CAPITAL UNIVERSITY OF SCIENCE AND
TECHNOLOGY, ISLAMABAD

Numerical Simulation of Mixed Convective Nanofluid Flows in a Square Cavity

by

Khalid Mehmood

A thesis submitted in partial fulfillment for the
degree of Doctor of Philosophy

in the

Faculty of Computing
Department of Mathematics

Numerical Simulation of Mixed Convective Nanofluid Flows in a Square Cavity

By

Khalid Mehmood
(PA133001)

Dr. Fatma Ibrahim
Technische Universität Dortmund
Fakultät für Mathematik Lehrstuhl
Dortmund, Germany
(Foreign Evaluator No. 1)

Dr. Hakan F. Öztop
Department of Mechanical Engineering,
Firat University, Elazig, Turkey
(Foreign Evaluator No. 2)

Dr. Muhammad Sagheer
(Thesis Supervisor)

Dr. Muhammad Sagheer
(Head, Department of Mathematics)

Dr. Muhammad Abdul Qadir
(Dean, Faculty of Computing)

Department of Mathematics
Capital University of Science & Technology
Islamabad

To my teachers and family

CAPITAL UNIVERSITY OF SCIENCE & TECHNOLOGY
ISLAMABAD
Expressway, Kahuta Road, Zone-V, Islamabad
Phone:+92-51-111-555-666 Fax: +92-51-4486705
Email: info@cust.edu.pk Website: https://www.cust.edu.pk

CERTIFICATE OF APPROVAL

This is to certify that the research work presented in the thesis, entitled "**Numerical Simulation of Mixed Convective Nanofluid Flows in a Square Cavity**" was conducted under the supervision of **Dr. Muhammad Sagheer**. No part of this thesis has been submitted anywhere else for any other degree. This thesis is submitted to the **Department of Mathematics, Capital University of Science and Technology** in partial fulfillment of the requirements for the degree of Doctor in Philosophy in the field of **Mathematics**. The open defence of the thesis was conducted on **01 February, 2018.**.

Student Name : Mr. Khalid Mehmood (PA133001)

The Examining Committee unanimously agrees to award PhD degree in the mentioned field.

Examination Committee :

(a) External Examiner 1: Dr. Muhammad Sabeel Khan
Assistant Professor
IST, Islamabad

(b) External Examiner 2: Dr. Muhammad Ayub
Professor
QAU, Islamabad

(c) Internal Examiner : Dr. Abdul Rehman Kashif
Associate Professor
Capital University of Science & Technology, Islamabad

Supervisor Name : Dr. Muhammad Sagheer
Professor
Capital University of Science & Technology, Islamabad

Name of HoD : Dr. Muhammad Sagheer
Professor
Capital University of Science & Technology, Islamabad

Name of Dean : Dr. Muhammad Abdul Qadir
Professor
Capital University of Science & Technology, Islamabad

AUTHOR'S DECLARATION

I, **Mr. Khalid Mehmaood (Registration No. PA133001)**, hereby state that my PhD thesis titled, '**Numerical Simulation of Mixed Convective Nanofluid Flows in a Square Cavity**' is my own work and has not been submitted previously by me for taking any degree from Capital University of Science and Technology, Islamabad or anywhere else in the country/ world.

At any time, if my statement is found to be incorrect even after my graduation, the University has the right to withdraw my PhD Degree.

(**Khalid Mehmood**)

Dated: 01 February, 2018

Registration No : PA133001

PLAGIARISM UNDERTAKING

I solemnly declare that research work presented in the thesis titled "**Numerical Simulation of Mixed Convective Nanofluid Flows in a Square Cavity**" is solely my research work with no significant contribution from any other person. Small contribution/ help wherever taken has been duly acknowledged and that complete thesis has been written by me.

I understand the zero tolerance policy of the HEC and Capital University of Science and Technology towards plagiarism. Therefore, I as an author of the above titled thesis declare that no portion of my thesis has been plagiarized and any material used as reference is properly referred/ cited.

I undertake that if I am found guilty of any formal plagiarism in the above titled thesis even after award of PhD Degree, the University reserves the right to withdraw/ revoke my PhD degree and that HEC and the University have the right to publish my name on the HEC/ University Website on which names of students are placed who submitted plagiarized thesis.

(**Khalid Mehmood**)
Registration No. PA133001

Dated: 01 February, 2018

Acknowledgements

First of all, I express my gratitude to Almighty Allah (SWT), the merciful, the compassionate and the creator of the whole universe, on the completion of my PhD studies. It was not possible for me without His blessings upon me. I offer my humblest words of thanks to the Holy Prophet Hazrat Muhammad (Peace be upon him) who is forever a torch of guidance for the humanity.

This is great opportunity for me to express my feelings of love and gratitude to my teacher and supervisor Prof. Dr. Muhammad Sagheer for he remained a constant source of inspiration to me. I am highly impressed by his nice behaviour, cooperation and kindness. I deeply appreciate for his guidance, encouragement, advice, ideas, and invaluable support, throughout the duration of this thesis.

A lot of appreciation is extended to Dr. Shafqat Hussain, Associate professor for his devotion, commitment, dedication and help during this project. He provided me the opportunity to learn the method that finally lead to this thesis. He patiently introduced me the basic knowledge of the topic and always helped me whenever I needed. His keen scientic insights were indispensable for this thesis and will always be a source of inspiration for my future career.

I am also grateful to the Vice Chancellor of the university and the Dean of the faculty of Computing for providing the best research facilities and conducive environment for study at CUST.

I gratefully acknowledge the funding source that made my Ph.D work possible. I was funded by the Higher Education Commission of Pakistan. I am deeply indebted to my parents, my wife and other family members. Without their love, prayers, time and guidance, it would not be possible for me to complete this task.

Last but not the least, my sincere thanks goes to my friends Mr. Muhammad Bilal, Mr. Yasir Mehmood, Mr. Tanvir Sajid and Mr. Sajid Shah for very good company and entertainment activities in free hours at the university.

List of Publications

1. S. Hussain, K. Mehmood, M. Sagheer, MHD mixed convection and entropy generation of water-alumina nanofluid flow in a double lid driven cavity with discrete heating, Journal of Magnetism and Magnetic Materials, pp. 140-155, vol. 419, 2016.

2. S. Hussain, S. Ahmed, K. Mehmood, M. Sagheer, Effects of inclination angle on mixed convective nanofluid flow in a double lid-driven cavity with discrete heat sources, International Journal of Heat and Mass Transfer, pp. 847-860, vol. 106, 2017.

3. K. Mehmood, S. Hussain, M. Sagheer, Mixed convection in alumina-water nanofluid filled lid–driven square cavity with an isothermally heated square blockage inside with magnetic field effect: Introduction, International Journal of Heat and Mass Transfer, pp. 397-409, vol. 109, 2017.

4. K. Mehmood, S. Hussain, M. Sagheer, MHD mixed convection in alumina-water nanofluid filled square porous cavity using KKL model: Effects of non-linear thermal radiation and inclined magnetic field, Journal of Molecular Liquids, pp. 485-498, vol. 238, 2017.

Abstract

The aim of this thesis is to investigate the mixed convective nanofluid flow in the square cavities with different physical effects. Initially, the influence of the cavity inclination angle on the mixed convective nanofluid flow in a double lid-driven cavity shall be considered. Then the magnetohydrodynamics mixed convective nanofluid flow and entropy generation in a double lid-driven square cavity with discrete heating will be examined. Furthermore, the mixed convection in nanofluid filled lid-driven square cavity with an isothermally heated square blockage inside with magnetic field effect will also be analysed. At the end, the mixed convective nanofluid flow in a lid-driven square porous cavity using the Ko-Kleinstreuer-Li model considering the effect of thermal radiation and inclined magnetic field will be discussed. In all the discussed problems, the governing nonlinear partial differential equations are solved by the Galerkin finite element method in space and the fully implicit Crank-Nicolson scheme in time. The discretized systems of nonlinear equations are linearized by means of Newton's method and the associated linear subproblems are solved with the help of Gaussian elimination method. The effect of physical parameters on the fluid flow has been investigated and discussed in detail by means of streamlines, isotherms and plots. The optimization of the thermodynamic efficiency of a system is today's requirement. The entropy generation reduces this efficiency, therefore, it becomes necessary to reduce the entropy generation. To do this, one has to carefully measure the entropy generation in a process. Due to this motivation, calculation of entropy generation due to heat transfer, fluid friction and magnetic field has also been taken into account in some part of the study along with other physical effects.

Contents

List of Figures

List of Tables

Abbreviations

CFD	Computational fluid dynamics
DOFs	Degrees of freedom
FEM	Finite element method
FEATFLOW	Finite element analysis tool for the flow problems
KKL	Ko-Kleinstreuer-Li
LBB	Ladyzhenskaya-Babuŝka-Brezzi
MHD	Magnetohydrodynamics
NEN	Number of elemental nodes

Symbols

Be	Bejan number
C_p	specific heat (J $kg^{-1}K^{-1}$)
d_p	diameter of nanoparticle (nm)
Da	Darcy number, K/L^2
e_{S1}	dimensional length of left heat source (m)
e_{S2}	dimensional length of right heat source (m)
g	gravitational acceleration (m s^{-2})
Gr	Grashof number, $\frac{\beta g \Delta T L^3}{\nu_f^2}$
k	thermal conductivity (W m^{-1} K^{-1})
k_m	effective thermal conductivity of porous medium (W m^{-1} K^{-1})
K	permeability of porous media (m^2)
L	length of cavity (m)
Nu	local Nusselt number
Nu_{avg}	average Nusselt number
$Nu_{\text{avg},S1}$	average Nusselt number due to left heat source
$Nu_{\text{avg},S2}$	average Nusselt number due to right heat source
p	pressure (N m^{-2})
P	dimensionless pressure
Pr	Prandtl number, ν_f/α_f
Re	Reynolds number, V_w L/ν_f
Ri	Richardson number, Gr/Re^2
S_T	dimensionless total entropy
$S1$	left heat source

$S2$	right heat source
s	dimensional entropy (J/K)
t	dimensional time (s)
T	dimensional temperature (K)
u, v	x-velocity and y-velocity (m s^{-1})
U, V	dimensionless x-velocity and y-velocity
U_0	horizontal lid velocity
V_w	vertical lid velocity
x, y	dimensional space coordinates (m)
X, Y	dimensionless space coordinates

Greek symbols

α	thermal diffusivity (m^2 s^{-1})
β	thermal expansion coefficient (K^{-1})
γ	inclination angle of magnetic field
ϵ	porosity of the porous medium
θ	dimensionless temperature
μ	dynamic viscosity (kg m^{-1} s^{-1})
ν	kinematic viscosity (m^2 s^{-1})
ρ	density (kg m^{-3})
σ	electrical conductivity (Ω m)$^{-1}$
τ	dimensionless time
ϕ	volume fraction of the nanoparticles
ψ	inclination angle of cavity

Subscripts

c	cold
f	base fluid
h	hot
nf	nanofluid
p	nanoparticles

Chapter 1

Introduction

1.1 Introduction

In fluid dynamics, heat transfer over mixed convective flow in lid-driven cavities is one of the most extensively studied problem by researchers and industrialists due to its growing practical applications. A lot of problems arising in industry can be simulated using cavity due to its simple geometry. In order to enhance the heat conductivity of base fluids like water, ethylene glycol, oil, etc., modern techniques have been adopted. First of all, Choi [1] contributed in this field by introducing the nanofluids. Later on, many researchers have utilized nanoparticles to study heat transfer mechanism [2–17]. In the last two decades, numerous scientists have participated a lot to solve the heat transfer problems in cavities filled with nanofluids experimentally, analytically as well as numerically.

1.1.1 Mixed Convection in Cavities

Mixed convection in cavities has been studied by many researchers due to its numerous applications including electronic instruments cooling, heat exchangers, chemical reactors, solar collectors, heating and cooling of buildings. Sourtiji *et al.* [18] investigated heat treansfer in mixed convective Al_2O_3-water nanofluid flow in

a ventilated cavity. It is observed that heat transfer increases with an increase in the values of Reynolds number, Richardson number and nanoparticle volume fraction. Teamah *et al.* [19] have investigated laminar mixed convection in shallow inclined cavities using numerical simulation. They showed the influence of cavity inclination on the flow, thermal and mass fields for inclination angles ranging from 0° to 30°. Ahmed *et al.* [20] examined the mixed convection from a discrete heat source in enclosures with two adjacent moving walls and filled with micropolar nanofluid. It was noticed that average Nusselt number along the heat source decreases as the heat source length increases while it increases when the solid volume fraction increases. Sheremet and Pop [21] analyzed the mixed convection in a lid-driven square cavity filled by a nanofluid using Buongiorno's mathematical model. They found that Richardson number and the moving parameter play a dominant role in the transfer of heat and mass and other flow characteristics within a cavity. Sheikholeslami *et al.* [22] conducted numerical study on MHD free convective alumina-water nanofluid flow taking into account thermal radiation and observed the enhancement in the average Nusselt number with Rayleigh number, nanoparticles volume fraction and radiation parameter while it declined with a growth in Hartmann number and viscous dissipation parameter. In another study, Sheikholeslami [23] utilized Ko-Kleinstreuer-Li formulation simulating the nanofluid flow in a porous channel. KKL correlation was applied to calculate the effective thermal conductivity and viscosity of nanofluid. Sheikholeslami and Rashidi [24] considered the influence of space dependent magnetic field on free convection of Fe_3O_4-water nanofluid. Mixed convective flow in an inclined square enclosure saturated with a nanofluid was discussed by Abu-Nada and Chamkha [25] with the conclusion that the Richardson number plays a vital role in heat transfer process and flow properties inside an enclosure. Also, it was anticipated that substantial heat transfer could be enhanced due to existence of nanoparticles and this would be attained by inclination of cavity at different values of Ri. Mixed convection in an inclined two sided lid-driven cavity filled with nanofluid utilizing two-phase mixture model was propounded by Alinia *et al.* [26]. It was observed that augmentation of SiO_2 nanoparticles enhances more heat

transfer as compared with pure fluid and inclination angle affects a lot on the flow characteristics at high Richardson number. Sivasankaran *et al.* [27] considered a lid-driven inclined cavity with discrete heating and found that more transfer of heat was observed at cavity inclination angle of $\gamma = 30°$. Mixed convection of Cu-water nanofluid in an inclined lid-driven cavity utilizing the lattice Boltzmann method was investigated by Karimipour *et al.* [28] and it was found that movement of cavity lid at $Ri = 0.1$ has more effects on nanofluid than that of $Ri = 1$. Also, introducing 4% of Cu-nanoparticles in the base fluid increases 50% of average Nusselt number for inclination angles of cavity ranging from 0° to 90° at $Ri = 0.1$ and $Re = 100$. Larger concentration of nanoparticles increases the average Nusselt number faintly at $Ri = 1$ for inclination angle equal to 0° but it enhances rapidly average Nusselt number for inclination angle $\gamma = 90°$. Das and Tiwari [29] numerically examined the problem of mixed convection of differentially heated enclosure saturated with Cu-water nanofluid and their conclusion showed that the average Nusselt number increases significantly with the augmentation of nanoparticles volume fraction keeping Richardson number at unity. Subdani *et al.* [30] numerically investigated the flow and heat transfer in a square cavity filled with alumina-water nanofluid, with a heat source at the bottom wall. In their study, enhancement in heat transfer was observed with increasing Reynolds number for constant Rayleigh number and heat source placed at the centre of the bottom wall. A lid driven enclosure saturated with nanofluid was investigated numerically for the mixed convection by Muthtamilselvan *et al.* [31] and found that fluid flow and heat transfer were affected both by the aspect ratio of the cavity and nanoparticles volume fraction. A similar study was performed numerically for natural convection by Ho *et al.* [32] in a two-dimensional cavity. Their study revealed that heat transfer in a cavity was enhanced due to augmentation in the concentration of copper-water nanoparticles at some fixed Grashof number. Natural convective heat transfer in a cavity saturated with alumina-water nanofluid using numerical simulation was performed by Khanafer *et al.* [33]. It was seen that the heat transfer increases or decreases due to the model that was used for

viscosity and thermal conductivity of the nanofluid. Mahmoudi *et al.* [34] numerically studied the mixed convection flow in a vented square cavity filled with copper-water nanofluid. The special criteria they adopted was the consideration of inlet and outlet ports to configure at four different places. They observed their influence on the flow and heat transfer and it was noticed that Reynolds number, Richardson number and nanoparticles volume fraction have significant effect on the numerical characteristic of the flow field. Furthermore, they noticed that the the flow fields and the temperature distribution inside the cavity were dependent on the location of the inlet and outlet.

1.1.2 Magnetohydrodynamics

The effect of magnetic field on convective heat transfer in a cavity was extensively investigated by many researchers [35–43]. Shirvan *et al.* [44] investigated the effect of magnetic field on mixed convective heat transfer in a ventilated square cavity. It is worthy noted that the heat transfer rate decreases with an increase in the Hartmann number. Malvandi and Ganji [45] discussed free convection in a cavity saturated with alumina-water nanofluid with magnetic field effect. Observation indicates that magnetic field increases the slip velocity and the velocity gradient near the wall but reduces the heat transfer rate. Mixed convection of shear-thinning fluids in a cavity with MHD was investigated by Kefayati [46]. For an electrically conducting fluid, the influence of Lorentz force is to inhibit convection flow by reducing the fluid velocity so that the existence of external magnetic field becomes an active technique in manufacturing industries. Orientation and strength of magnetic field play a vital role in the behavior of flow. Applied magnetic field influences the suspended particles and reshuffles their concentration in the fluid which effectively changes the heat transfer characteristics of the flow. Mixed convection in a porous cavity with MHD effect using numerical approach was examined by Mohan and Satheesh [47]. Analysis shows that MHD effect plays an important role in the dynamics of temperature and concentration which depend on the aspect ratio and Hartmann number. Elshehabey and Ahmed [48] have investigated MHD

effect on mixed convection in a cavity saturated with a nanofluid. It was shown that inclined magnetic field cease the fluid flow. Selimefendigil and Chamkha [49] analyzed the MHD mixed convective, non-Newtonian power law fluid in a cavity with an uneven bottom wall considering the impact of an inclined magnetic field and found that the natural convection plays a vital role for a shear-thinning fluid. Sheremet *et al.* [50] considered a wavy-walled cavity saturated with a nanofluid under the influence of magnetic field. It has been perceived that the average Nusselt number at vertical hot wavy wall is an increasing function of the magnetic field inclination angle γ for $0 < \gamma < \pi/2$ and decreasing for $\pi/2 < \gamma < \pi$.

1.1.3 Isothermal Blockage Inside a Cavity

Heat transfer in a cavity with one or more obstacles inside has drawn the attention of many researchers in the last decade. Esfe *et al.* [51] discussed the mixed convective nanofluid flow in an enclosure with a hot obstacle inside. Their conclusion showed that the nanofluid descends downward along the right wall, moves horizontally above the obstacle to the left corner of the cavity along the bottom wall and then moves upward and forms an eddy inside the cavity. Increasing the Richardson number, clockwise rotating vortex becomes larger due to the effect of the obstacle. Islam *et al.* [52] examined the mixed convection in a lid driven cavity with an isothermal block inside and found that for any size of blockage kept at random place in a cavity, the average Nusselt number changes only when the Richardson number exceeds the order of 1. For Richardson number more than 1, average Nusselt number increases speedily. Moreover, optimal situation for heat transfer was acquired to maintain the block at the top left and bottom right corner of the cavity. Öztop *et al.* [53] considered the fluid flow due to combined convection in lid driven enclosure having a circular body. It was indicated that the circular body played a role of control parameter for the heat and fluid flow. Billah *et al.* [54] investigated the mixed convection in a lid-driven cavity with a heated circular hollow cylinder and found that the heat transfer and fluid flow are strongly dependent on the diameter of the hollow cylinder. Considerable influence of cylinder on the

flow for the cases of forced, mixed and natural convection was observed. For the fixed Richardson number, cylinder augmented the heat transfer with increasing diameter. Mehrizi *et al.* [55] analyzed the mixed convection in a ventilated cavity with hot obstacle considering the influence of nanofluid and outlet port location. They have shown that the heat transfer enhanced with increasing the nanoparticles volume fraction for various Richardson numbers and outlet port positions. Moreover, an augmentation in the Richardson number caused to change the main flow direction from top to bottom of the obstacle. Rahman *et al.* [56] examined the magnetohydrodynamic mixed convection and Joule heating in a lid driven cavity having a square block inside and observed that the flow field and temperature profile mainly depend on the magnetic parameter, Joule heating parameter and size of the inner block for the mixed convection regime. Khanafer and Aithal [57] discussed the mixed convection flow and heat transfer in a lid driven cavity with a circular cylinder. It was observed that the optimal heat transfer results could be obtained while placing the cylinder near the bottom wall for different Richardson numbers. For natural and mixed convection, the average Nusselt number increases with an increase in the radius of the cylinder for various Richardson numbers. Selimefendigil and Öztop [58] considered the MHD mixed convection in a nanofluid filled lid driven square enclosure with a rotating cylinder inside and their conclusion showed that the heat transfer enhancement for $Ri = 10$ was 17% more than that for $Ri = 1$. A numerical study on the mixed convection in a lid driven cavity with a circular cylinder has been conducted by Zheng *et al.* [59]. They showed that the fluid flow and heat transfer characteristics in the cavity strongly depend on the position of the circular cylinder as well as on the relative magnitude of the forced convection and the natural convection caused by the movement in the top wall of the cavity and the heating at the hot bottom wall, respectively.

1.1.4 Porosity

Mixed convective heat transfer in porous media has attracted a lot of researchers due to its demanding applications in science and engineering including civil, chemical and mechanical engineering. Heat exchangers [60], boilers [61], oil and gas flowing in reservoirs [62], water filtration [63], ground-water flows [64], transfer of drugs in tissues [65], fuel cells [66], packed-bed energy storage systems [67], thermal insulation [68, 69] and fluidized beds [70] are some examples out of many applications. One can found comprehensive discussion on the the heat and mass transfer in porous media in the books [71–73]. Sheremet and Pop [74] investigated natural convective nanofluid flow in a porous cavity and unveiled that the average Nusselt number and Sherwood number amplify with an increase in the buoyancy ratio parameter. Chamkha and Ismael [75] examined the natural convection in the porous enclosure saturated with nanofluid and found that the Nusselt number increases as thickness of porous layer reaches a certain critical value and after that it is reduced. Ahmed *et al.* [76] considered the MHD and viscous dissipation effects on the mixed convective flow in a porous cavity and observed that the average Nusselt number increases with an augmentation in the viscous dissipation and Darcy number. Rashad *et al.* [77] discussed the free convective nanofluid flow in a porous cavity considering the effect of magnetic field and internal heat generation. More study on nanofluid saturated porous cavity can be consulted in the literature [78–88].

1.1.5 Entropy Generation

Entropy is defined as the degree of disorder in a closed but varying system, a system in which transfer of energy takes place in one direction only. Entropy generation that signifies the amount of irreversibility in a process is the criteria for the performance of the engineering machinery. Thermodynamic efficiency of a system is reduced due to entropy generation. Entropy analysis tells us the part of the physical model or system in which energy is dissipated to a greater extent.

Basics to minimize the entropy generation was examined by Bejan [89]. Prototypical structure of heat transfer procedure in various industries is acquired with an accurate measurement of entropy generation since it clarifies waste of energy in a process. Hence, entropy generation is examined in the mixed convection of pure and nanofluid [90–100]. Hajialigal *et al.* [101] discussed the influence of magnetic field on the mixed convection and entropy generation in nanofluid saturated with three dimensional microchannels. It is highlighted that the entropy generation reduces with a growth in the magnetic field strength and the solid volume fraction. Mehrez *et al.* [102] investigated the impact of MHD on the transfer of heat and entropy generation in a cavity filled with nanofluid. It was found that an augmentation in the nanoparticles volume fraction results an enhancement in the average Nusselt number and entropy generation. It depends mostly on the strength and inclination angle of the magnetic field. Kefayati [103] has considered simulation of the power-law fluids with Soret and Dufour effects in an inclined porous cavity. Observations show that the entropy generation declines with an enhancement in the inclination angle from 40° to 80°. Mixed convection and entropy generation in a trapezoidal enclosure filled with nanofluid considering the influence of magnetic field were conducted by Aghaei *et al.* [104]. It was shown that the influence of fluid friction on entropy generation is negligible. Entropy is mostly generated due to the heat transfer. Selimefendigil and Öztop [105] investigated the impact of heat generation and magnetic field in a cavity saturated with nanofluid. It was noticed that the heat transfer reduces due to the existence of different obstacles. Entropy analysis of the MHD pseudo-plastic nanofluid flow through a vertical porous channel with convective heating was discussed by Das *et al.* [106]. It was found that the temperature of the fluid enhances with increasing Eckert number, thermal conductivity parameter and Biot number. Also, an increase in the power-law index caused the entropy generation rate to decline. Main source of entropy and heat transfer irreversibility was the channel wall.

1.2 Thesis Contributions

In this thesis, numerical simulation of mixed convective alumina-water nanofluid flow in a double lid driven square cavity has been executed. The Galerkin weighted residual finite element method has been utilized for spatial discretisation and the Crank-Nicolson implicit scheme is applied for temporal discretisation. Initially, we consider the influence of cavity inclination angle on the mixed convective nanofluid flow in a double lid-driven cavity. Then the magnetohydrodynamics mixed convective nanofluid flow and entropy generation in a double lid-driven square cavity with discrete heating was examined. Furthermore, the mixed convection in a nanofluid filled lid-driven square cavity with an isothermally heated square blockage inside with magnetic field effect has been analyzed. At the end, the mixed convective nanofluid flow in a lid-driven square porous cavity using Ko-Kleinstreuer-Li model considering the effect of thermal radiation and inclined magnetic field was discussed. Furthermore, the behaviour of the average Nusselt number, the entropy generation due to heat transfer, fluid friction, magnetic field, the total entropy generation, average temperature, kinetic energy and Bejan number have been investigated under the influence of different physical parameters like Reynolds number, Richardson number, Hartmann number, Eckert number, Darcy number, nanoparticles volume fraction, cavity inclination angle, magnetic field inclination angle, porosity and thermal radiation parameter and discussed physically in detail by means of streamlines, isotherms and plots.

All the computations during the preparation of this thesis are performed by using the finite element solver package FEATFLOW. The FEATFLOW is a general purpose open source FEM software package particularly for the simulations of the CFD problems. A brief introduction can be found at http://www.featflow.de.

1.3 Thesis Outline

This thesis is further subdivided in the following way.

The basic governing equations, discretization techniques and solution methodology have been discussed in **Chapter 2**.

The effect of the inclination angle on the mixed convective nanofluid flow in a double lid-driven cavity has been discussed in **Chapter 3**. The contents of this chapter are published.

MHD mixed convective alumina-water nanofluid flow and entropy generation in a lid driven square cavity is presented in **Chapter 4**. The contents of this chapter are published.

Mixed convective alumina-water nanofluid flow in a lid-driven square cavity with an isothermally heated square blockage inside under the influence of magnetic field effect has been considered in **Chapter 5**. The contents of this chapter are published.

MHD mixed convection in alumina–water nanofluid filled square porous cavity using KKL model considering the effects of non-linear thermal radiation and inclined magnetic field has been elaborated in **Chapter 6**. The contents of this chapter are published.

The whole analysis has been concluded in **Chapter 7**.

Chapter 2

Governing Equations and Discretization Techniques

In this chapter, we briefly discuss the basic laws governing the mathematical models discussed in this thesis. Since the entropy generation will be calculated in the forthcoming study, therefore the entropy generation and its principles have also been listed. The finite element method has been explained by taking an example of an unsteady heat equation along with semi-discretizations in space and time. Furthermore, the mixed finite element method has also been discussed.

2.1 Fundamental Laws

2.1.1 Law of Conservation of Mass

"The continuity equation or the law of conservation of mass [107] is written as

$$\frac{\partial \rho}{\partial t} + \nabla.(\rho \mathbf{V}) = 0, \tag{2.1}$$

where ρ is density and $\mathbf{V}$ is the velocity of fluid. For incompressible fluids, the above equation can be expressed in the following way

$$\nabla.\mathbf{V} = 0. \tag{2.2}$$

2.1.2 Law of Conservation of Momentum

The mathematical expression for law of momentum is

$$\rho\frac{D\mathbf{V}}{Dt} = \nabla.\tau + \rho\mathbf{b}. \tag{2.3}$$

The Cauchy stress tensor for an incompressible flow is $-p\mathbf{I} + \mathbf{S}$ in which p is the pressure, $\mathbf{I}$ is the identity tensor, $\mathbf{S}$ is the extra stress tensor, $\mathbf{b}$ is the body force and $\frac{D}{Dt}$ is the material time derivative. The Cauchy stress tensor and the velocity field are

$$\tau = \begin{bmatrix} \sigma_{xx} & \tau_{xy} & \tau_{xz} \\ \tau_{yx} & \sigma_{yy} & \tau_{yz} \\ \tau_{zx} & \tau_{zy} & \sigma_{zz} \end{bmatrix}, \tag{2.4}$$

$$\mathbf{V} = [u(x,y,z), v(x,y,z), w(x,y,z)], \tag{2.5}$$

where σ_{xx}, σ_{yy} and σ_{zz} are the normal stresses, τ_{xy}, τ_{xz}, τ_{yx}, τ_{yz}, τ_{zx} and τ_{zy} are shear stresses and u, v, w are the velocity components along the x, y and z-directions respectively. Eq. (2.3) in scalar form yields

$$\rho\left(\frac{\partial u}{\partial t} + u\frac{\partial u}{\partial x} + v\frac{\partial u}{\partial y} + w\frac{\partial u}{\partial z}\right) = \frac{\partial(\sigma_{xx})}{\partial x} + \frac{\partial(\tau_{xy})}{\partial y} + \frac{\partial(\tau_{xz})}{\partial z} + \rho b_x, \tag{2.6}$$

$$\rho\left(\frac{\partial v}{\partial t} + u\frac{\partial v}{\partial x} + v\frac{\partial v}{\partial y} + w\frac{\partial v}{\partial z}\right) = \frac{\partial(\tau_{yx})}{\partial x} + \frac{\partial(\sigma_{yy})}{\partial y} + \frac{\partial(\tau_{yz})}{\partial z} + \rho b_y, \tag{2.7}$$

$$\rho\left(\frac{\partial w}{\partial t} + u\frac{\partial w}{\partial x} + v\frac{\partial w}{\partial y} + w\frac{\partial w}{\partial z}\right) = \frac{\partial(\tau_{zx})}{\partial x} + \frac{\partial(\tau_{zy})}{\partial y} + \frac{\partial(\sigma_{zz})}{\partial z} + \rho b_z, \tag{2.8}$$

where b_x, b_y and b_z show the components of body force along the x, y and z-axes, respectively. The above equations for two-dimensional flow become

$$\rho\left(\frac{\partial u}{\partial t}+u\frac{\partial u}{\partial x}+v\frac{\partial u}{\partial y}\right)=\frac{\partial(\sigma_{xx})}{\partial x}+\frac{\partial(\tau_{xy})}{\partial y}+\rho b_x, \tag{2.9}$$

$$\rho\left(\frac{\partial v}{\partial t}+u\frac{\partial v}{\partial x}+v\frac{\partial v}{\partial y}\right)=\frac{\partial(\tau_{yx})}{\partial x}+\frac{\partial(\sigma_{yy})}{\partial y}+\rho b_y, \tag{2.10}$$

2.1.3 Equation of Heat Transfer

According to first law of thermodynamics, the heat transfer equation is

$$\rho\frac{d\varepsilon}{dt}=\tau.\mathbf{L}-\nabla.\mathbf{q}+\rho r_h, \tag{2.11}$$

where $\varepsilon = C_pT$ is the internal energy, C_p is the specific heat, T is the temperature, $\mathbf{L} = \nabla\mathbf{V}$ is the velocity gradient, $\mathbf{q} = -k\nabla T$ is the heat flux, k is the thermal conductivity and r_h is the radiative heating. The above equation in the absence of radiative heating is

$$\rho C_p\frac{dT}{dt}=\tau.\nabla\mathbf{V}+k\nabla^2T.\text{"} \tag{2.12}$$

2.2 Magnetohydrodynamics

The magnetohydrodynamics is the study of the magnetic properties of an electrically conducting fluid. The field of MHD was introduced by the Swedish plasma physicist and the Nobel Laureate Hannes Alfvén. The basic perception of MHD is that an electromagnetic force exerts an influence not only on the flow of conducting fluid but it also changes itself under the influence of the flow. In general, the system of equations illustrating the movement of the conducting fluid in the presence of an external magnetic field, is composed of the Navier-Stokes and the

Maxwell equations [108]. The Navier-Stokes equation of motion including electromagnetic body force (Lorentz force) $\mathbf{F} = \mathbf{j} \times \mathbf{B}$ is

$$\frac{\partial \mathbf{V}}{\partial t} + (\mathbf{V}.\nabla)\,\mathbf{V} = -\frac{1}{\rho}\nabla P + \nu\nabla^2\mathbf{V} + \frac{1}{\rho}\,(\mathbf{j} \times \mathbf{B})\,. \tag{2.13}$$

The continuity equation for incompressible fluids is

$$\nabla.\mathbf{V} = 0. \tag{2.14}$$

The Ohm's law for slowly moving medium (medium velocity should be much smaller than the velocity of light) in a magnetic field is

$$\mathbf{j} = \sigma(\mathbf{E} + \mathbf{V} \times \mathbf{B}). \tag{2.15}$$

The Maxwell equations are

$$\frac{\partial \mathbf{B}}{\partial t} = -(\nabla \times \mathbf{E}), \tag{2.16}$$

$$\mathbf{j} = \frac{1}{\mu}(\nabla \times \mathbf{B}) - \epsilon\frac{\partial \mathbf{E}}{\partial \mathbf{t}}, \tag{2.17}$$

$$\nabla.\mathbf{B} = 0, \tag{2.18}$$

$$\nabla.\mathbf{E} = \frac{\rho}{\epsilon}. \tag{2.19}$$

Here $\mathbf{V}$ is the fluid velocity, σ is the electrical conductivity, $\mathbf{E}$ is an electric field, P is the pressure, ν is the kinematic viscosity, $\mathbf{B}$ is the magnetic induction, ρ is the density, $\mathbf{j}$ is an electric current. The Eq. (2.13) illustrates the movement of a conducting fluid in the magnetic field and includes the force of pressure gradient ∇P, viscosity $\nu\nabla^2\mathbf{V}$, inertial force $(\mathbf{V}.\nabla)\,\mathbf{V}$ and Lorentz force $\mathbf{j} \times \mathbf{B}$ on the element of moving medium. The existence of a Lorentz force in the conducting fluid due to the interaction of the current $\mathbf{j}$ with the magnetic field $\mathbf{B}$, shows the major difference between the hydrodynamics and the magnetohydrodynamics.

2.3 Principle of Entropy Generation

The concepts of entropy and irreversibility, derived from the second law of thermodynamics, were introduced by the German physicist Rudolf Clausius in 1856. According to the second law of thermodynamics, the entropy of a closed system always increases with the time. It is constant in the case when a process is reversible or in equilibrium. The enhancement in the entropy elucidates the irreversibility of the natural processes.

Entropy is the thermodynamic characteristics just like pressure and temperature. The changes in a closed system subject to entropy are expressed by the ratio Q/T, where Q is net heat transfer and T is temperature. Entropy increases as T decreases or Q increases. In a reversible process, a small increase in the entropy (dS) of a system is defined as a ratio of the small transfer of heat (δQ) to a closed system divided by the common temperature (T) of the system and the surroundings which supply the heat, i.e.,

$$dS = \frac{\delta Q}{T}. \tag{2.20}$$

Eq. (2.20) is valid for an ideal, closed and reversible process. For an actually possible small process in an isolated system, the second law requires that the above equation changes to an inequality given by

$$dS > \frac{\delta Q}{T}. \tag{2.21}$$

2.4 The Finite Element Method

The finite element method is utilized for the spatial discretization of the problems considered in this thesis. Initially, this method was used to solve the elasticity and structural mechanics problems but these days it has become very beneficial for the solution of partial differential equations arising in the fluid mechanics, solid mechanics and engineering. In this mathematical technique, the original strong form of the partial differential equations is transformed to variational or weak form

by multiplying with a weight (or test) function and integrating over the domain. We will apply Galerkin weighted residual finite element method in the subsequent work.

2.4.1 Weighted Residual Formulation

We explain the weighted residual finite element method with the help of a two dimensional, steady, linear problem

$$Lu = f \quad \text{in } \Omega, \tag{2.22}$$

$$u = 0 \quad \text{on } \partial\Omega, \tag{2.23}$$

with $\Omega \subset \mathbb{R}^2$ and L is the Laplacian operator. The function u is defined as $u : \Omega \to \mathbb{R}$ and if the solution u is an exact, then the residual $R(u) = Lu - f = 0$, otherwise $R(\tilde{u}) \neq 0$ for an approximate solution $\tilde{u} \approx u$. Our target is to search for a function u_h that forces residual equal to zero by a suitable function [109]. The Eq. (2.22) is in strong form. In finite element method we suppose the integral form also known as the weak or variational form of Eq. (2.22). First, the equation is multiplied by an appropriate test function w and then integrated over the domain Ω to obtain

$$\int_\Omega (Lu - f)w \; d\Omega = 0, \quad \text{for all} \quad w \in W, \tag{2.24}$$

where W is the test space. Applying the Green's theorem to Eq. (2.24) and incorporating the boundary condition, we have

$$a(u, \; w) = \int_\Omega f \; w \; d\Omega, \quad \text{for all} \quad w \in W, \tag{2.25}$$

where

$$a(u, w) = \int_\Omega \left(\frac{\partial u}{\partial x}\frac{\partial w}{\partial x} + \frac{\partial u}{\partial y}\frac{\partial w}{\partial y} \right) \; d\Omega, \quad \text{for all} \quad w \in W, \tag{2.26}$$

is the bilinear form. We say that $a(.,.)$ is a bilinear form on $V \times V$ if $a : V \times V \to \mathbb{R}$, i.e., $a(u, w) \in \mathbb{R}$ for $u, \; w \in \; V$. Let us assume that the function u be approximated

by the trial function $u_h \in U_h$ of the form

$$u_h \approx \sum_{j=1}^{N} c_j \phi_j \in U_h, \tag{2.27}$$

where U_h, c_j, ϕ_j are the finite dimensional trial space, unknown coefficients (to be determined) and basis functions, respectively. We must also replace the infinite dimensional test space W by a finite dimensional test space $W_h \in W$. Moreover, the computational domain is subdivided into a number of non-overlapping elements. Finite dimensional test space can be expressed as

$$w_h \approx \sum_{i=1}^{N} d_i \psi_i \in W_h, \tag{2.28}$$

where ψ_i are basis functions from the test space. Incorporating the approximate solutions in Eqs. (2.25) and (2.26), these can be rewritten as

$$a(u_h, w_h) = \int_\Omega \left(\frac{\partial u_h}{\partial x}\frac{\partial w_h}{\partial x} + \frac{\partial u_h}{\partial y}\frac{\partial w_h}{\partial y} \right) \, d\Omega = \int_\Omega f w_h \, d\Omega. \tag{2.29}$$

Our target is to compute c_j where basis functions are predefined. The expression (2.29) holds for all possible choices of d_i, $i = 1, 2, ..., N$. Thus the unknown coefficients c_j for the approximate solution u_h can be determined by solving the following system of equations

$$\sum_{j=1}^{N} c_j a(\phi_j, \psi_i) = \int_\Omega f \psi_i \, d\Omega, \quad \forall \; i = 1, 2, ..., N. \tag{2.30}$$

There exist several methods of weighted residuals that depend on the choice of ψ_i for example the collocation method and the least square method. If one selects $\psi_i = \phi_i$, this method is known as standard Galerkin method and the same method is utilized in this work.

2.4.2 The Unsteady Heat Equation

We consider an unsteady two dimensional heat equation, i.e.,

$$\frac{\partial u}{\partial t} - \left(\frac{\partial^2 u}{\partial x^2} + \frac{\partial^2 u}{\partial y^2}\right) = f \quad \text{in} \quad \Omega. \tag{2.31}$$

The scaler unknown u is a function of both space and time variables and $u : \Omega \to \mathbb{R}$ with $\Omega \subset \mathbb{R}^2$. The time domain is taken as $[0, T]$ that is further divided into N subintervals $[t_{k-1}, t_k], k = 1, 2, ..., N$ such that $0 = t_0, t_{k-1} < t_k$ and $t_N = T$. The time step is represented by $\Delta t = t_k - t_{k-1},\ k = 1, 2, ..., N$. To obtain a solution at an initial time step on the full domain, an initial condition and two boundary conditions are required. After multiplying Eq. (2.31) by the test (weight) function w and integrating by parts, we get

$$\int_{\Omega_e} \left(\frac{\partial u}{\partial t} w + \frac{\partial u}{\partial x}\frac{\partial w}{\partial x} + \frac{\partial u}{\partial y}\frac{\partial w}{\partial y}\right) d\Omega = \int_{\Omega_e} f w d\Omega + \text{B.T.} \tag{2.32}$$

Here, B.T. represents the boundary integral term. The Eq. (2.32) is the variational or weak form of the problem (2.31). For solution, we apply the method of lines in which semi-discretiation of space is performed first to obtain a system of ordinary differential equations, then the semi-discretiation in time is employed to get an algebraic system of equations.

2.4.3 The Semi-discretization in Space

The approximate solution over an element can be given by

$$u^e(x, y, t) = \sum_{j=1}^{NEN} u_j(t)\xi_j(x, y) \tag{2.33}$$

Substituting the approximate solution into the weak form, we get

$$\int_{\Omega^e} \left[\left(\sum_{j=1}^{NEN} \frac{\partial u_j}{\partial t} \xi_j \right) w + \left(\sum_{j=1}^{NEN} u_j \frac{\partial \xi_j}{\partial x} \right) \frac{\partial w}{\partial x} + \left(\sum_{j=1}^{NEN} u_j \frac{\partial \xi_j}{\partial y} \right) \frac{\partial w}{\partial y} \right] d\Omega = \int_{\Omega^e} f w d\Omega + \text{B.T.} \quad (2.34)$$

Utilizing the Galerkin finite element method, we choose a weight function $w = \xi_i(x, y)$ to get the following i^{th} equation of the elemental system

$$\int_{\Omega^e} \left[\left(\sum_{j=1}^{NEN} \frac{\partial u_j}{\partial t} \xi_j(x, y) \right) \xi_i + \left(\sum_{j=1}^{NEN} u_j \frac{\partial \xi_j}{\partial x} \right) \frac{\partial \xi_i}{\partial x} + \left(\sum_{j=1}^{NEN} u_j \frac{\partial \xi_j}{\partial y} \right) \frac{\partial \xi_i}{\partial y} \right] d\Omega = \int_{\Omega^e} f \xi_i d\Omega + \text{B.T.} \quad (2.35)$$

Taking the summation sign outside of the integral

$$\sum_{j=1}^{NEN} \left[\int_{\Omega^e} \xi_j \xi_i d\Omega \right] \frac{\partial u_j}{\partial t} + \sum_{j=1}^{NEN} \left[\int_{\Omega^e} \left(\frac{\partial \xi_j}{\partial x} \frac{\partial \xi_i}{\partial x} \right) + \int_{\Omega^e} \left(\frac{\partial \xi_j}{\partial y} \frac{\partial \xi_i}{\partial y} \right) d\Omega \right] u_j = \int_{\Omega^e} f \xi_i d\Omega + \text{B.T.} \quad (2.36)$$

The final equation can be expressed in the following compact form

$$[M^e]\{\dot{u}^e\} + [K^e][u^e] = \{F^e\}, \quad (2.37)$$

where u^e is the nodal unknown vector and $\{\dot{u}\}$ represents the time derivative for the unknown. M^e, K^e and F^e are the mass matrix, stiffness matrix and force vector at an element level, respectively. For the sake of brevity, the boundary integral B^e is included in F^e. Following is the global system that is obtained after assembling the local (element level) system

$$[M]\{\dot{u}\} + [K][u] = \{F\}. \quad (2.38)$$

2.4.4 The Semi-discretization in Time

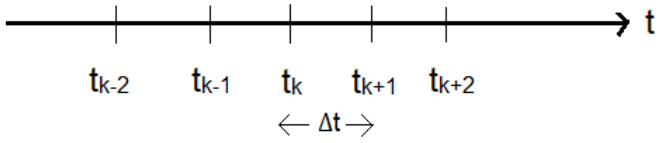

Figure 2.1: Time domain discretization.

The Eq. (2.38) is not a system of simple algebraic equations but it is a set of ordinary differential equations due to presence of the time derivative term. For time discretization, we assume the time domain given by the Figure 2.1. Initial condition gives the solution at zeroth time level $k = 0$. The solution is obtained at the next time level utilizing the information at a previous time level. Here, t_k represents the present time level where the solution is known and t_{k+1} is the next time level where we want to find the solution. Δt is the time step between the both time levels k and $k+1$. For simplicity, we will assume Δt to be constant for the full domain although it can be considered to vary with time for increasing efficiency. For discretization of the time dependent problems, following three schemes are frequently used

- Crank-Nicolson method
- Backward Euler method
- Forward Euler method

Since Crank-Nicolson method is utilized in this thesis therefore it becomes important to discuss some details of it.

2.4.4.1 The Crank-Nicolson Scheme

Following formulation serves as a base for this scheme

$$\frac{\{\dot{u}_{k+1}\} + \{\dot{u}_k\}}{2} = \frac{\{u_{k+1}\} - \{u_k\}}{\Delta t} + \mathcal{O}(\Delta t)^2. \tag{2.39}$$

It has an accuracy of order two and it is somewhat an average of forward and backward difference schemes. For its derivation, we write Eq. (2.38) for both time level k and $k+1$ in the following way

$$[M]\frac{\{u_{k+1}\}-\{u_k\}}{\Delta t}+[K]_k\{u\}_k=\{F\}_k, \tag{2.40}$$

$$[M]\frac{\{u_{k+1}\}-\{u_k\}}{\Delta t}+[K]_{k+1}\{u\}_{k+1}=\{F\}_{k+1}. \tag{2.41}$$

After multiplying these equations by $1/2$, adding them, using Eq. (2.39) to discretize the time derivative terms and rearranging them, we obtain the following form

$$\{u\}_{k+1}=\left([M]+\frac{\Delta t}{2}[K]_{k+1}\right)^{-1}\left[\left([M]-\frac{\Delta t}{2}[K]_k\right)\{u\}_k+\{u\}_k + \frac{\Delta t}{2}(\{F\}_k+\{F\}_{k+1})\right]. \tag{2.42}$$

2.5 Mixed finite Element Method

The mixed finite element method is utilized to obtain approximate solutions for coupled partial differential equations with more than one unknowns, simultaneously. We want to find the velocity, temperature and pressure from our governing equations, at the same time. So, the mixed finite element method is employed to solve the system of equations. Here, we require different finite element spaces for various unknowns. To ensure the convergence of the solution, these different spaces are interrelated in such a way that the famous discrete inf-sup condition, i.e., the Ladyzhenskaya-Babuŝka-Brezzi (LBB) condition given in expression (2.43) is satisfied [110, 111], i.e.,

$$\inf_{q_h\in Q_h}\sup_{v_h\in V_h}\frac{b(v_h,q_h)}{\|v_h\|_V\|q_h\|_Q}\geq\gamma. \tag{2.43}$$

We have solved the governing equations of **Chapter 3** in space by the nonconforming Stokes element $\widetilde{Q_1}/Q_0$ while the problems of the **Chapters 4**, **5** and **6** in space are solved by the conforming Stokes element Q_2/P_1^{disc}. A brief description of these finite element pairs is given in the following subsections.

2.5.1 The Nonconforming Stokes Element $\widetilde{Q_1}/Q_0$

When the finite element space is not a subspace of the solution space, this approach is called nonconforming. This is a recently established nonconforming rectangular element [112]. The shape function consists of four terms as $[1, x, y, x^2 - y^2]$ and there exists its four mean values along the edges of the rectangle. Let T_h be the regular decomposition of the domain $\Omega \subseteq R_n$ into quadrilaterals respectively hexahedrons denoted by T, where the mesh parameter $h > 0$ describes the maximum diameter of the elements of T_h. By ∂T_h, we denote the set of all $(n-1)$-faces Γ of the elements $T \in T_h$. The family T_h is assumed to satisfy the usual uniform shape condition. Accordingly, the generic constant c used below is always independent of h. In defining the parametric rotated multilinear element, one uses the unit n-cube (with edge parallel to the coordinate axes) as a reference element T. For each $T \in T_h$, let $\psi_T : \hat{T} \to T$ be the corresponding n-linear $1-1$ transformation. We set

$$\widetilde{Q}_1(T) \;=\; \{q \circ \psi_T^{-1} : q \in \text{span } (1, x_i, x_{i+1}, x_i^2 - x_{i+1}^2, i = 1, ..., n)\}. \tag{2.44}$$

The parametric rotated multilinear element has a nonparametric counter part. For any element $T \in T_h$, let $\{\xi_i\}$ denote a coordinate system which is obtained by connecting the center points of any two opposite $(n-1)$-faces of T. Since the mesh family T_h is uniformly regular, the linear transformation between $\{x_i\}$ and the Cartesian system $\{\xi_i\}$ is bounded independently of h. On each $T \in T_h$, we set

$$\widetilde{Q}_1(T) = \{q \circ \psi_T^{-1} : q \in \text{span}(1, \xi_i, \xi_{i+1}, \xi_i^2 - \xi_{i+1}^2, i = 1, ..., n)\}. \tag{2.45}$$

The Q_0 element consists of a quadrilateral with constant interpolation.

2.5.2 The Conforming Stokes Element Q_2/P_1^{disc}

The domain is discretized into a number of non-overlapping quadrilateral elements Ω_n, $n \in \mathbb{N}$. The biquadratic element Q_2 [113] is defined on each quadrilateral with 9 degrees of freedom as shown in Figure 2.2. Moreover, we use a reference coordinate system (ξ, η) for the construction of local shape function on the physical element. Now, we define a bilinear mapping between the physical and reference element by $G_n : \widetilde{\Omega}_n \to \Omega_n$. The inverse mapping $G_n^{-1} : \Omega_n \to \widetilde{\Omega}_n$ is applied to get back to the physical coordinate system (x, y). Figure 2.2 demonstrates both the physical and reference coordinate systems. The value of shape function on each node is defined by

$$\widetilde{\phi}_j(\widetilde{x}_i) = \delta_{ij} = \begin{cases} 1 & if \quad j = i \\ 0 & if \quad j \neq i, \end{cases}$$

where $\widetilde{x}_i \in \widetilde{\Omega}_n$ denotes the ith node in $\widetilde{\Omega}_n$. These nine shape functions are biquadratic polynomials and can be expressed by $\{1, \xi, \eta, \xi\eta, \xi^2, \eta^2, \xi^2\eta, \xi\eta^2, \xi^2\eta^2\}$ where $-1 \leq \xi \leq 1$ and $-1 \leq \eta \leq 1$. Then, the space $Q_2(\Omega_n)$ on the physical element is defined by

$$Q_2(\Omega_n) = \{h \circ G_n^{-1} : h \in \text{span } \{1, x, y, xy, x^2, y^2, x^2y, xy^2, x^2y^2\}\} \tag{2.46}$$

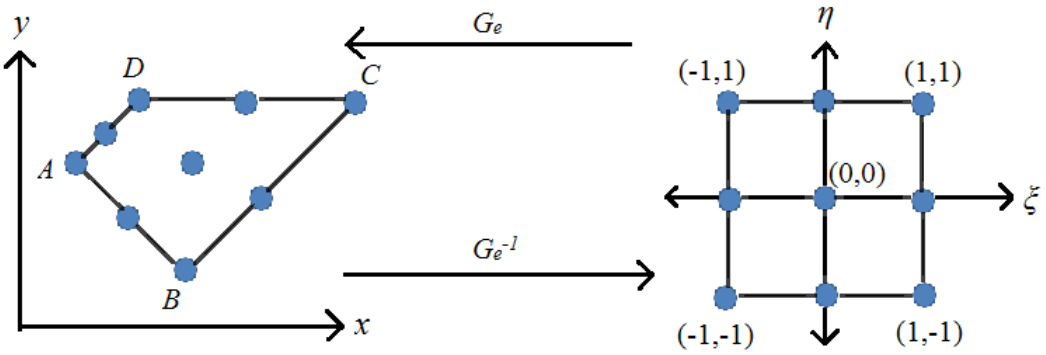

Figure 2.2: Mapping between biquadratic physical and reference element.

The discontinuous P_1 finite element space contains piecewise polynomials which are discontinuous across the boundaries that are common to the other element.

Three degrees of freedom exist at the centre of each element as shown in Figure 2.3. In mapped approach, the shape function on the reference element can be expressed in the following way

$$\widetilde{\phi}_1(\xi,\eta) = 1,$$

$$\widetilde{\phi}_2(\xi,\eta) = \xi,$$

$$\widetilde{\phi}_3(\xi,\eta) = \eta.$$

The space $P_1(\Omega_n)$ on the physical element, is defined by

$$P_1(\Omega_n) = \{h \circ G_n^{-1} : h \in \text{span}\{1, x, y\}\}. \tag{2.47}$$

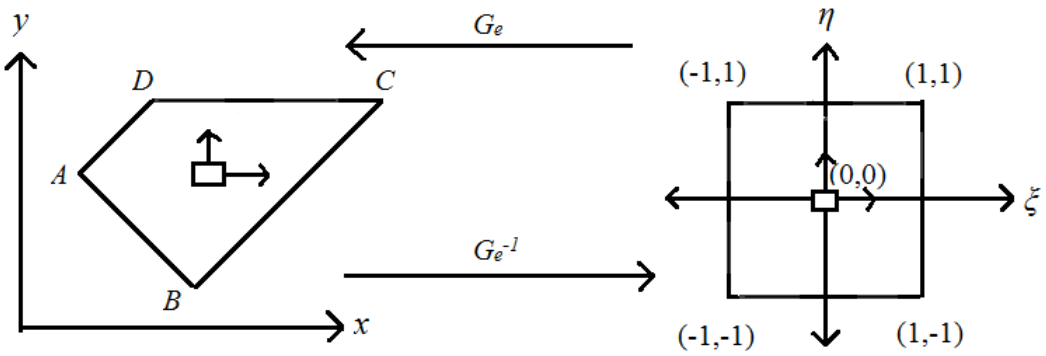

Figure 2.3: Mapping between discontinuous P_1 physical and reference element.

Chapter 3

Mixed Convective Nanofluid Flow in a Cavity

3.1 Introduction

In this chapter, numerical simulations are performed to examine the effect of inclination on the heat transfer of Al_2O_3–water nanofluid for mixed convection flow in a partially heated double lid driven inclined cavity. Two heat sources are affixed at some portion of the bottom wall of the cavity while the remaining part of this wall is considered as adiabatic. The moving vertical walls and the top wall are kept at constant cold temperature. Buoyant force is responsible for the flow along with two moving vertical walls. The governing equations are discretized with the help of finite element method in space and the Crank-Nicolson in time. Newton's method is utilized to linearize the system of nonlinear equations and the associated linear system is solved by the Gaussian elimination method in each time level. Numerical results are presented and analyzed by means of streamlines, isotherms, tables and some useful plots. Impact of emerging parameters on the flow, in specific ranges such as Reynolds number ($1 \leq Re \leq 100$), Richardson number ($0.01 \leq Ri \leq 10$), nanoparticle volume fraction ($0 \leq \phi \leq 0.04$) as well as inclination angle of cavity ($0^\circ \leq \psi \leq 45^\circ$) are investigated and findings are

exactly of the same order as that of the previously performed analysis in the literature. Calculations of average Nusselt number, average temperature, average entropy generation due to heat transfer and fluid friction and kinetic energy are the main focus of this chapter. This study is organised in the following way: Section 3.2 illustrates the problem configuration. Section 3.3 contains information about space and time discretizations of the governing equations, the numerical method, code validation and grid independence test. Results based on the numerical simulation have been elaborated in Section 3.4. Finally, conclusion has been drawn in Section 3.5.

3.2 Problem Formulation

3.2.1 The Problem Configuration

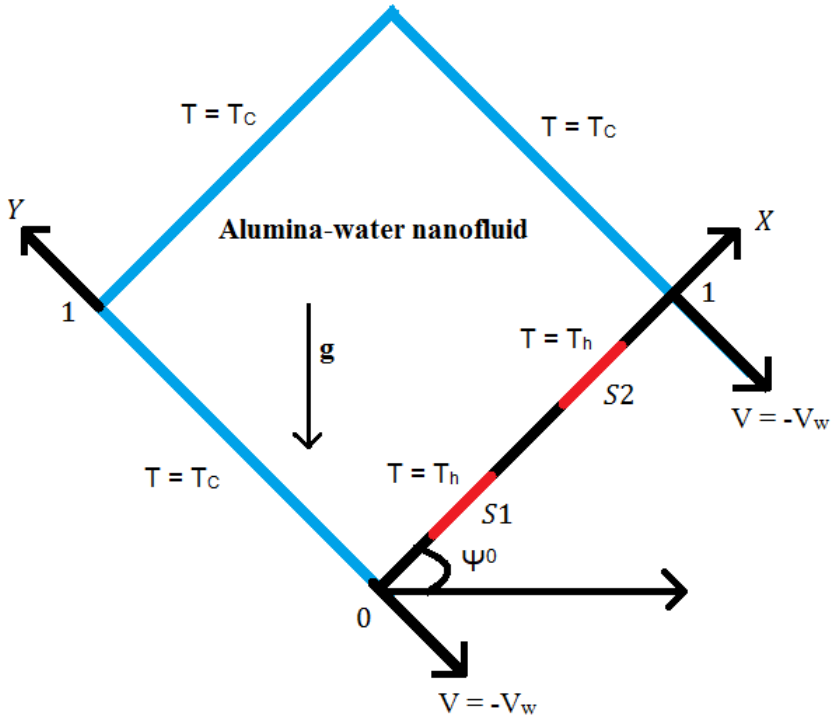

Figure 3.1: Schematic diagram of the physical model.

We consider a lid driven square cavity inclined at an angle ψ and filled with nanofluid that is unsteady and incompressible. Two heat sources are fixed along

Physical properties	H_2O	Al_2O_3
ρ (kg m^{-3})	997.1	3970
C_p (J kg^{-1}K^{-1})	4179	765
k (W m^{-1} K^{-1})	0.613	25
β (K^{-1})	21×10^{-5}	1.89×10^{-5}
d_p (nm)	-	47

Table 3.1: Thermo-physical properties of water and alumina [37].

the wall at the bottom at constant temperature (see Figure 3.1). L represents the width of the cavity, while T_h is the prescribed constant hot temperature, T_c is the constant cold temperature. Distance of heat sources from both the side walls is the same. It is assumed that the slipping effect between any two phases is negligible. Viscous dissipation in the energy equation is neglected [93, 96]. Nanoparticles used during this study have certain thermo-physical properties [114–116] that are tabulated in Table 3.1. Density variation is taken into consideration by using the Boussinesq approximation which is apparent as the buoyancy force.

3.2.2 The Governing Equations

Governing equations of continuity, momentum and energy [37] under the above-mentioned assumptions are given by

$$\frac{\partial u}{\partial t} + u\frac{\partial u}{\partial x} + v\frac{\partial u}{\partial y} = -\frac{1}{\rho_{nf}}\frac{\partial p}{\partial x} + \frac{\mu_{nf}}{\rho_{nf}}\left(\frac{\partial^2 u}{\partial x^2} + \frac{\partial^2 u}{\partial y^2}\right) + \frac{(\rho\beta)_{nf}}{\rho_{nf}} g(T - T_c)\,\sin\psi, \tag{3.1}$$

$$\frac{\partial v}{\partial t} + u\frac{\partial v}{\partial x} + v\frac{\partial v}{\partial y} = -\frac{1}{\rho_{nf}}\frac{\partial p}{\partial y} + \frac{\mu_{nf}}{\rho_{nf}}\left(\frac{\partial^2 v}{\partial x^2} + \frac{\partial^2 v}{\partial y^2}\right) + \frac{(\rho\beta)_{nf}}{\rho_{nf}} g(T - T_c)\,\cos\psi, \tag{3.2}$$

$$\frac{\partial u}{\partial x} + \frac{\partial v}{\partial y} = 0, \tag{3.3}$$

$$\frac{\partial T}{\partial t} + u\frac{\partial T}{\partial x} + v\frac{\partial T}{\partial y} = \alpha_{nf}\left(\frac{\partial^2 T}{\partial x^2} + \frac{\partial^2 T}{\partial y^2}\right). \tag{3.4}$$

3.2.3 The Dimensionless Governing Equations

Problem variables regarding the non-dimensional form are implemented as follows

$$X = \frac{x}{L},\ Y = \frac{y}{L},\ U = \frac{u}{V_w},\ V = \frac{v}{V_w},\ \theta = \frac{T-T_c}{T_h-T_c},\ P = \frac{p}{\rho_{nf}V_w^2},\ \tau = \frac{tV_w}{L},$$
$$Re = \frac{V_wL}{\nu_f},\ Gr = \frac{g\beta\Delta TL^3}{\nu_f^2},\ Pr = \frac{\nu_f}{\alpha_f},\ Ri = \frac{Gr}{Re^2},\ S_T = s\frac{T_0^2L^2}{k_f(T_h-T_c)^2},$$

where V_w, ν_f, α_f and β are imposed lid velocity, kinematic viscosity, thermal diffusibility and the coefficient of thermal expansion of nanofluid, respectively. Dimensionless governing equations could be given as follows

$$\frac{\partial U}{\partial \tau} + U\frac{\partial U}{\partial X} + V\frac{\partial U}{\partial Y} = -\frac{\partial P}{\partial X} + \frac{1}{Re}\frac{\rho_f}{\rho_{nf}}\frac{1}{(1-\phi)^{2.5}}\left(\frac{\partial^2 U}{\partial X^2} + \frac{\partial^2 U}{\partial Y^2}\right) + Ri\frac{\rho_f}{\rho_{nf}}\left(1-\phi+\frac{\rho_s\beta_s\phi}{\rho_f\beta_f}\right)(\sin\psi)\theta, \tag{3.5}$$

$$\frac{\partial V}{\partial \tau} + U\frac{\partial V}{\partial X} + V\frac{\partial V}{\partial Y} = -\frac{\partial P}{\partial Y} + \frac{1}{Re}\frac{\rho_f}{\rho_{nf}}\frac{1}{(1-\phi)^{2.5}}\left(\frac{\partial^2 V}{\partial X^2} + \frac{\partial^2 V}{\partial Y^2}\right) + Ri\frac{\rho_f}{\rho_{nf}}\left(1-\phi+\frac{\rho_s\beta_s\phi}{\rho_f\beta_f}\right)(\cos\psi)\theta, \tag{3.6}$$

$$\frac{\partial U}{\partial X} + \frac{\partial V}{\partial Y} = 0, \tag{3.7}$$

$$\frac{\partial \theta}{\partial \tau} + U\frac{\partial \theta}{\partial X} + V\frac{\partial \theta}{\partial Y} = \frac{\alpha_{nf}}{\alpha_f}\frac{1}{RePr}\left(\frac{\partial^2 \theta}{\partial X^2} + \frac{\partial^2 \theta}{\partial Y^2}\right) . \tag{3.8}$$

Associated with the problem, the boundary conditions are given by

$U = 0,\quad V = -1,\quad \theta = 0,\quad$ for $\quad X = 0,\ 1\quad$ and $\quad 0 \le Y \le 1,$

$U = 0,\quad V = 0,\quad \theta = 0,\quad$ for $\quad 0 \le X \le 1\quad$ and $\quad Y = 1,$

$$U = V = 0,\ \theta = 1 \text{ for } \begin{cases} 0.2 \le X \le 0.4, \\ 0.6 \le X \le 0.8 \quad \text{and } Y = 0, \end{cases}$$

$$U = V = 0,\ \frac{\partial \theta}{\partial Y} = 0 \text{ for } \begin{cases} 0 \le X \le 0.2, \\ 0.4 \le X \le 0.6 \quad \text{and } Y = 0, \\ 0.8 \le X \le 1. \end{cases}$$

3.2.4 The Effective Nanofluid Properties

The effective density, thermal diffusivity, specific heat and the coefficient of thermal expansion of the nanofluid [114, 115] could be expressed as follows

$$\rho_{nf} = (1-\phi)\,\rho_f + \phi\rho_p, \tag{3.9}$$

$$\alpha_{nf} = \frac{k_{nf}}{(\rho C_p)_{nf}}, \tag{3.10}$$

$$(\rho C_p)_{nf} = (1-\phi)\,(\rho C_p)_f + \phi(\rho C_p)_p, \tag{3.11}$$

$$(\rho\beta)_{nf} = (1-\phi)\,(\rho\beta)_f + \phi\,(\rho\beta)_p. \tag{3.12}$$

The Brownian motion has considerable influence on the thermal conductivity of the nanofluid. Koo and Kleinstreuer [117] proposed the following model for effective thermal conductivity

$$k_{eff} = k_{static} + k_{Brownian}, \tag{3.13}$$

$$k_{static} = k_f\left[1 + \frac{3\,(k_p/k_f - 1)\,\phi}{(k_p/k_f + 2) - (k_p/k_f - 1)\,\phi}\right], \tag{3.14}$$

where k_p, k_f are the thermal conductivities of the solid nanosized particles and pure fluid, respectively, k_{static} is the static thermal conductivity based on the Maxwell [118] model, and $k_{Brownian}$ is the thermal conductivity proposed by the KKL model, given by

$$k_{Brownian} = 5\times 10^4\phi\rho_f(C_p)_f\sqrt{\frac{\kappa_b T}{\rho_p d_p}}g'(T,\phi,d_p), \tag{3.15}$$

where the empirical function g' for the Al_2O_3-water nanofluid can be given by

$$\begin{aligned} g'(T,\phi,d_p) = {} & (a_1 + a_2\ln(d_p) + a_3\ln(\phi) + a_4\ln(\phi)\ln(d_p) + a_5\ln(d_p)^2)\ln(T) \\ & + (a_6 + a_7\ln(d_p) + a_8\ln(\phi) + a_9\ln(d_p)\ln(\phi) + a_{10}\ln(d_p)^2), \end{aligned} \tag{3.16}$$

with the coefficients $a_i (i = 1, 2, ..., 10)$ being tabulated in Table 3.2. Koo and Kleinstreuer [119] further proposed the following model for the effective viscosity

due to micromixing in suspensions

$$\mu_{eff} = \mu_{static} + \mu_{Brownian} = \mu_{static} + \frac{k_{Brownian}}{k_f} \times \frac{\mu_f}{Pr_f}, \tag{3.17}$$

where $\mu_{static} = \mu_f/(1-\phi)^{2.5}$ is the viscosity of the nanofluid as given by the Brinkman model [120]. Also, by incorporating the interfacial thermal resistence $R_f = 4 \times 10^{-8}\text{m}^2\text{K/W}$, the original k_p in Eq. (3.14) is replaced by $k_{p,eff}$ in the form

$$R_f + \frac{d_p}{k_p} = \frac{d_p}{k_{p,eff}}. \tag{3.18}$$

Coefficients values	Al_2O_3-water
a_1	52.813488759
a_2	6.115637295
a_3	0.6955745084
a_4	0.041745555278
a_5	0.176919300241
a_6	-298.19819084
a_7	-34.532716906
a_8	-3.9225289283
a_9	-0.2354329626
a_{10}	-0.999063481

Table 3.2: The coefficients values of alumina-water nanofluid [22].

3.2.5 The Entropy Generation

The entropy generation due to various physical sources can be written as follows:

$$s = \frac{k_{nf}}{T_0^2}\left[\left(\frac{\partial T}{\partial x}\right)^2 + \left(\frac{\partial T}{\partial y}\right)^2\right] + \frac{\mu_{nf}}{T_0}\left[2\left(\left(\frac{\partial u}{\partial x}\right)^2 + \left(\frac{\partial v}{\partial y}\right)^2\right)\right] + \left[\frac{\mu_{nf}}{T_0}\left(\frac{\partial u}{\partial y} + \frac{\partial v}{\partial x}\right)^2\right], \tag{3.19}$$

where $T_0 = \frac{T_h + T_c}{2}$. The dimensionless entropy generation obtained from Eq. (3.19) is given as follows:

$$S_T = \frac{k_{nf}}{k_f}\left[\left(\frac{\partial\theta}{\partial X}\right)^2 + \left(\frac{\partial\theta}{\partial Y}\right)^2\right] + \chi\frac{\mu_{nf}}{\mu_f}\left[2\left(\left(\frac{\partial U}{\partial X}\right)^2 + \left(\frac{\partial V}{\partial Y}\right)^2\right)\right] + \chi\frac{\mu_{nf}}{\mu_f}\left[\left(\frac{\partial U}{\partial Y} + \frac{\partial V}{\partial X}\right)^2\right], \tag{3.20}$$

where χ is the irreversibility factor . It is expressed in the following

$$\chi = \frac{\mu_f T_0}{k_f}\left(\frac{V_w}{T_h - T_c}\right)^2. \tag{3.21}$$

Let us write

$$S_T = S_{HT} + S_{FF}, \tag{3.22}$$

where

$$S_{HT} = \frac{k_{nf}}{k_f}\left[\left(\frac{\partial\theta}{\partial X}\right)^2 + \left(\frac{\partial\theta}{\partial Y}\right)^2\right]. \tag{3.23}$$

Here

$$S_{FF} = \chi\frac{\mu_{nf}}{\mu_f}\left[2\left(\left(\frac{\partial U}{\partial X}\right)^2 + \left(\frac{\partial V}{\partial Y}\right)^2\right) + \left(\frac{\partial U}{\partial Y} + \frac{\partial V}{\partial X}\right)^2\right], \tag{3.24}$$

where S_{HT} and S_{FF} represent the non-dimensional entropy generation due to the heat transfer and fluid friction, respectively. Integrating Eq. (3.20) yields the dimensionless average entropy generation $S_{T,\text{avg}}$ that could be given as follows

$$S_{T,\text{avg}} = \frac{1}{\vartheta}\int S_T d\vartheta = S_{HT,\text{avg}} + S_{FF,\text{avg}}. \tag{3.25}$$

Here, total volume of the nanofluid is represented by ϑ, $S_{HT,\text{avg}}$ and $S_{FF,\text{avg}}$ are respectively the dimensionless average entropy generation for heat transfer and fluid friction.

3.2.6 Calculation of the Nusselt Number

To determine the heat transfer characteristics, we are interested in computing local and average Nusselt number on both of the discrete heat sources. Local Nusselt number on each of the heat sources is given by

$$Nu = \frac{h_{nf} L}{k_f}, \tag{3.26}$$

where h_{nf} is the heat transfer coefficient formulated as

$$h_{nf} \;=\; \frac{q}{T_h - T_c}. \tag{3.27}$$

Here q is the wall heat flux per unit area given by

$$q \;=\; -\,k_{nf} \frac{(T_h - T_c)}{L} \frac{\partial \theta}{\partial Y}\bigg|_{Y=0}. \tag{3.28}$$

As a result,

$$Nu = -\frac{k_{nf}}{k_f} \left(\frac{\partial \theta}{\partial Y} \right), \tag{3.29}$$

$$Nu_{\text{avg},S1} = \int_{0.2}^{0.4} Nu \; dX, \text{ and } Nu_{\text{avg},S2} = \int_{0.6}^{0.8} Nu \; dX. \tag{3.30}$$

The overall surface average Nusselt number can be calculated as $Nu_{\text{avg},S1} + Nu_{\text{avg},S2}$.

3.3 The Numerical Approach

3.3.1 Spatial and Temporal Discretization

The system of coupled non-linear partial dierential equations together with given boundary conditions have been discretized numerically by the finite element formulation. The numerical procedure used to solve the governing equations for the present work is based on the Galerkin weighted residual method in which we have used the nonconforming Stokes element $\widetilde{Q}_1/Q_0$, where $\widetilde{Q}_1$ element is utilized for

the velocity and temperature and Q_0 element is used for the pressure (see 2.5 for detail). The variational or weak form of the governing Eqs. (3.5) - (3.8) is given in the following:

$$\begin{aligned}
&\int_\Omega \frac{\partial U}{\partial \tau} w \; d\Omega + \int_\Omega \left(U\frac{\partial U}{\partial X} + V\frac{\partial U}{\partial Y} \right) w \; d\Omega = -\int_\Omega \frac{\partial P}{\partial X} w \; d\Omega \\
&+ \frac{1}{Re}\frac{\rho_f}{\rho_{nf}}\frac{1}{(1-\phi)^{2.5}} \int_\Omega \left(\frac{\partial^2 U}{\partial X^2} + \frac{\partial^2 U}{\partial Y^2} \right) w \; d\Omega \\
&+ Ri\frac{\rho_f}{\rho_{nf}} \left(1 - \phi + \frac{\rho_s \beta_s \phi}{\rho_f \beta_f} \right) (\sin\psi) \int_\Omega \theta w \; d\Omega \qquad , \quad (3.31) \\
&\int_\Omega \frac{\partial V}{\partial \tau} w \; d\Omega + \int_\Omega \left(U\frac{\partial V}{\partial X} + V\frac{\partial V}{\partial Y} \right) w \; d\Omega = -\int_\Omega \frac{\partial P}{\partial Y} w \; d\Omega \\
&+ \frac{1}{Re}\frac{\rho_f}{\rho_{nf}}\frac{1}{(1-\phi)^{2.5}} \int_\Omega \left(\frac{\partial^2 V}{\partial X^2} + \frac{\partial^2 V}{\partial Y^2} \right) w \; d\Omega \\
&+ Ri\frac{\rho_f}{\rho_{nf}} \left(1 - \phi + \frac{\rho_s \beta_s \phi}{\rho_f \beta_f} \right) (\cos\psi) \int_\Omega \theta w \; d\Omega, \qquad (3.32) \\
&\int_\Omega \left(\frac{\partial U}{\partial X} + \frac{\partial V}{\partial Y} \right) q \; d\Omega = 0, \qquad (3.33) \\
&\int_\Omega \frac{\partial \theta}{\partial \tau} w \; d\Omega + \int_\Omega \left(U\frac{\partial \theta}{\partial X} + V\frac{\partial \theta}{\partial Y} \right) w \; d\Omega \\
&= \frac{\alpha_{nf}}{\alpha_f}\frac{1}{RePr} \int_\Omega \left(\frac{\partial^2 \theta}{\partial X^2} + \frac{\partial^2 \theta}{\partial Y^2} \right) w \; d\Omega \qquad . \quad (3.34)
\end{aligned}$$

Now, the infinite dimensional trial spaces U, V, θ and P are approximated by U_h, V_h, θ_h and P_h, respectively. Moreover, the infinite dimensional test spaces W and Q are approximated by the finite dimensional test spaces W_h and Q_h, respectively, in such a way that

$$\begin{aligned}
w_h \in W_h \subset H^1(\Omega) &= \left\{ s : \Omega \to \mathbb{R} : \int_\Omega |s(x)|^2 dx < \infty, \int_\Omega |s'(x)|^2 dx < \infty \right\}, \\
q_h \in Q_h \subset L_2(\Omega) &= \left\{ g : \Omega \to \mathbb{R} : \int_\Omega |g(x)|^2 dx < \infty \right\}.
\end{aligned}$$

After the finite dimensional approximation the Eqs. (3.31) - (3.34) takes the form, given as follows:

$$\int_\Omega \frac{\partial U_h}{\partial \tau} w_h \; d\Omega + \int_\Omega \left(U_h\frac{\partial U_h}{\partial X} + V_h\frac{\partial U_h}{\partial Y} \right) w_h \; d\Omega = -\int_\Omega \frac{\partial P_h}{\partial X} w_h \; d\Omega$$

$$+\frac{1}{Re}\frac{\rho_f}{\rho_{nf}}\frac{1}{(1-\phi)^{2.5}}\int_\Omega\left(\frac{\partial^2 U_h}{\partial X^2}+\frac{\partial^2 U_h}{\partial Y^2}\right)w_h\ d\Omega$$
$$+Ri\frac{\rho_f}{\rho_{nf}}\left(1-\phi+\frac{\rho_s\beta_s\phi}{\rho_f\beta_f}\right)(\sin\psi)\int_\Omega\theta_h w_h\ d\Omega, \tag{3.35}$$
$$\int_\Omega\frac{\partial V_h}{\partial\tau}w_h\ d\Omega+\int_\Omega\left(U_h\frac{\partial V_h}{\partial X}+V_h\frac{\partial V_h}{\partial Y}\right)w_h\ d\Omega=-\int_\Omega\frac{\partial P_h}{\partial Y}w_h\ d\Omega$$
$$+\frac{1}{Re}\frac{\rho_f}{\rho_{nf}}\frac{1}{(1-\phi)^{2.5}}\int_\Omega\left(\frac{\partial^2 V_h}{\partial X^2}+\frac{\partial^2 V_h}{\partial Y^2}\right)w_h\ d\Omega$$
$$+Ri\frac{\rho_f}{\rho_{nf}}\left(1-\phi+\frac{\rho_s\beta_s\phi}{\rho_f\beta_f}\right)(\cos\psi)\int_\Omega\theta_h w_h\ d\Omega, \tag{3.36}$$
$$\int_\Omega\left(\frac{\partial U_h}{\partial X}+\frac{\partial V_h}{\partial Y}\right)q_h\ d\Omega=0, \tag{3.37}$$
$$\int_\Omega\frac{\partial\theta_h}{\partial\tau}w_h\ d\Omega+\int_\Omega\left(U_h\frac{\partial\theta}{\partial X}+V_h\frac{\partial\theta_h}{\partial Y}\right)w_h\ d\Omega$$
$$=\frac{\alpha_{nf}}{\alpha_f}\frac{1}{RePr}\int_\Omega\left(\frac{\partial^2\theta_h}{\partial X^2}+\frac{\partial^2\theta_h}{\partial Y^2}\right)w_h\ d\Omega\quad. \tag{3.38}$$

Using the FEM approximation $U_h(\tau,X,Y)=\sum_{j=1}^{N}U_j(\tau)\xi_j(X,Y)$, $V_h(\tau,X,Y)=\sum_{j=1}^{N}V_j(\tau)\xi_j(X,Y)$, $\theta_h(\tau,X,Y)=\sum_{j=1}^{N}\theta_j(\tau)\xi_j(X,Y)$ and $P_h(X,Y)=\sum_{j=1}^{K}P_j\eta_j(X,Y)$ are the trial functions, similarly $w_h=\sum_{i=1}^{N}w_i\ \xi_i$ and $q_h=\sum_{i=1}^{K}q_i\ \eta_i$ are the test functions. By the Galerkin finite element model for a typical element Ω_e, the Eqs. (3.35) - (3.38) are transformed into the following system:

$$\int_{\Omega_e}\frac{\partial U_j}{\partial\tau}\xi_j\xi_i d\Omega_e+U_j\int_{\Omega_e}\left(\overline{U}\xi_i\frac{\partial\xi_j}{\partial X}+\overline{V}\xi_i\frac{\partial\xi_j}{\partial Y}\right)d\Omega_e=P_j\int_{\Omega_e}\eta_j\frac{\partial\xi_i}{\partial X}d\Omega_e$$
$$+\frac{1}{Re}\frac{\rho_f}{\rho_{nf}}\frac{1}{(1-\phi)^{2.5}}U_j\int_{\Omega_e}\left(\frac{\partial\xi_j}{\partial X}\frac{\partial\xi_i}{\partial X}+\frac{\partial\xi_j}{\partial Y}\frac{\partial\xi_i}{\partial Y}\right)d\Omega_e$$
$$+Ri\frac{\rho_f}{\rho_{nf}}\left(1-\phi+\frac{\rho_s\beta_s}{\rho_f\beta_f}\phi\right)\sin\psi\theta_j\int_{\Omega_e}\xi_j\xi_i d\Omega_e, \tag{3.39}$$
$$\int_{\Omega_e}\frac{\partial V_j}{\partial\tau}\xi_j\xi_i d\Omega_e+V_j\int_{\Omega_e}\left(\overline{U}\xi_i\frac{\partial\xi_j}{\partial X}+\overline{V}\xi_i\frac{\partial\xi_j}{\partial Y}\right)d\Omega_e=P_j\int_{\Omega_e}\eta_j\frac{\partial\xi_i}{\partial Y}d\Omega_e$$
$$+\frac{1}{Re}\frac{\rho_f}{\rho_{nf}}\frac{1}{(1-\phi)^{2.5}}V_j\int_{\Omega_e}\left(\frac{\partial\xi_j}{\partial X}\frac{\partial\xi_i}{\partial X}+\frac{\partial\xi_j}{\partial Y}\frac{\partial\xi_i}{\partial Y}\right)d\Omega_e$$
$$+Ri\frac{\rho_f}{\rho_{nf}}\left(1-\phi+\frac{\rho_s\beta_s}{\rho_f\beta_f}\phi\right)\cos\psi\theta_j\int_{\Omega_e}\xi_j\xi_i d\Omega_e, \tag{3.40}$$
$$U_j\int_{\Omega_e}\frac{\partial\xi_j}{\partial X}\eta_i\ d\Omega_e+V_j\int_{\Omega_e}\frac{\partial\xi_j}{\partial Y}\eta_i\ d\Omega_e=0, \tag{3.41}$$

$$\int_{\Omega_e} \frac{\partial \theta_j}{\partial \tau} \xi_j \xi_i d\Omega_e + \theta_j \int_{\Omega_e} \left(\overline{U} \xi_i \frac{\partial \xi_j}{\partial X} + \overline{V} \xi_i \frac{\partial \xi_j}{\partial Y} \right) \, d\Omega_e$$
$$= \frac{1}{RePr} \theta_j \int_{\Omega_e} \left(\frac{\partial \xi_j}{\partial X} \frac{\partial \xi_i}{\partial X} + \frac{\partial \xi_j}{\partial Y} \frac{\partial \xi_i}{\partial Y} \right) \, d\Omega_e. \tag{3.42}$$

The final system can be expressed in the following comprehensive form:

$$[\mathbf{M^e}]\{\dot{\mathbf{u}}^\mathbf{e}\} + [\mathbf{K^e}][\mathbf{u^e}] = \{\mathbf{F^e}\}, \tag{3.43}$$

$$[\mathbf{M^e}]\{\dot{\mathbf{u}}^\mathbf{e}\} + \underbrace{\begin{bmatrix} [K_{ji}^{11}] & [K_{ji}^{12}] & [K_{ji}^{13}] & [K_{ji}^{14}] \\ [K_{ji}^{21}] & [K_{ji}^{22}] & [K_{ji}^{23}] & [K_{ji}^{24}] \\ [K_{ji}^{31}] & [K_{ji}^{32}] & [K_{ji}^{33}] & [K_{ji}^{34}] \\ [K_{ji}^{41}] & [K_{ji}^{42}] & [K_{ji}^{43}] & [K_{ji}^{44}] \end{bmatrix}}_{\mathbf{K^e}} \underbrace{\begin{bmatrix} \{\underline{U}\} \\ \{\underline{V}\} \\ \{\underline{P}\} \\ \{\underline{\theta}\} \end{bmatrix}}_{\mathbf{u^e}} = \underbrace{\begin{bmatrix} \{\underline{F^1}\} \\ \{\underline{F^2}\} \\ \{\underline{F^3}\} \\ \{\underline{F^4}\} \end{bmatrix}}_{\mathbf{F^e}}, \tag{3.44}$$

where

$$[\mathbf{M^e}] = \begin{bmatrix} [M_{ji}^{11}] & [M_{ji}^{12}] & [M_{ji}^{13}] & [M_{ji}^{14}] \\ [M_{ji}^{21}] & [M_{ji}^{22}] & [M_{ji}^{23}] & [M_{ji}^{24}] \\ [M_{ji}^{31}] & [M_{ji}^{32}] & [M_{ji}^{33}] & [M_{ji}^{34}] \\ [M_{ji}^{41}] & [M_{ji}^{42}] & [M_{ji}^{43}] & [M_{ji}^{44}] \end{bmatrix} \tag{3.45}$$

In the above expression (3.45), $[\mathbf{M^e}]$ is the elemental block mass matrix in which all the block matrices are zero except $[M_{ji}^{11}] = [M_{ji}^{22}] = [M_{ji}^{44}] = M = \int_{\Omega_e} \xi_j \xi_i \, d\Omega_e$ where the variation of i and j depends on the choice of the basis function and the geometric element considered. Furthermore, $\{\dot{\mathbf{u}}^\mathbf{e}\}$, $\mathbf{K^e}$, $\mathbf{u^e}$ and $\mathbf{F^e}$ in the expression (3.44) are said to be the time derivative vector for the nodal unknowns, the stiffness block matrix, the block solution vector for the nodal unknowns and the right hand side block vector at an element level, respectively. For the sake of brevity, the boundary integral is also included in $\mathbf{F^e}$. In stiffness block matrix,

$$K_{ji}^{11} = \frac{1}{Re} \frac{\rho_f}{\rho_{nf}} \frac{1}{(1-\phi)^{2.5}} \int_{\Omega_e} \left(\left(\frac{\partial \xi_j}{\partial X} \frac{\partial \xi_i}{\partial X} + \frac{\partial \xi_j}{\partial Y} \frac{\partial \xi_i}{\partial Y} \right) + \left(\overline{U} \xi_i \frac{\partial \xi_j}{\partial X} + \overline{V} \xi_i \frac{\partial \xi_j}{\partial Y} \right) \right) \, d\Omega_e,$$
$$K_{ji}^{22} = \frac{1}{Re} \frac{\rho_f}{\rho_{nf}} \frac{1}{(1-\phi)^{2.5}} \int_{\Omega_e} \left(\left(\frac{\partial \xi_j}{\partial X} \frac{\partial \xi_i}{\partial X} + \frac{\partial \xi_j}{\partial Y} \frac{\partial \xi_i}{\partial Y} \right) + \left(\overline{U} \xi_i \frac{\partial \xi_j}{\partial X} + \overline{V} \xi_i \frac{\partial \xi_j}{\partial Y} \right) \right) \, d\Omega_e,$$

$$K_{ji}^{44} = \frac{\alpha_{nf}}{\alpha_f}\frac{1}{RePr}\int_{\Omega_e}\left(\frac{\partial\xi_j}{\partial X}\frac{\partial\xi_i}{\partial X}+\frac{\partial\xi_j}{\partial Y}\frac{\partial\xi_i}{\partial Y}\right)\,d\Omega_e+\int_{\Omega_e}\left(\overline{U}\xi_i\frac{\partial\xi_j}{\partial X}+\overline{V}\xi_i\frac{\partial\xi_j}{\partial Y}\right)\,d\Omega_e \quad ,$$

$$K_{ji}^{14} = -Ri\frac{\rho_f}{\rho_{nf}}\left(1-\phi+\frac{\rho_s\beta_s\phi}{\rho_f\beta_f}\right)\sin\psi\int_{\Omega_e}\xi_j\xi_i\,d\Omega_e \quad ,$$

$$K_{ji}^{24} = -Ri\frac{\rho_f}{\rho_{nf}}\left(1-\phi+\frac{\rho_s\beta_s\phi}{\rho_f\beta_f}\right)\cos\psi\int_{\Omega_e}\xi_j\xi_i\,d\Omega_e,$$

$$K_{ji}^{13} = -\int_{\Omega_e}\eta_j\frac{\partial\xi_i}{\partial X}d\Omega_e,$$

$$K_{ji}^{23} = -\int_{\Omega_e}\eta_j\frac{\partial\xi_i}{\partial Y}d\Omega_e,$$

$$K_{ji}^{31} = \int_{\Omega_e}\frac{\partial\xi_j}{\partial X}\eta_i d\Omega_e,$$

$$K_{ji}^{32} = \int_{\Omega_e}\frac{\partial\xi_j}{\partial Y}\eta_i d\Omega_e,$$

$$K_{ji}^{12} = K_{ji}^{21} = K_{ji}^{33} = K_{ji}^{34} = K_{ji}^{41} = K_{ji}^{42} = K_{ji}^{43} = 0,$$

$$\overline{U} = \sum_{j=1}^{N} U_j\xi_j, \overline{V} = \sum_{j=1}^{N} V_j\xi_j.$$

The above system (3.44) involves the nodal unknowns $\mathbf{u^e}$ and the time dependent terms $\{\dot{\mathbf{u}}^{\mathbf{e}}\}$. Time discretization of the nodal unknowns still remains to do. Time discretization has been performed by utilizing the Crank-Nicolson method (see 2.4 for detail). We have utilized $\widetilde{Q}_1/Q_0$, for space discretization (see 2.5 for detail). After discretization in space and time, we obtain an algebraic system of nonlinear equations. Integration regarding each term of these equations is performed by Gaussian quadrature method. Then implementation of boundary conditions is carried out and the linear algebraic equations are obtained from nonlinear equations by using the iterative Newton method. Some tolerance value is prescribed to see the optimised minimum difference of the current values of the variables to the previous iteration values by achieving the convergence of the solution of an iterative scheme. In other words, the adopted criterion to stop the iterative scheme could be given as follows

$$\left|\frac{\Gamma^{n+1}-\Gamma^n}{\Gamma^{n+1}}\right| \leq 10^{-6}, \tag{3.46}$$

where U, V, P or θ are denoted by a general variable Γ. Superscript n represents the iteration number in the above expression. Finally, these linear equations are

computed by the Gaussian elimination method in each time level.

3.3.2 Code Validation and Grid Independence Test

Code validation has been presented in Table 3.3 for the mixed convection flow. Code validation has also been performed for free convection results published in the literature, given in Table 3.4, for various computed variables and the results have an excellent agreement for both of the cases. Furthermore, the comparison of our results with those of Ghaffarpasand [121] has also been demonstrated by Figure 3.2. Grid independent solution for the problem is achieved through the grid refinement study and results for average Nusselt number have been given in Table 3.5 for $Re = 100, Ri = 10, \phi = 0.04, \psi = 15^\circ$ together with the number of elements #EL and the total number of all space degrees of freedom #DOFs which are needed to represent the discrete velocity/temperature and pressure solution with respect to the used discretization. A uniform grid at level $\ell = 9$ with $\#EL = 65536$ is utilized for all the simulations in this chapter.

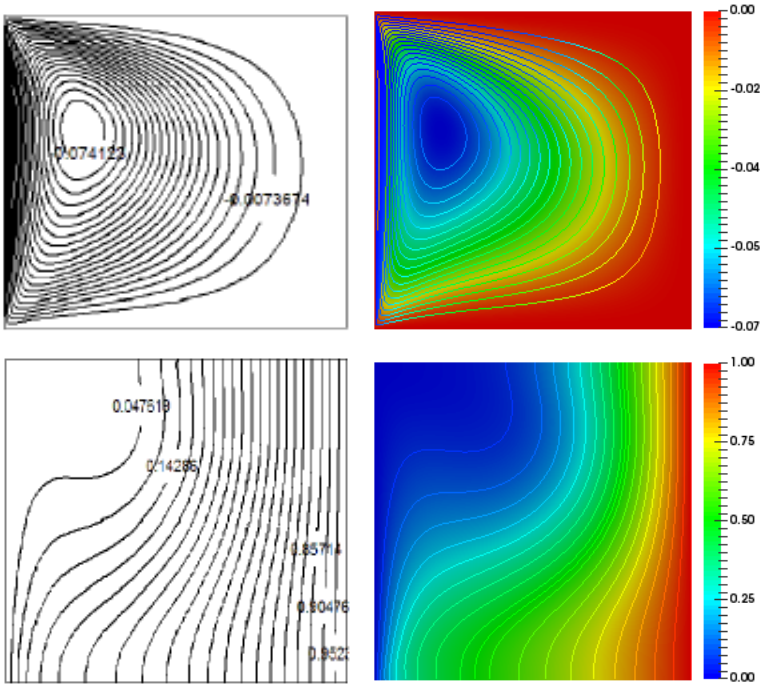

Figure 3.2: Code validation of streamlines (above row) and isotherms (bottom row) contours of present study (right column) to that of Ghaffarpasand [121] (left column).

Re		100	400	1000
Nu_{avg}	Present study	2.03	4.07	6.58
	Malleswaran and Sivasankaran [122]	–	4.08	6.48
	Sheremet and Pop [123]	2.05	4.09	6.70
	Saha *et al.* [124]	2.01	3.97	6.28
	Abu-Nada and Chamkha [125]	2.09	4.16	6.55
	Sharif [126]	–	4.05	6.55
	Iwatsu *et al.* [127]	1.94	3.84	6.33

Table 3.3: Comparison of the present results with those of [122–127].

Rayleigh number		10^3	10^4	10^5	10^6
U_{max}	Present work	3.649	16.179	34.707	64.823
	Moumni [128]	3.650	16.178	34.764	64.835
	Kuzink *et al.* [129]	3.636	16.167	34.962	64.133
	Dixit and Babu. [130]	3.652	16.163	35.521	64.186
	De vahil Davis. [131]	3.649	16.178	34.730	64.630
	Djebail *et al.* [132]	3.634	16.134	34.662	64.511
	Markatos and Pericleous [133]	3.544	16.180	35.730	68.810
Y_{max}	Present work	0.810	0.820	0.850	0.850
	Moumni [128]	0.813	0.827	0.854	0.854
	Kuzink *et al.* [129]	0.809	0.821	0.854	0.860
	Dixit and Babu. [130]	0.812	0.828	0.855	0.849
	De vahil Davis. [131]	0.813	0.823	0.855	0.850
	Djebail *et al.* [132]	0.813	0.825	0.852	0.852
	Markatos and Pericleous [133]	0.832	0.832	0.857	0.872
Nu_{avg}	Present work	1.118	2.245	4.522	8.826
	Moumni [128]	1.117	2.244	4.521	8.824
	Kuzink *et al.* [129]	1.117	2.246	4.518	8.792
	Dixit and Babu. [130]	1.121	2.286	4.546	8.625
	De vahil Davis. [131]	1.118	2.243	4.519	8.800
	Djebail *et al.* [132]	1.115	2.226	4.508	8.713
	Markatos and Pericleous [133]	1.108	2.201	4.430	8.754

Table 3.4: Comparison of the present results with those of [128–133].

ℓ	#EL	#DOFs	$Nu_{\text{avg},S1}$	$Nu_{\text{avg},S2}$
4	64	496	1.13763	0.51621
5	256	1888	2.33642	1.27791
6	1024	7360	4.25657	3.54305
7	4096	29056	4.68552	4.04080
8	16384	115456	5.38090	4.62415
9	65536	460288	5.55777	4.78706
10	262144	1838080	5.56164	4.79133

Table 3.5: Results of grid independence test for Al_2O_3-water nanofluid.

3.4 Results and Discussion

We have considered a cavity saturated with alumina-water nanofluid along with two heat sources, both of the same length, located symmetrically from the side walls at the bottom. Figure 3.3 illustrates the impact of Re on the contours of streamlines and isotherms for nanofluid saturated with alumina nanoparticles in a square cavity with $Ri = 10$, $\psi = 15°$ and $\phi = 0.04$. It can be observed that for low Re, the flow is symmetric in the whole cavity. Enhancement in Reynolds number more than 10 causes the shear forces to increase due to moving walls that creates a disturbance in symmetry. Moreover, the eddies become increasingly large and are pushed down to the area near side vertical moving walls. One can observe from isotherm plots that at $Re = 1$, the contours are uniformly distributed and parallel to the two heat sources pointing that conduction is the dominant procedure for transfer of heat in the cavity. Increasing the Re causes strong thermal plumes to be formed that move to the side walls and tilt to the left heat source indicating dominant convection of heat in the cavity.

In Figure 3.4, impact of Ri on streamlines and isotherms with $Re = 100$, $\gamma = 15°$ and $\phi = 0.04$ is shown. For mixed convection case, i.e., $Ri = 1$ symmetric counter rotating vortices are observed indicating that buoyancy forces and shear forces

have equal effect on the flow in the cavity. Increasing the Ri more than 1 favors the natural convection case due to which the symmetry of counter rotating cells vanishes and strength of the buoyancy force increases which leads to the interaction of the shear and buoyancy forces at high Reynolds numbers, i.e., $Re = 100$. As one increases the Richardson number, the strength of streamlines also grows that is evident from the scale affixed to the right side of each figure. Moreover, with a rise in Richardson number, the isotherms are slightly pushed down towards the bottom tilting to left side wall due to inclination indicating more heat transfer because of left heat source.

Figure 3.5 represents impact of nanoparticles volume fraction on isotherms and streamlines with $Re = 100, Ri = 10$ and $\gamma = 15°$. As long as the streamlines are concerned, two counter-rotating vortices of same magnitude can be observed in the cavity. Moreover, addition of nanoparticles to base fluid reduces the strength of flow field due to density augmentation. Increasing in solid volume fraction causes a decrease in the intensity of buoyancy and, hence, the flow intensity. Thus, the fluid moves slower in the cavity in the presence of nanoparticles. Isotherm plots show a thermal plume in the middle of the cavity for $\phi = 0.01$. Augmenting the nanoparticles volume fraction, thickness of this plume starts increasing and becomes maximum for $\phi = 0.04$ that indicates a growth in heat transfer in the cavity.

Effect of inclination angle γ on streamlines and isotherms with $Ri = 10$, $Re = 100$ and $\phi = 0.04$ is depicted in Figure 3.6. For $\gamma = 0°$ symmetric counter rotating vortices of equal magnitudes are formed. Augmentation in inclination angle γ disturbs the symmetry of the vortices. Hence, larger and stronger vortices are formed in the left side of the cavity. As long as isotherms are concerned, for $\gamma = 0°$ a main vertical thermal plume in the middle of the cavity is noticed. Increasing γ main vertical thermal plume thickens and tilts to the left side of the cavity.

Variation of average entropy generation due to heat transfer, fluid friction, average temperature and kinetic energy with respect to inclination of cavity for pure

fluid ($\phi = 0$) and nanofluid ($\phi = 0.04$) have been depicted in Figures 3.7-3.14. It has been noticed that presence of nanoparticles has significant effect on the physical properties of fluid. For both of the cases of pure fluid and nanofluid, entropy generation due to heat transfer S_{HT}, entropy generation due to fluid friction S_{FF}, average temperature and kinetic energy diminish with increasing inclination angle γ but for the case of nanofluid, increase in scale of these properties has been observed.

Effect of cavity inclination angles on average Nusselt number of left heat source and right heat source has been demonstrated in Figures 3.15 and 3.16. It is noticed that average Nusselt number of both the heat sources is same with no cavity inclination. As the cavity inclination angle is increased from 15° to 45°, average Nusselt number due to left heat source increases while gradual reduction has been observed due to right heat source. Enhancement in Nusselt number because of the left heat source is due to density variation of the nanofluid.

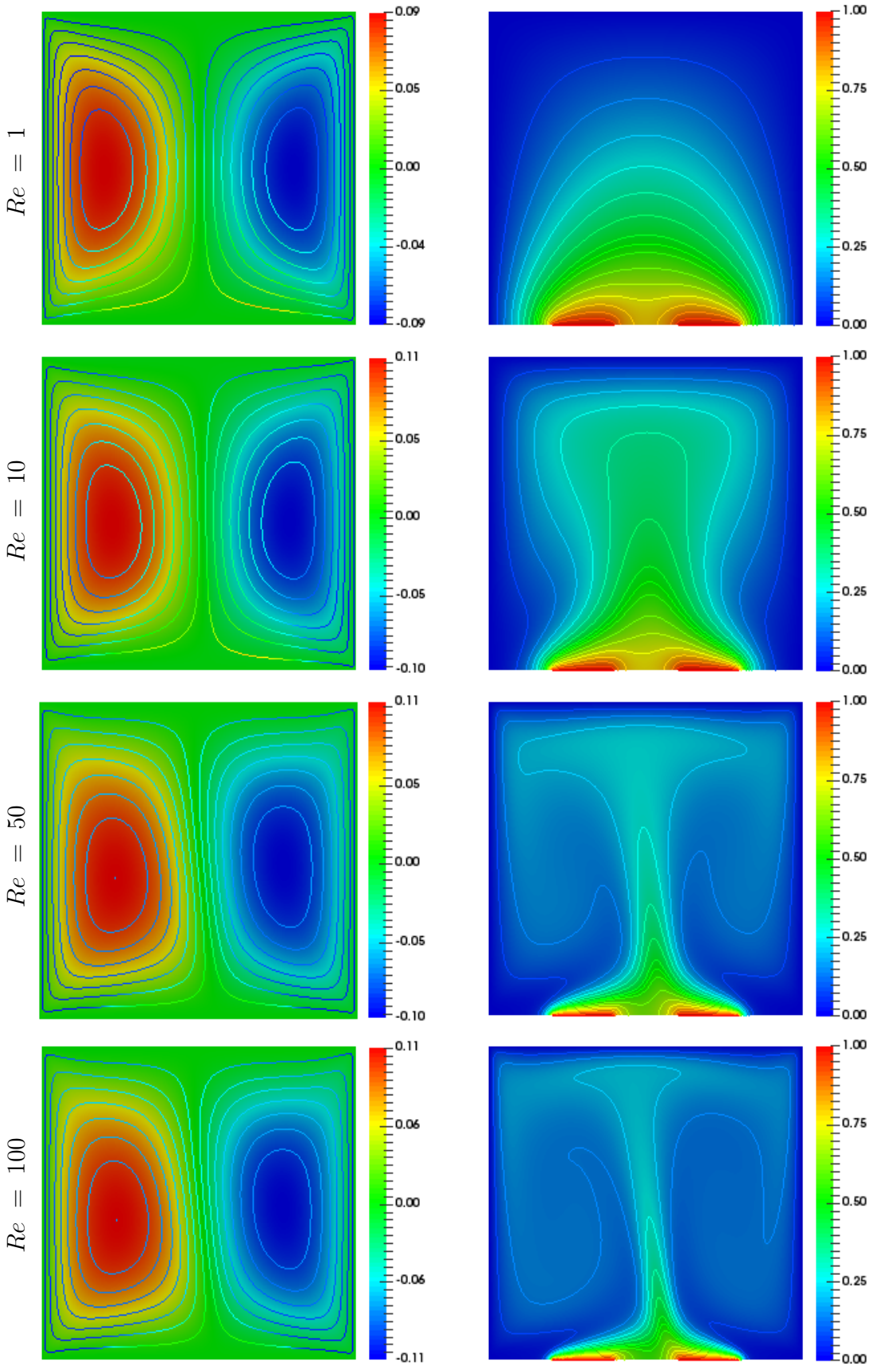

Figure 3.3: Streamlines and isotherms contours for different Re.

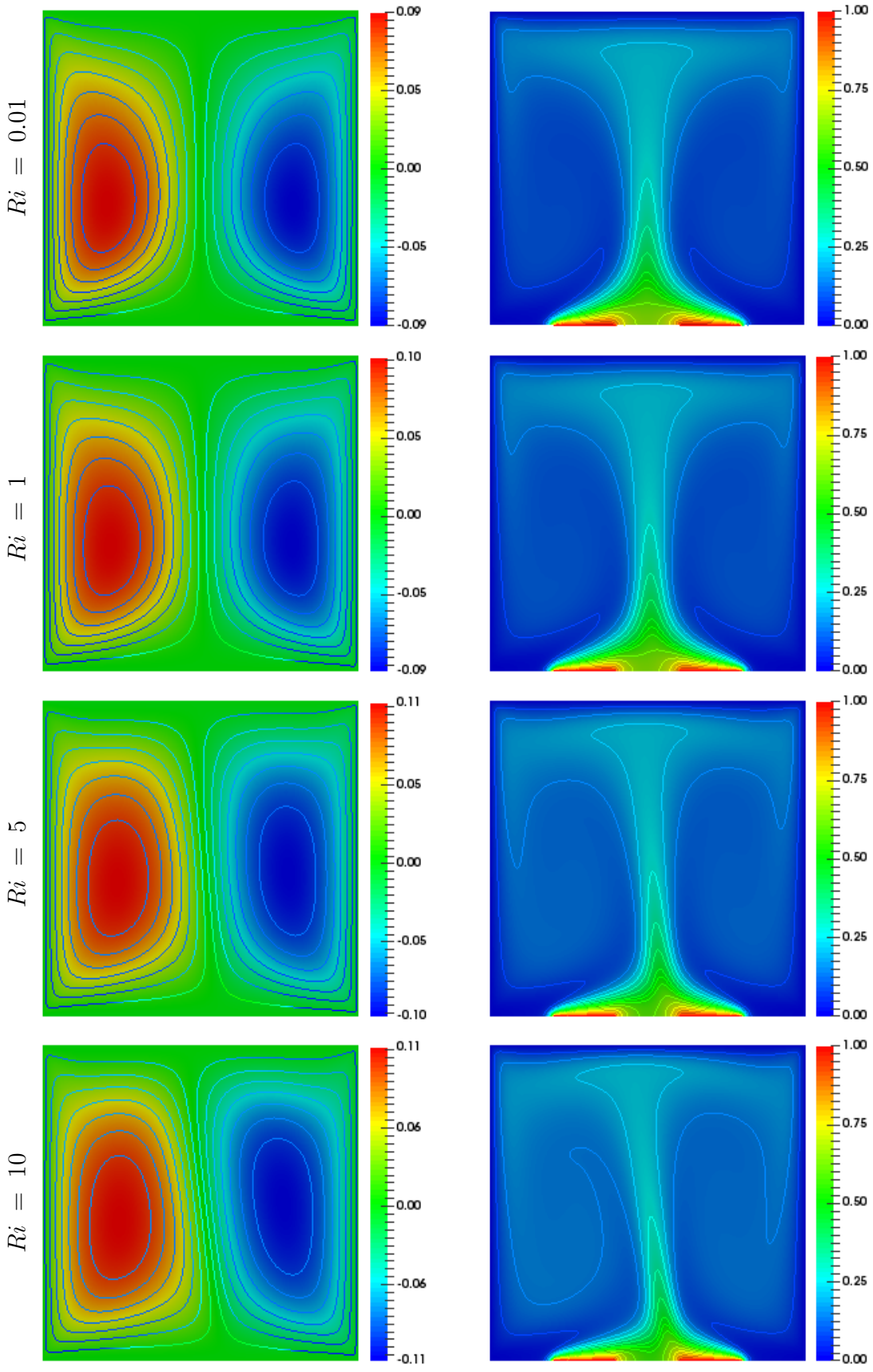

Figure 3.4: Streamlines and isotherms contours for different Ri.

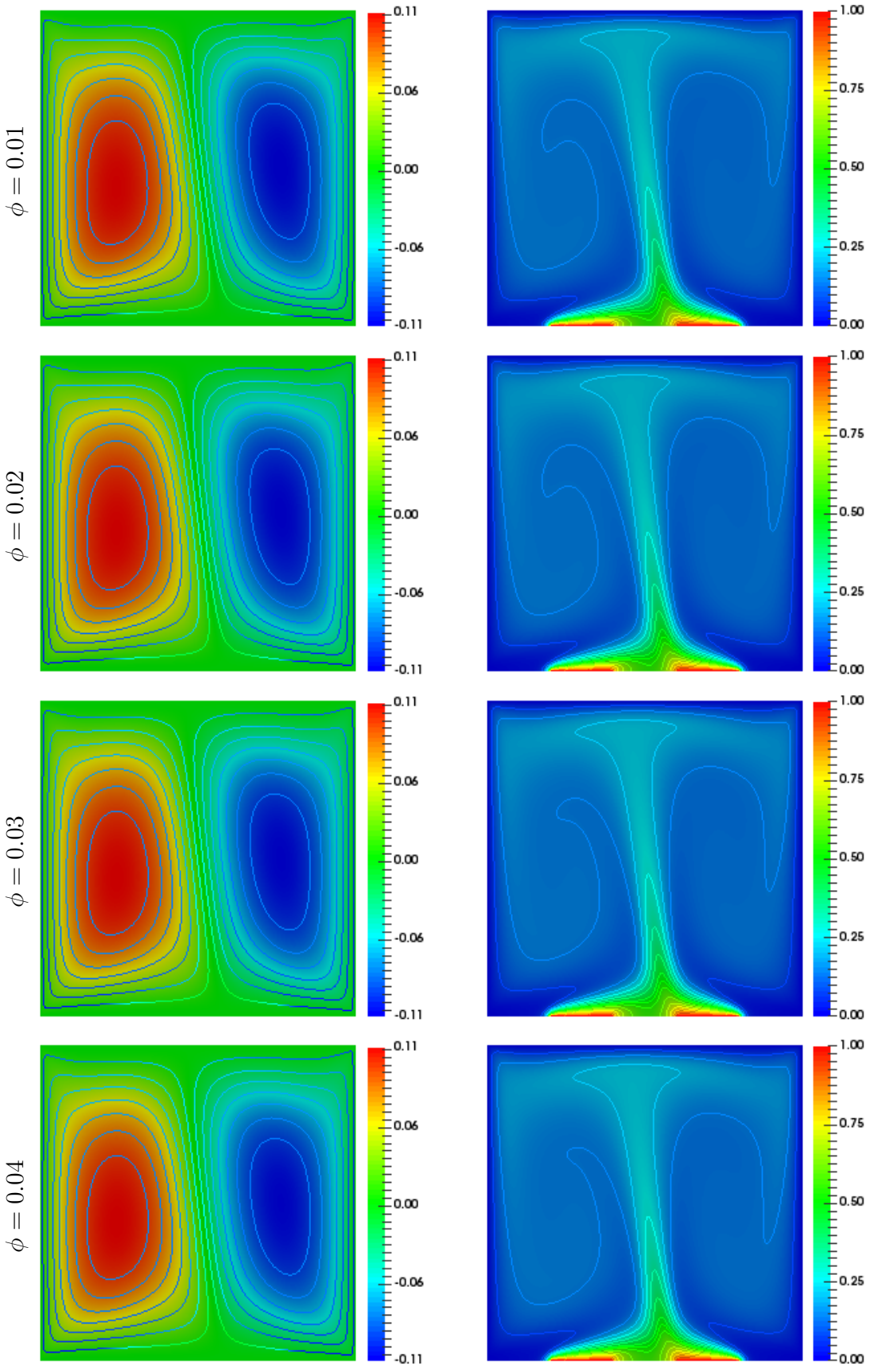

Figure 3.5: Streamlines and isotherms contours for different ϕ.

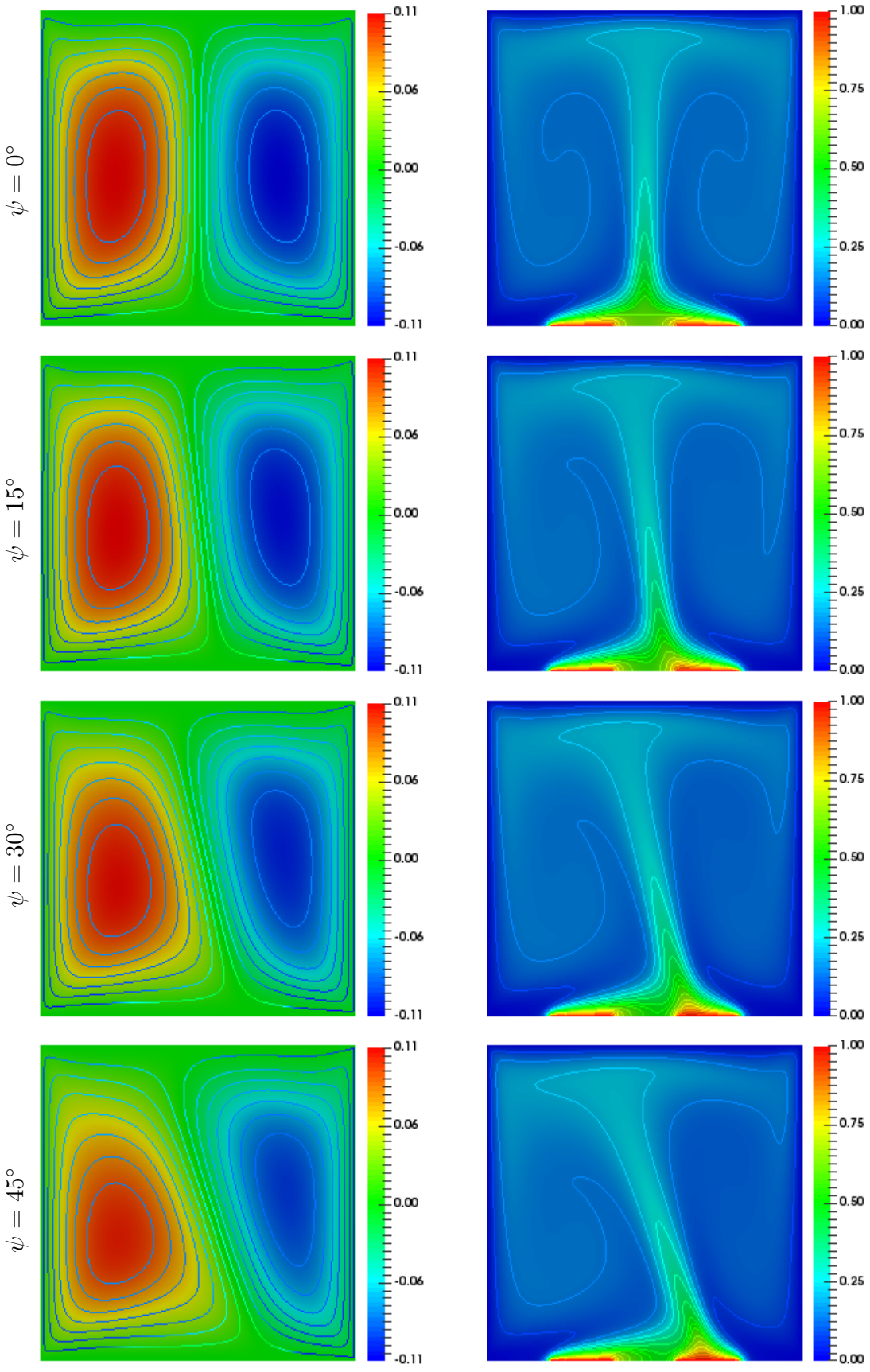

Figure 3.6: Streamlines and isotherms contours for different ψ.

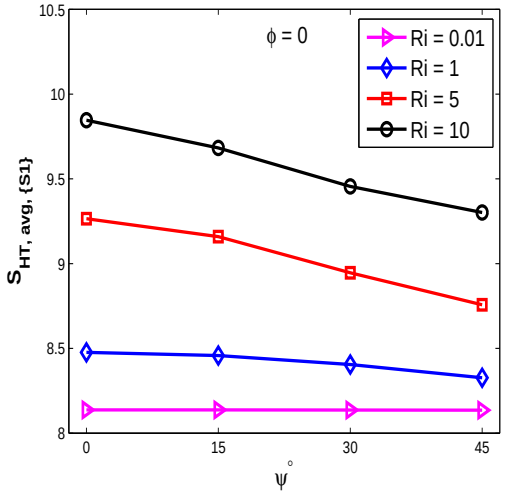

Figure 3.7: Variation of average entropy generation due to heat transfer as a function of ψ.

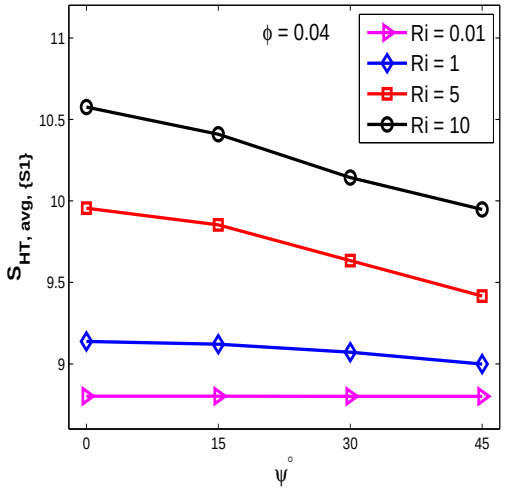

Figure 3.8: Variation of average entropy generation due to heat transfer as a function of ψ.

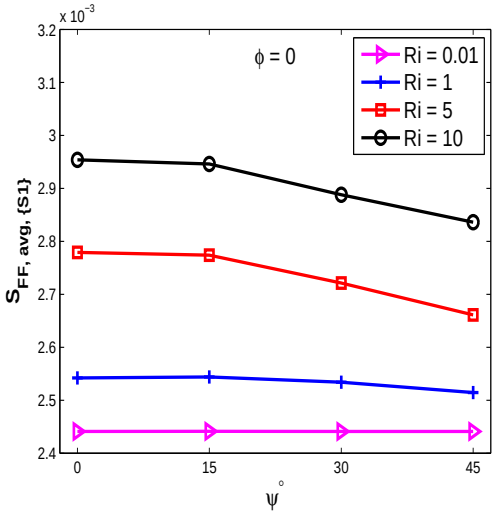

Figure 3.9: Variation of average entropy generation due to fluid friction as a function of ψ.

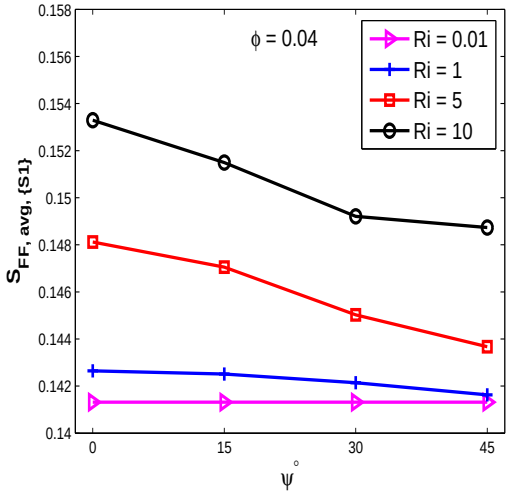

Figure 3.10: Variation of average entropy generation due to fluid friction as a function of ψ.

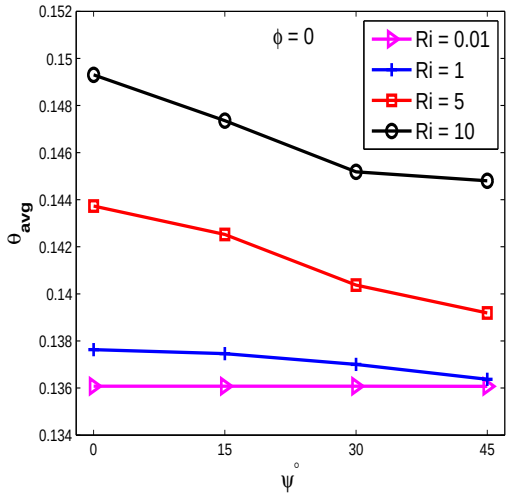

Figure 3.11: Variation of average temperature as a function of ψ.

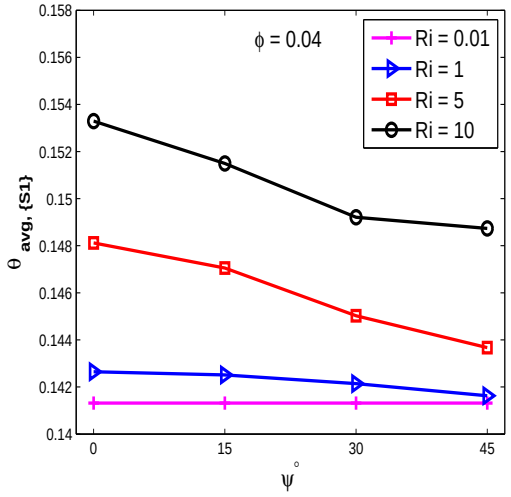

Figure 3.12: Variation of average temperature as a function of ψ.

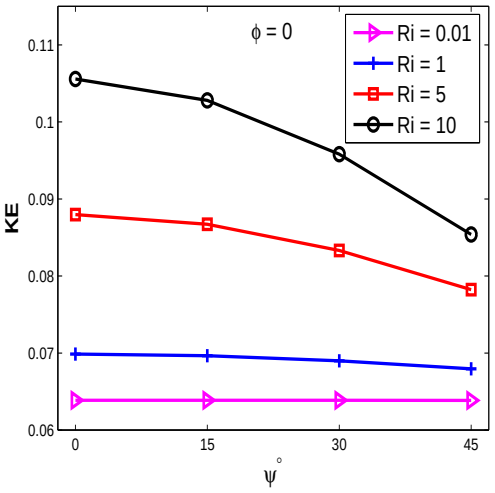

Figure 3.13: Variation of kinetic energy as a function of ψ.

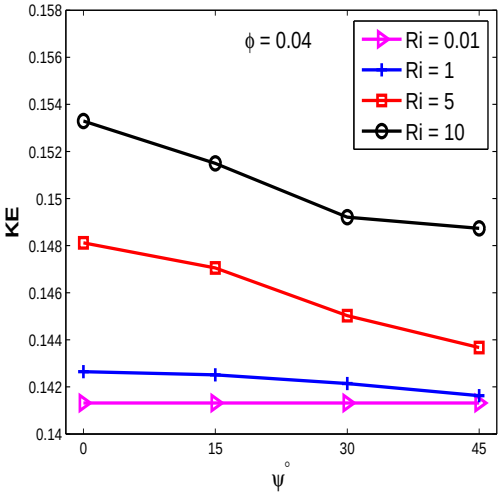

Figure 3.14: Variation of kinetic energy as a function of ψ.

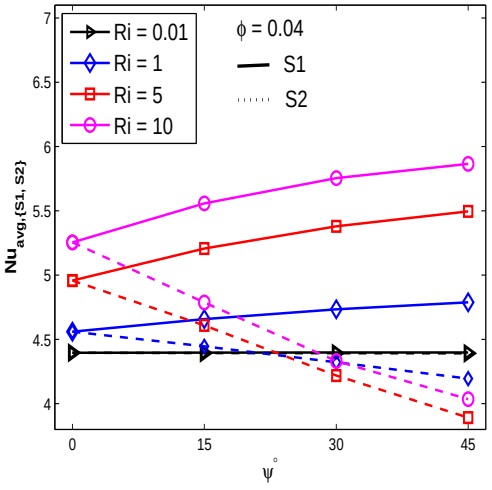

Figure 3.15: Effect of Richardson number on average Nusselt number of left heat source $S1$ and right heat source $S2$ as a function of ψ.

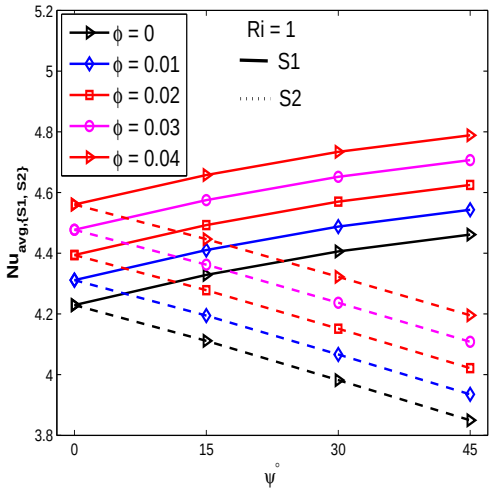

Figure 3.16: Effect of nanoparticle volume fraction on average Nusselt number of left heat source $S1$ and right heat source $S2$ as a function of ψ.

3.5 Closing Remarks

We have numerically investigated the heat transfer of Al_2O_3-water nanofluids in two dimensional mixed convection flows in a partially heated two-sided lid driven cavity. At the lower wall of the cavity, two heat sources are fixed and vertically moving walls and top wall are kept cool at constant temperature. Buoyancy force along with two moving vertical walls is responsible for the flow. First, problem is formulated and then solved by the Galerkin finite element method. In this method, we have used the nonconforming Stokes element $\widetilde{Q}_1/Q_0$, where $\widetilde{Q}_1$ element is for the velocity and temperature and Q_0 element for pressure. Effects of pertinent parameters such as Re, Ri, ϕ and ψ on the flow are investigated and findings are exactly of the same order as those of the previously performed analysis. This study can be concluded as follows.

1. An augmentation in the nanoparticles volume fraction and Richardson number causes a significant increase in the heat transfer.

2. An increase in the inclination angle diminishes the entropy generation due to the heat transfer S_{HT}, fluid friction S_{FF}, average temperature and kinetic energy.

3. An increase in the Richardson number Ri causes an enhancement in the entropy generation and kinetic energy.

4. An increase in the inclination angle causes to increase the average Nusselt number due to the left heat source while an opposite behavior has been observed for the right heat source.

Chapter 4

MHD Mixed Convective Nanofluid Flow with Entropy Generation

4.1 Introduction

In this chapter, the mixed convective Al_2O_3-water nanofluid flow in a partially heated square double lid driven cavity along with the entropy generation under the influence of inclined magnetic field is numerically investigated. Two heat sources are affixed at some portion of the bottom wall of the cavity while the remaining part of this wall is considered as an adiabatic. The moving vertical walls and the top wall are kept at constant cold temperature. Buoyant force is responsible for the flow along with the two moving vertical walls. The governing equations are discretized in space using the LBB-stable finite element pair $\mathrm{Q}_2/\mathrm{P}_1^{\mathrm{disc}}$ which leads to 3rd and 2nd order accuracy in the L_2-norm for the velocity/temperature and pressure, respectively and the fully implicit Crank-Nicolson scheme of 2nd order accuracy is utilized for the temporal discretization. Newton method is utilized to linearize the system of nonlinear equations and associated linear system is solved by the Gaussian elimination method in each time

level. Numerical results are presented and analyzed by means of the streamlines, isotherms, tables and some useful plots. The impacts of emerging parameters on the flow, in specific ranges such as Reynolds number ($1 \leq Re \leq 100$), Richardson number ($1 \leq Ri \leq 50$), Hartman number ($0 \leq Ha \leq 100$), solid volume fraction ($0 \leq \phi \leq 0.2$) as well as the angles of inclined magnetic field ($0° \leq \gamma \leq 90°$) are investigated and the findings are found to be exactly of the same order as those of the previously performed analysis. Calculation of the average Nusselt number, the average entropy generation due to heat transfer, fluid friction and magnetic field, total entropy generation, Bejan number and kinetic energy are the main focus of study in the present chapter. This study is organised in the following way. Section 4.2 illustrates the problem configuration. Section 4.3 contains information about space and time discretizations of the governing equations, the numerical method, code validation and grid independence test. Results based on the numerical simulation have been elaborated in Section 4.4. Finally, the conclusion has been drawn in Section 4.5.

4.2 Problem Formulation

4.2.1 The Problem Configuration

We consider a lid driven square cavity filled with nanofluid and two heat sources along the wall at the bottom at constant temperature (see Figure 4.1). The width of the cavity has been denoted by L, while T_h is the prescribed constant hot temperature, T_c is the constant cold temperature of the walls and ceiling and $e_{S1} = e_{S2} = L/5$ is the dimensional length of the heat sources. The distance of the sources from both of the side walls is exactly the same. Insulation is provided to those parts of the bottom that are not active. Cavity is saturated with Al_2O_3-water nanofluid. It is also assumed that the slipping effect between any two phases is negligible. The Joule heating and viscous dissipation are assumed to be neglected. Furthermore, the induced magnetic field is assumed to be negligible as compared with the external magnetic field [93, 96]. Nanofluid used

during this study has certain thermo-physical properties [38] that are tabulated in the Table 4.1. Density variation is taken into consideration by using the Boussinesq approximation which is apparent as the buoyancy force.

Physical Properties	Water	Alumina
$\rho\,(Kgm^{-3})$	997.1	3970
$C_p\,(JKg^{-1}K^{-1})$	4179	765
$k\,(Wm^{-1}K^{-1})$	0.613	40
$\beta\,(K^{-1})$	21×10^{-5}	0.85×10^{-5}
$\sigma\,(\Omega m)^{-1}$	0.05	1×10^{-10}

Table 4.1: Thermo-physical properties of water and alumina

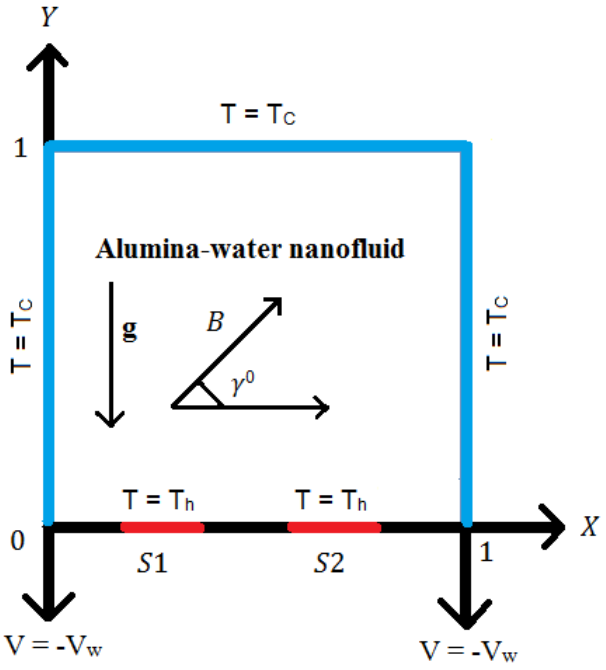

Figure 4.1: Schematic diagram of the physical model.

4.2.2 The Governing Equations

Governing equations of continuity, momentum and energy [37] under the above-mentioned assumptions are written as follows

$$\frac{\partial u}{\partial t} + u\frac{\partial u}{\partial x} + v\frac{\partial u}{\partial y} = -\frac{1}{\rho_{nf}}\frac{\partial p}{\partial x} + \frac{\mu_{nf}}{\rho_{nf}}\left(\frac{\partial^2 u}{\partial x^2} + \frac{\partial^2 u}{\partial y^2}\right) + \frac{\sigma_{nf}B_0^2}{\rho_{nf}}\left(v\sin\gamma\cos\gamma - u\sin^2\gamma\right), \tag{4.1}$$

$$\frac{\partial v}{\partial t} + u\frac{\partial v}{\partial x} + v\frac{\partial v}{\partial y} = -\frac{1}{\rho_{nf}}\frac{\partial p}{\partial y} + \frac{\mu_{nf}}{\rho_{nf}}\left(\frac{\partial^2 v}{\partial x^2} + \frac{\partial^2 v}{\partial y^2}\right) + \frac{(\rho\beta)_{nf}}{\rho_{nf}}g(T - T_c) + \frac{\sigma_{nf}B_0^2}{\rho_{nf}}\left(u\sin\gamma\cos\gamma - v\cos^2\gamma\right), \quad (4.2)$$

$$\frac{\partial u}{\partial x} + \frac{\partial v}{\partial y} = 0, \quad (4.3)$$

$$\frac{\partial T}{\partial t} + u\frac{\partial T}{\partial x} + v\frac{\partial T}{\partial y} = \alpha_{nf}\left(\frac{\partial^2 T}{\partial x^2} + \frac{\partial^2 T}{\partial y^2}\right). \quad (4.4)$$

4.2.3 The Dimensionless Governing Equations

Problem variables implemented regarding the non-dimensional form are as follows.

$$X = \frac{x}{L},\ Y = \frac{y}{L},\ U = \frac{u}{V_w},\ V = \frac{v}{V_w},\ \theta = \frac{T - T_c}{T_h - T_c},\ P = \frac{p}{\rho_{nf}V_w^2},\ \tau = \frac{tV_w}{L},$$
$$Re = \frac{V_w L}{\nu_f},\ Gr = \frac{g\beta\Delta T L^3}{\nu_f^2},\ Pr = \frac{\nu_f}{\alpha_f},\ Ha = B_0 L\sqrt{\frac{\sigma_f}{\mu_f}},\ S_T = s\frac{T_0^2 L^2}{k_f(T_h - T_c)^2}.$$

Dimensionless governing equations are reduced as follows

$$\frac{\partial U}{\partial \tau} + U\frac{\partial U}{\partial X} + V\frac{\partial U}{\partial Y} = -\frac{\partial P}{\partial X} + \frac{1}{Re}\frac{\rho_f}{\rho_{nf}}\frac{1}{(1-\phi)^{2.5}}\left(\frac{\partial^2 U}{\partial X^2} + \frac{\partial^2 U}{\partial Y^2}\right) + \frac{\rho_f}{\rho_{nf}}\frac{\sigma_{nf}}{\sigma_f}\frac{Ha^2}{Re}\left(V\sin\gamma\cos\gamma - U\sin^2\gamma\right), \quad (4.5)$$

$$\frac{\partial V}{\partial \tau} + U\frac{\partial V}{\partial X} + V\frac{\partial V}{\partial Y} = -\frac{\partial P}{\partial Y} + \frac{1}{Re}\frac{\rho_f}{\rho_{nf}}\frac{1}{(1-\phi)^{2.5}}\left(\frac{\partial^2 V}{\partial X^2} + \frac{\partial^2 V}{\partial Y^2}\right) + Ri\frac{\rho_f}{\rho_{nf}}\left(1 - \phi + \frac{\rho_s\beta_s}{\rho_f\beta_f}\phi\right)\theta + \frac{\rho_f}{\rho_{nf}}\frac{\sigma_{nf}}{\sigma_f}\frac{Ha^2}{Re}\left(U\sin\gamma\cos\gamma - V\cos^2\gamma\right), \quad (4.6)$$

$$\frac{\partial U}{\partial X} + \frac{\partial V}{\partial Y} = 0, \quad (4.7)$$

$$\frac{\partial \theta}{\partial \tau} + U\frac{\partial \theta}{\partial X} + V\frac{\partial \theta}{\partial Y} = \frac{\alpha_{nf}}{\alpha_f}\frac{1}{RePr}\left(\frac{\partial^2 \theta}{\partial X^2} + \frac{\partial^2 \theta}{\partial Y^2}\right). \quad (4.8)$$

Associated with the problem, the boundary conditions could be given as follows.

$U = 0, \quad V = -1, \quad \theta = 0, \quad$ for $\quad X = 0,\ 1 \quad$ and $0 \le Y \le 1$

$U = 0, \quad V = 0, \quad \theta = 0, \quad$ for $\quad 0 \le X \le 1 \quad$ and $Y = 1$

$$U = V = 0,\ \theta = 1 \ \text{ for } \begin{cases} 0.2 \le X \le 0.4, \\ 0.6 \le X \le 0.8 \quad \text{and } Y = 0, \end{cases}$$

$$U = V = 0,\ \frac{\partial \theta}{\partial Y} = 0 \ \text{ for } \begin{cases} 0 \le X \le 0.2, \\ 0.4 \le X \le 0.6 \ \text{ and } Y = 0 \\ 0.8 \le X \le 1 \end{cases}$$

4.2.4 The Effective Nanofluid Properties

The effective density, thermal diffusivity, electrical conductivity, specific heat and the coefficient of thermal expansion of the nanofluid [37, 134] are given as follows.

$$\rho_{nf} = (1-\phi)\rho_f + \phi\rho_p, \tag{4.9}$$

$$\alpha_{nf} = \frac{k_{nf}}{(\rho C_p)_{nf}}, \tag{4.10}$$

$$\sigma_{nf} = \sigma_f \left[1 + \frac{3\,(\sigma-1)\phi}{(\sigma+2)\ -(\sigma-1)\,\phi}\right],\ \sigma = \frac{\sigma_p}{\sigma_f} \tag{4.11}$$

$$(\rho C_p)_{nf} = (1-\phi)\,(\rho C_p)_f\ + \phi(\rho C_p)_p, \tag{4.12}$$

$$(\rho\beta)_{nf} = (1-\phi)(\rho\beta)_f + \phi(\rho\beta)_p. \tag{4.13}$$

The nanofluid thermal conductivity is computed by the following model [114].

$$\frac{k_{nf}}{k_f} = \frac{k_p + \ 2k_f - 2\phi\,(k_f - k_p)}{k_p + 2k_f\ + \phi\,(k_f - k_p)}, \tag{4.14}$$

where k_p and k_f are the thermal conductivities of dispersed nanoparticles and pure fluid accordingly. By the help of Brinkman model [120], the effective dynamic viscosity is calculated as follows:

$$\mu_{nf} = \frac{\mu_f}{(1-\phi)^{2.5}}. \tag{4.15}$$

4.2.5 The Entropy Generation

The entropy generation due to various physical sources can be written as follows:

$$s = \frac{k_{nf}}{T_0^2}\left[\left(\frac{\partial T}{\partial x}\right)^2 + \left(\frac{\partial T}{\partial y}\right)^2\right] + \frac{\mu_{nf}}{T_0}\left[2\left(\left(\frac{\partial u}{\partial x}\right)^2 + \left(\frac{\partial v}{\partial y}\right)^2\right) + \left(\frac{\partial u}{\partial y} + \frac{\partial v}{\partial x}\right)^2\right] + \frac{\sigma_{nf} B_0^2}{T_0}\left(u\sin\gamma - v\cos\gamma\right)^2, \tag{4.16}$$

where $T_0 = \frac{T_h + T_c}{2}$. The dimensionless entropy generation obtained from Eq. (4.16) is given as follows:

$$S_T = \frac{k_{nf}}{k_f}\left[\left(\frac{\partial \theta}{\partial X}\right)^2 + \left(\frac{\partial \theta}{\partial Y}\right)^2\right] + \chi\frac{\mu_{nf}}{\mu_f}\left[2\left(\left(\frac{\partial U}{\partial X}\right)^2 + \left(\frac{\partial V}{\partial Y}\right)^2\right)\right] + \chi\frac{\mu_{nf}}{\mu_f}\left[\left(\frac{\partial U}{\partial Y} + \frac{\partial V}{\partial X}\right)^2\right] + \chi Ha^2\frac{\sigma_{nf}}{\sigma_f}\left(U\sin\gamma - V\cos\gamma\right)^2, \tag{4.17}$$

where

$$S_T = S_{HT} + S_{FF} + S_{MF}, \tag{4.18}$$

$$S_{HT} = \frac{k_{nf}}{k_f}\left[\left(\frac{\partial \theta}{\partial X}\right)^2 + \left(\frac{\partial \theta}{\partial Y}\right)^2\right], \tag{4.19}$$

$$S_{FF} = \chi\frac{\mu_{nf}}{\mu_f}\left[2\left(\left(\frac{\partial U}{\partial X}\right)^2 + \left(\frac{\partial V}{\partial Y}\right)^2\right) + \left(\frac{\partial U}{\partial Y} + \frac{\partial V}{\partial X}\right)^2\right], \tag{4.20}$$

$$S_{MF} = \chi Ha^2\frac{\sigma_{nf}}{\sigma_f}\left(U\sin\gamma - V\cos\gamma\right)^2. \tag{4.21}$$

Here S_{HT}, S_{FF} and S_{MF} represent the non-dimensional entropy generation due to heat transfer, fluid friction and magnetic field, respectively. In Eq. (4.17), χ is the irreversibility factor. It is expressed as follows:

$$\chi = \frac{\mu_f T_0}{k_f}\left(\frac{V_w}{T_h - T_c}\right)^2. \tag{4.22}$$

Integrating the Eq. (4.17) yields the dimensionless average entropy generation S_{avg} that could be given as follows:

$$S_{\text{avg}} = \frac{1}{\vartheta}\int S_T d\vartheta = S_{HT,\text{avg}} + S_{FF,\text{avg}} + S_{MF,\text{avg}}. \tag{4.23}$$

Here, the total volume of the nanofluid is represented by ϑ. Moreover, $S_{HT,\text{avg}}$, $S_{FF,\text{avg}}$ and $S_{MF,\text{avg}}$ are respectively the dimensionless average entropy generation for heat transfer, fluid friction and magnetic field. An important dimensionless number regarding the entropy is the Bejan number that is defined as the ratio of entropy generation due to heat transfer to the total entropy generation which could be written as follows:

$$Be = \frac{S_{HT}}{S_T}.$$

The Richardson number $Ri = \frac{Gr}{Re^2}$ in the mixed convection is used to show the significance of the free convection related to the forced convection. It might be noticed that the free convection phenomena are studied for $Ri > 10$, mixed convection effects can be visualised for $Ri = 1$ and influence of forced convection can be observed for $Ri < 0.1$.

4.2.6 Calculation of the Nusselt number

To determine the heat transfer characteristics, we are interested to compute the local and the average Nusselt number on both of the discrete heat sources. Local Nusselt number on each of the heat sources could be given as follows.

$$Nu = \frac{h_{nf} L}{k_f}, \tag{4.24}$$

where h_{nf} is the heat transfer coefficient with

$$h_{nf} = \frac{q}{T_h - T_c}, \tag{4.25}$$

where q is the wall heat flux per unit area with

$$q = -k_{nf}\frac{(T_h - T_c)}{L}\frac{\partial\theta}{\partial Y}\bigg|_{Y=0}, \tag{4.26}$$

$$Nu = -\frac{k_{nf}}{kf}\left(\frac{\partial\theta}{\partial Y}\right), \tag{4.27}$$

$$Nu_{\text{avg},S1} = \int_{0.2}^{0.4} Nu\ dX \text{ and } Nu_{\text{avg},S2} = \int_{0.6}^{0.8} Nu\ dX. \tag{4.28}$$

4.3 The Numerical Approach

4.3.1 Spatial and Temporal Discretization

The system of coupled non-linear partial dierential equations together with given boundary conditions have been discretized numerically by the finite element formulation. The numerical procedure used to solve the governing equations for the present work is based on the Galerkin weighted residual method in which we have used the higher order Stokes element Q_2/P_1^{disc}, where Q_2 element is utilized for the velocity and temperature and P_1^{disc} element is used for the pressure (see 2.5 for detail). The variational or weak form of the governing Eqs. (4.5) - (4.8) is given in the following:

$$\begin{aligned}
&\int_\Omega \frac{\partial U}{\partial\tau}\ w\ d\Omega + \int_\Omega \left(U\frac{\partial U}{\partial X} + V\frac{\partial U}{\partial Y}\right) w\ d\Omega = -\int_\Omega \frac{\partial P}{\partial X}\ w\ d\Omega \\
&+ \frac{1}{Re}\frac{\rho_f}{\rho_{nf}}\frac{1}{(1-\phi)^{2.5}}\int_\Omega \left(\frac{\partial^2 U}{\partial X^2} + \frac{\partial^2 U}{\partial Y^2}\right) w\ d\Omega \\
&+ \frac{\rho_f}{\rho_{nf}}\frac{\sigma_{nf}}{\sigma_f}\frac{Ha^2}{Re}\left(\sin\gamma\cos\gamma\int_\Omega Vw\ d\Omega - \sin^2\gamma\int_\Omega Uw\ d\Omega\right), \\
&\int_\Omega \frac{\partial V}{\partial\tau}\ w\ d\Omega + \int_\Omega \left(U\frac{\partial V}{\partial X} + V\frac{\partial V}{\partial Y}\right) w\ d\Omega = -\int_\Omega \frac{\partial P}{\partial Y}\ w\ d\Omega \\
&+ \frac{1}{Re}\frac{\rho_f}{\rho_{nf}}\frac{1}{(1-\phi)^{2.5}}\int_\Omega \left(\frac{\partial^2 V}{\partial X^2} + \frac{\partial^2 V}{\partial Y^2}\right) w\ d\Omega \\
&+ Ri\frac{\rho_f}{\rho_{nf}}\left(1-\phi + \frac{\rho_s\beta_s}{\rho_f\beta_f}\phi\right)\int_\Omega \theta\ w\ d\Omega
\end{aligned} \tag{4.29}$$

$$+ \frac{\rho_f}{\rho_{nf}} \frac{\sigma_{nf}}{\sigma_f} \frac{Ha^2}{Re} \left(\sin\gamma \cos\gamma \int_\Omega Uw \; d\Omega - \cos^2\gamma \int_\Omega Vw \; d\Omega \right), \tag{4.30}$$

$$\int_\Omega \left(\frac{\partial U}{\partial X} + \frac{\partial V}{\partial Y} \right) q \; d\Omega = 0, \tag{4.31}$$

$$\int_\Omega \frac{\partial \theta}{\partial \tau} \, w \; d\Omega + \int_\Omega \left(U \frac{\partial \theta}{\partial X} + V \frac{\partial \theta}{\partial Y} \right) w \; d\Omega$$
$$= \frac{\alpha_{nf}}{\alpha_f} \frac{1}{RePr} \int_\Omega \left(\frac{\partial^2 \theta}{\partial X^2} + \frac{\partial^2 \theta}{\partial Y^2} \right) w \; d\Omega. \tag{4.32}$$

Now, the infinite dimensional trial spaces U, V, θ and P are approximated by U_h, V_h, θ_h and P_h, respectively. Moreover, the infinite dimensional test spaces W and Q are approximated by the finite dimensional test spaces W_h and Q_h, respectively, in such a way that

$$w_h \in W_h \subset H^1(\Omega) = \left\{ s : \Omega \to \mathbb{R} : \int_\Omega |s(x)|^2 dx < \infty, \int_\Omega |s'(x)|^2 dx < \infty \right\},$$
$$q_h \in Q_h \subset L_2(\Omega) = \left\{ g : \Omega \to \mathbb{R} : \int_\Omega |g(x)|^2 dx < \infty \right\}.$$

After the finite dimensional approximation the Eqs. (4.29) - (4.32) takes the form, given as follows:

$$\int_\Omega \frac{\partial U_h}{\partial \tau} \, w_h \; d\Omega + \int_\Omega \left(U_h \frac{\partial U_h}{\partial X} + V_h \frac{\partial U_h}{\partial Y} \right) w_h \; d\Omega = - \int_\Omega \frac{\partial P_h}{\partial X} \, w_h \; d\Omega$$
$$+ \frac{1}{Re} \frac{\rho_f}{\rho_{nf}} \frac{1}{(1-\phi)^{2.5}} \int_\Omega \left(\frac{\partial^2 U_h}{\partial X^2} + \frac{\partial^2 U_h}{\partial Y^2} \right) w_h \; d\Omega$$
$$+ \frac{\rho_f}{\rho_{nf}} \frac{\sigma_{nf}}{\sigma_f} \frac{Ha^2}{Re} \left(\sin\gamma \cos\gamma \int_\Omega V_h w_h \; d\Omega - \sin^2\gamma \int_\Omega U_h w_h \; d\Omega \right), \tag{4.33}$$

$$\int_\Omega \frac{\partial V_h}{\partial \tau} \, w_h \; d\Omega + \int_\Omega \left(U_h \frac{\partial V_h}{\partial X} + V_h \frac{\partial V_h}{\partial Y} \right) w_h \; d\Omega = - \int_\Omega \frac{\partial P_h}{\partial Y} \, w_h \; d\Omega$$
$$+ \frac{1}{Re} \frac{\rho_f}{\rho_{nf}} \frac{1}{(1-\phi)^{2.5}} \int_\Omega \left(\frac{\partial^2 V_h}{\partial X^2} + \frac{\partial^2 V_h}{\partial Y^2} \right) w_h \; d\Omega$$
$$+ Ri \frac{\rho_f}{\rho_{nf}} \left(1 - \phi + \frac{\rho_s \beta_s}{\rho_f \beta_f} \phi \right) \int_\Omega \theta_h \, w_h \; d\Omega$$
$$+ \frac{\rho_f}{\rho_{nf}} \frac{\sigma_{nf}}{\sigma_f} \frac{Ha^2}{Re} \left(\sin\gamma \cos\gamma \int_\Omega U_h w_h \; d\Omega - \cos^2\gamma \int_\Omega V_h w_h \; d\Omega \right), \tag{4.34}$$

$$\int_\Omega \left(\frac{\partial U_h}{\partial X} + \frac{\partial V_h}{\partial Y} \right) q_h \; d\Omega = 0, \tag{4.35}$$

$$\int_\Omega \frac{\partial \theta_h}{\partial \tau}\, w_h\, d\Omega + \int_\Omega \left(U_h \frac{\partial \theta_h}{\partial X} + V_h \frac{\partial \theta_h}{\partial Y} \right) w_h\, d\Omega = \frac{\alpha_{nf}}{\alpha_f} \frac{1}{RePr} \int_\Omega \left(\frac{\partial^2 \theta_h}{\partial X^2} + \frac{\partial^2 \theta_h}{\partial Y^2} \right) w_h\, d\Omega. \tag{4.36}$$

Using the FEM approximation $U_h(\tau, X, Y) = \sum_{j=1}^{N} U_j(\tau)\xi_j(X, Y)$, $V_h(\tau, X, Y) = \sum_{j=1}^{N} V_j(\tau)\xi_j(X, Y)$, $\theta_h(\tau, X, Y) = \sum_{j=1}^{N} \theta_j(\tau)\xi_j(X, Y)$ and $P_h(X, Y) = \sum_{j=1}^{K} P_j\eta_j(X, Y)$ are the trial functions. Similarly $w_h = \sum_{i=1}^{N} w_i\ \xi_i$ and $q_h = \sum_{i=1}^{K} q_i\ \eta_i$ are the test functions. By the Galerkin finite element model for a typical element Ω_e, the Eqs. (4.33) - (4.36) are transformed into the following system:

$$\int_{\Omega_e} \frac{\partial U_j}{\partial \tau}\xi_j\xi_i d\Omega_e + U_j \int_{\Omega_e} \left(\overline{U}\xi_i \frac{\partial \xi_j}{\partial X} + \overline{V}\xi_i \frac{\partial \xi_j}{\partial Y} \right) d\Omega_e = -P_j \int_{\Omega_e} \eta_j \frac{\partial \xi_i}{\partial X} d\Omega_e + \frac{1}{Re}\frac{\rho_f}{\rho_{nf}}\frac{1}{(1-\phi)^{2.5}} U_j \int_{\Omega_e} \left(\frac{\partial \xi_j}{\partial X}\frac{\partial \xi_i}{\partial X} + \frac{\partial \xi_j}{\partial Y}\frac{\partial \xi_i}{\partial Y} \right) d\Omega_e + \frac{\rho_f}{\rho_{nf}}\frac{\sigma_{nf}}{\sigma_f}\frac{Ha^2}{Re} \left(\sin\gamma\cos\gamma V_j \int_{\Omega_e} \xi_j\xi_i d\Omega_e - \sin^2\gamma U_j \int_{\Omega_e} \xi_j\xi_i d\Omega_e \right), \tag{4.37}$$

$$U_j \int_{\Omega_e} \frac{\partial \xi_j}{\partial X}\eta_i d\Omega_e + V_j \int_{\Omega_e} \frac{\partial \xi_j}{\partial Y}\eta_i d\Omega_e = 0, \tag{4.38}$$

$$\int_{\Omega_e} \frac{\partial V_j}{\partial \tau}\xi_j\xi_i d\Omega_e + V_j \int_{\Omega_e} \left(\overline{U}\xi_i \frac{\partial \xi_j}{\partial X} + \overline{V}\xi_i \frac{\partial \xi_j}{\partial Y} \right) d\Omega_e = -P_j \int_{\Omega_e} \eta_j \frac{\partial \xi_i}{\partial Y} d\Omega_e + \frac{1}{Re}\frac{\rho_f}{\rho_{nf}}\frac{1}{(1-\phi)^{2.5}} V_j \int_{\Omega_e} \left(\frac{\partial \xi_j}{\partial X}\frac{\partial \xi_i}{\partial X} + \frac{\partial \xi_j}{\partial Y}\frac{\partial \xi_i}{\partial Y} \right) d\Omega_e + Ri\frac{\rho_f}{\rho_{nf}} \left(1 - \phi + \frac{\rho_s\beta_s}{\rho_f\beta_f}\phi \right) \theta_j \int_{\Omega_e} \xi_j\xi_i d\Omega_e + \frac{\rho_f}{\rho_{nf}}\frac{\sigma_{nf}}{\sigma_f}\frac{Ha^2}{Re} \left(\sin\gamma\cos\gamma U_j \int_{\Omega_e} \xi_j\xi_i d\Omega_e - \sin^2\gamma V_j \int_{\Omega_e} \xi_j\xi_i d\Omega_e \right), \tag{4.39}$$

$$\int_{\Omega_e} \frac{\partial \theta_j}{\partial \tau}\xi_j\xi_i d\Omega_e + \theta_j \int_{\Omega_e} \left(\overline{U}\xi_i \frac{\partial \xi_j}{\partial X} + \overline{V}\xi_i \frac{\partial \xi_j}{\partial Y} \right) d\Omega_e = \frac{1}{RePr}\theta_j \int_{\Omega_e} \left(\frac{\partial \xi_j}{\partial X}\frac{\partial \xi_i}{\partial X} + \frac{\partial \xi_j}{\partial Y}\frac{\partial \xi_i}{\partial Y} \right) d\Omega_e. \tag{4.40}$$

The final system can be expressed in the following comprehensive form

$$[\mathbf{M^e}]\{\dot{\mathbf{u}}^\mathbf{e}\} + [\mathbf{K^e}][\mathbf{u^e}] = \{\mathbf{F^e}\}, \tag{4.41}$$

$$[\mathbf{M^e}]\{\dot{\mathbf{u}}^\mathbf{e}\} + \underbrace{\begin{bmatrix} [K_{ji}^{11}] & [K_{ji}^{12}] & [K_{ji}^{13}] & [K_{ji}^{14}] \\ [K_{ji}^{21}] & [K_{ji}^{22}] & [K_{ji}^{23}] & [K_{ji}^{24}] \\ [K_{ji}^{31}] & [K_{ji}^{32}] & [K_{ji}^{33}] & [K_{ji}^{34}] \\ [K_{ji}^{41}] & [K_{ji}^{42}] & [K_{ji}^{43}] & [K_{ji}^{44}] \end{bmatrix}}_{\mathbf{K^e}} \underbrace{\begin{bmatrix} \{\underline{U}\} \\ \{\underline{V}\} \\ \{\underline{P}\} \\ \{\underline{\theta}\} \end{bmatrix}}_{\mathbf{u^e}} = \underbrace{\begin{bmatrix} \{\underline{F^1}\} \\ \{\underline{F^2}\} \\ \{\underline{F^3}\} \\ \{\underline{F^4}\} \end{bmatrix}}_{\mathbf{F^e}}, \quad (4.42)$$

In the expression (4.43), $[\mathbf{M^e}]$ is the elemental block mass matrix in which all the block matrices are zero except $[M_{ji}^{11}] = [M_{ji}^{22}] = [M_{ji}^{44}] = M = \int_{\Omega_e} \xi_j \xi_i \, d\Omega_e$ where the variation of i and j depends on the choice of the basis function and the geometric element considered. Furthermore, $\{\dot{\mathbf{u}}^\mathbf{e}\}$, $\mathbf{K^e}$, $\mathbf{u^e}$ and $\mathbf{F^e}$ in the expression (4.42) are said to be the time derivative vector for the nodal unknowns, the stiffness block matrix, the block solution vector for the nodal unknowns and the right hand side block vector at an element level, respectively. For the sake of brevity, the boundary integral is also included in $\mathbf{F^e}$.

$$[\mathbf{M^e}] = \begin{bmatrix} [M_{ji}^{11}] & [M_{ji}^{12}] & [M_{ji}^{13}] & [M_{ji}^{14}] \\ [M_{ji}^{21}] & [M_{ji}^{22}] & [M_{ji}^{23}] & [M_{ji}^{24}] \\ [M_{ji}^{31}] & [M_{ji}^{32}] & [M_{ji}^{33}] & [M_{ji}^{34}] \\ [M_{ji}^{41}] & [M_{ji}^{42}] & [M_{ji}^{43}] & [M_{ji}^{44}] \end{bmatrix} \quad (4.43)$$

In stiffness block matrix,

$$\begin{aligned}
K_{ji}^{11} &= \frac{1}{Re}\frac{\rho_f}{\rho_{nf}}\frac{1}{(1-\phi)^{2.5}}\int_{\Omega_e}\left(\left(\frac{\partial\xi_j}{\partial X}\frac{\partial\xi_i}{\partial X}+\frac{\partial\xi_j}{\partial Y}\frac{\partial\xi_i}{\partial Y}\right)+\left(\overline{U}\xi_i\frac{\partial\xi_j}{\partial X}+\overline{V}\xi_i\frac{\partial\xi_j}{\partial Y}\right)\right)\,d\Omega_e \\
&\quad + \frac{\rho_f}{\rho_{nf}}\frac{\sigma_{nf}}{\sigma_f}\frac{Ha^2}{Re}\left(\sin^2\gamma\int_{\Omega_e}\xi_j\xi_i d\Omega_e\right), \\
K_{ji}^{12} &= -\frac{\rho_f}{\rho_{nf}}\frac{\sigma_{nf}}{\sigma_f}\frac{Ha^2}{Re}\left(\sin\gamma\cos\gamma\int_{\Omega_e}\xi_j\xi_i d\Omega_e\right), \\
K_{ji}^{21} &= -\frac{\rho_f}{\rho_{nf}}\frac{\sigma_{nf}}{\sigma_f}\frac{Ha^2}{Re}\left(\sin\gamma\cos\gamma\int_{\Omega_e}\xi_j\xi_i d\Omega_e\right), \\
K_{ji}^{22} &= \frac{1}{Re}\frac{\rho_f}{\rho_{nf}}\frac{1}{(1-\phi)^{2.5}}\int_{\Omega_e}\left(\left(\frac{\partial\xi_j}{\partial X}\frac{\partial\xi_i}{\partial X}+\frac{\partial\xi_j}{\partial Y}\frac{\partial\xi_i}{\partial Y}\right)+\left(\overline{U}\xi_i\frac{\partial\xi_j}{\partial X}+\overline{V}\xi_i\frac{\partial\xi_j}{\partial Y}\right)\right)\,d\Omega_e \\
&\quad + \frac{\rho_f}{\rho_{nf}}\frac{\sigma_{nf}}{\sigma_f}\frac{Ha^2}{Re}\left(\cos^2\gamma\int_{\Omega_e}\xi_j\xi_i d\Omega_e\right),
\end{aligned}$$

$$K_{ji}^{44} = \frac{\alpha_{nf}}{\alpha_f}\frac{1}{RePr}\int_{\Omega_e}\left(\frac{\partial\xi_j}{\partial X}\frac{\partial\xi_i}{\partial X}+\frac{\partial\xi_j}{\partial Y}\frac{\partial\xi_i}{\partial Y}\right)\,d\Omega_e+\int_{\Omega_e}\left(\overline{U}\xi_i\frac{\partial\xi_j}{\partial X}+\overline{V}\xi_i\frac{\partial\xi_j}{\partial Y}\right)\,d\Omega_e,$$

$$K_{ji}^{24} = -Ri\frac{\rho_f}{\rho_{nf}}\left(1-\phi+\frac{\rho_s\beta_s\phi}{\rho_f\beta_f}\right)\int_{\Omega_e}\xi_j\xi_i\,d\Omega_e,$$

$$K_{ji}^{13} = -\int_{\Omega_e}\eta_j\frac{\partial\xi_i}{\partial X}d\Omega_e,$$

$$K_{ji}^{23} = -\int_{\Omega_e}\eta_j\frac{\partial\xi_i}{\partial Y}d\Omega_e,$$

$$K_{ji}^{31} = \int_{\Omega_e}\frac{\partial\xi_j}{\partial X}\eta_i d\Omega_e,$$

$$K_{ji}^{32} = \int_{\Omega_e}\frac{\partial\xi_j}{\partial Y}\eta_i d\Omega_e,$$

$$K_{ji}^{14} = K_{ji}^{33} = K_{ji}^{34} = K_{ji}^{41} = K_{ji}^{42} = K_{ji}^{43} = 0,$$

$$\overline{U} = \sum_{j=1}^{N} U_j\xi_j, \overline{V} = \sum_{j=1}^{N} V_j\xi_j.$$

The above system (4.42) involves the nodal unknowns $\mathbf{u^e}$ and the time dependent terms $\{\dot{\mathbf{u}}^{\mathbf{e}}\}$. Time discretization of the nodal unknowns still remains to do. Time discretization has been performed by utilizing the Crank-Nicolson method (see 2.4 for detail). We have utilized Q_2/P_1^{disc} for space discretization (see 2.5 for detail). After discretization in the space and time, we obtain an algebraic system of nonlinear equations. Integration of each term of these equations is performed by Gaussian quadrature method. Then the implementation of the boundary conditions is carried out and the linear algebraic equations are obtained from nonlinear equations using the iterative Newton method. Some tolerance value is prescribed to see the optimized minimum difference of the current values of the variables to the previous iteration values by achieving the convergence of the solution of an iterative scheme. In other words, the adopted criterion to stop the iterative scheme could be given as follows.

$$\left|\frac{\Gamma^{n+1}-\Gamma^n}{\Gamma^{n+1}}\right| \leq 10^{-6}, \tag{4.44}$$

where U, V, P or θ are denoted by a general variable Γ. Superscript n represents the iteration number in the above expression. Finally, these linear equations are computed by the Gaussian elimination method in each time level.

4.3.2 Code Validation and Grid Independence Test

Code validation has been performed for free convection results published in the literature and given in Table 3.4 of chapter 3, for various computed variables. Code validation has also been presented in Table 3.3 for mixed convection flow in the section 3.3.2 of Chapter 3 and the results have an excellent agreement for both of the cases. Grid independent solution for the problem is achieved through the grid refinement study and results for average Nusselt number have been given in Table 4.2 for $Re = 100, Ri = 20, \phi = 0.2, Ha = 50, \gamma = 15°$. It is obvious that grid independence is attained with a grid of size 256×256 in X and Y directions. Therefore, all the following simulations are performed by this grid resolution. All the results are produced and presented on a grid of size 256×256.

ℓ	#EL	#DOFs	$Nu_{\text{avg},S1}$	$Nu_{\text{avg},S2}$
4	64	1059	1.46797	1.78793
5	256	4035	2.95710	3.59910
6	1024	15747	3.50279	4.31398
7	4096	62211	3.28871	4.13362
8	16384	247299	3.34808	4.20865
9	65536	986115	3.59976	4.49398
10	262144	3938307	3.66390	4.57513

Table 4.2: Result of grid independence test

γ	$Nu_{\text{avg},S1}$	$Nu_{\text{avg},S2}$
0°	5.9842	5.9842
15°	5.7885	6.0696
30°	5.5760	6.0097
45°	5.5492	5.9303
60°	5.6903	5.9481
75°	5.9020	6.0110
90°	6.0165	6.0165

Table 4.3: Effect of magnetic field inclination angle γ on Nusselt number

4.4 Results and Discussion

Mixed convection flow of Al_2O_3-water nanofluid in a square double lid-driven cavity with inclined magnetic field, discrete heating and entropy generation is numerically investigated. The numerical results are acquired for Reynolds number Re = 1, 10, 50, 100, Richardson numbers Ri = 1, 5, 10, 20, 50, nanoparticle volume fraction ϕ = 0, 0.05, 0.10, 0.15, 0.20, Hartman numbers Ha = 0, 50, 75, 100 and inclination angles of magnetic field γ ranging from 0° to 90° with a difference of 15°. The assumed Prandtl number of pure fluid is 6.2. Standard values of Re, Ri, ϕ, Ha and γ are taken as 100, 20, 0.2, 50 and 0°, respectively unless these are mentioned.

Impact of magnetic field inclination angle on average Nusselt number is portrayed in Table 4.3. It is observed that at γ=0°,90°, heat transfer due to left heater $S1$ and right heater $S2$ is same. Heat transfer decreases due to left heat source for γ ranging from 0° to 45° and then it enhances for $\gamma = 60° - 90°$. Similarly, transfer of heat declines due to right heat source for γ ranging from 15° to 45° and then it amplifies for $\gamma = 60° - 90°$. Infact, heat transfer reduces as magnetic field is applied close to the heat source and opposite behavior is shown when magnetic field occurs beyond the heat source.

Figure 4.2 shows the impact of Reynolds number $Re = 1, 10, 50, 100$ on isotherms and streamlines for cavity saturated with Al_2O_3-water nanofluid for $Ri = 20, \phi = 0.2, Ha = 50, \gamma = 0°$. It can be seen the symmetry of flow from the counter rotation of cells of same value for the given Re in the cavity. Augmenting the value of the Re, the swirls become larger and are propelled to the left and right verticle walls. Isotherms show that for small value of Re, the contours are equally distributed and symmetrical to the discrete heat sources. This indicates that conduction plays a governing role for the transfer of heat in cavity. Also, enhancement in Re causes to push the cold fluid to the bottom wall which results in the form of convective cooling. Thus a significant change can be observed in isotherms.

The influence of Ri on isotherms and streamlines is depicted in Figure 4.3. For $Ri = 1$, the streamlines are symmetrically distributed to the vertical midline in the cavity. Increasing the Ri, counter rotating cells are becoming larger and moving to cold vertical side walls due to increase in buoyancy forces. Moreover, increase in the Ri causes the isotherms to expand to the side moving vertical walls. This indicates the augmentation in the temperature gradients.

Effects of inclined magnetic field on the flow and thermal configuration for inclination angles $0°, 30°, 60°$ and $90°$ in the form of streamlines and isotherms are depicted in Figure 4.4. It is observed that for $\gamma = 0°$, streamlines are more clustered in the middle of the cavity with counter rotation of cells of same value. The isotherms, particularly in the central portion, i.e., away from the boundaries, exhibit appreciable effects of the convection currents. When inclination angle γ is increased from $30°$ to $60°$, isotherms are more affected as compared to the streamlines and they change significantly. The streamlines are being to distort from their original shape and the cluster of streamlines is shifted to right vertical wall and in isotherms the main vortex is tilted to the right vertical wall. Finally, for $\gamma = 90°$, in isotherms, a straight upward plume arises in the center of the cavity expanding to the side vertical moving walls. It indicates the maximum heat flow occurs in the center of the cavity.

Impact of nanoparticle volume fractions on streamlines and isotherms is illustrated by Figure 4.5. Enhancement in the rate of heat transfer from discrete heat sources by increasing the nanoparticle volume fraction at constant Re and Ri is noticed. The effect is more amplified on isotherms as compared to streamlines. It is worthy noted that the thickness of plumes, that rise from heat source in isotherms for $\phi = 0.2$, is more enhanced as compared to $\phi = 0.05$.

Effect of Reynolds number on Nusselt number, entropy generation and Bejan number with different nanoparticle volume fraction is shown in Figures 4.6-4.11.

It is observed that Nusselt number Nu, entropy generation due to heat transfer S_{HT}, entropy generation due to fluid friction S_{FF}, entropy generation due to magnetic field S_{MF}, total entropy generation S_T and Be increase with an increase in Re and ϕ. This increase in entropy generation is mostly due to heat transfer. Fluid friction and magnetic field play a little role for enhancement of entropy generation.

In Figures 4.12-4.17, effect of Richardson number Ri on Nusselt number, entropy generation and Bejan number with different magnetic field strength Ha is displayed. It is noticed that with an increase in Ri, the values of Nu and S_{HT} increase but for a fixed value of Ri and increasing the Ha, the values of Nu and S_{HT} decrease gradually. Entropy generation due to friction S_{FF} decreases with an increase in Ri but for a fixed value of Ri and increase in Ha result a gradual increase in S_{FF}. The value of S_{MF} increases with an increase in Ri and Ha. S_T increases with an increase in Ri while for a fixed value of Ri, total entropy generation S_T decreases with an increase in Ha. Be increases with an increase in Ri while for a fixed value of Ri, Bejan number Be gradually decrease with an increase in Ha.

Effect of Richardson number on Nusselt number, entropy generation and Bejan number with different nanoparticle volume fraction is shown in Figure 4.18-4.23. It is observed that Nusselt number Nu, entropy generation due to heat transfer S_{HT}, entropy generation due to fluid friction S_{FF}, entropy generation due to magnetic field S_{MF}, total entropy generation S_T and Be increase with an increase in Re and ϕ. It is commendable that increase in entropy generation is mostly due to heat transfer.

In Figure 4.24-4.29, effect of Reynolds number Re on Nusselt number, entropy generation and Bejan number with different magnetic field strength Ha is displayed. It is noticed that with an increase in Re, the values of Nu and S_{HT} also increase but for a fixed value of Re and increasing the Ha, the values of Nu and S_{HT} decrease gradually. Entropy generation due to friction S_{FF} increases with an

increase in Re and Ha. The value of S_{MF} increases with an increase in Re and Ha. S_T increases with an increase in Re while for a fixed value of Re, total entropy generation S_T decreases with an increase in Ha. Be increases with an increase in Re while for a fixed value of Re, Bejan number Be gradually decrease with an increase in Ha.

In Figure 4.30-4.33, effect of Reynolds number Re, Richardson number Ri, nanoparticle volume fraction ϕ and Hartman number Ha on kinetic energy is exhibited. One can observe that kinetic energy is enhanced with an increase in Re from 1 to 100 while for a fixed value of Re, it is decreased gradually with an increase in Ha from 0 to 100. For Richardson numbers ranging from 1 to 50, Kinetic energy is increasing gradually while for a fixed value of Ri, it decreases with an increase in Ha. If we observe the behavior of kinetic energy versus ϕ for various values of Re and Ri, we see that kinetic energy is enhanced for increasing values of Re, Ri and ϕ.

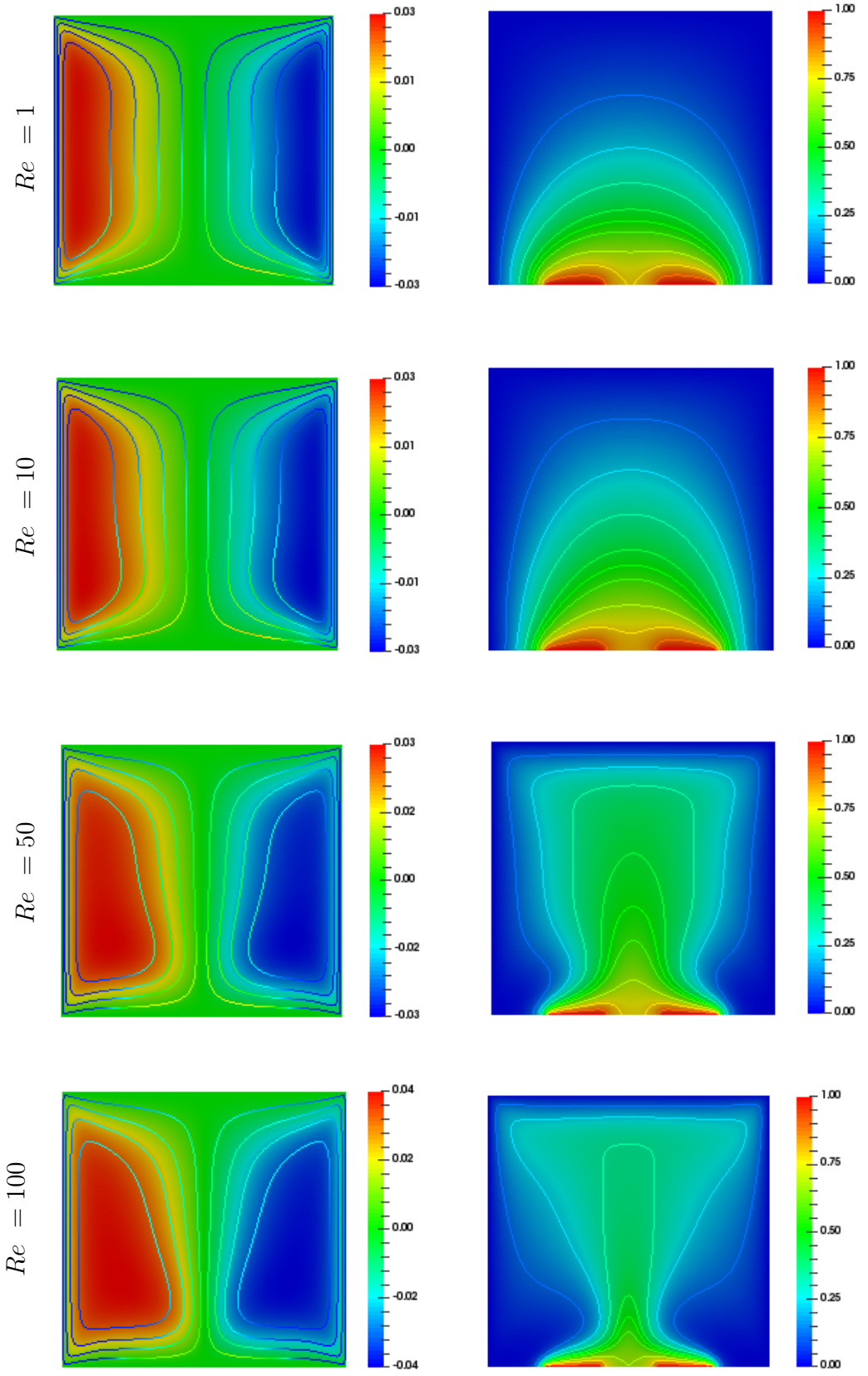

Figure 4.2: Streamlines and isotherms for different Re.

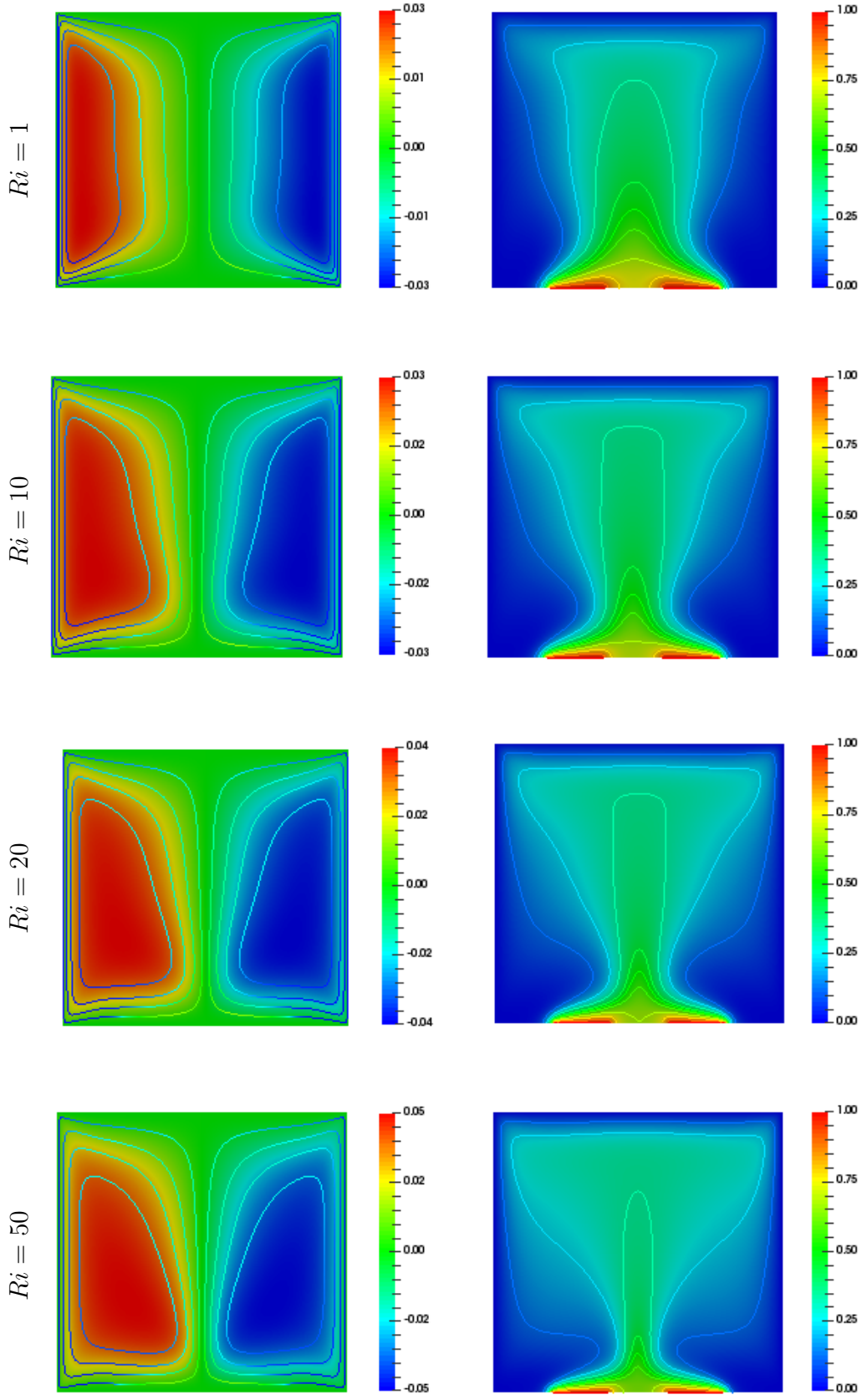

Figure 4.3: Streamlines and isotherms for different Ri.

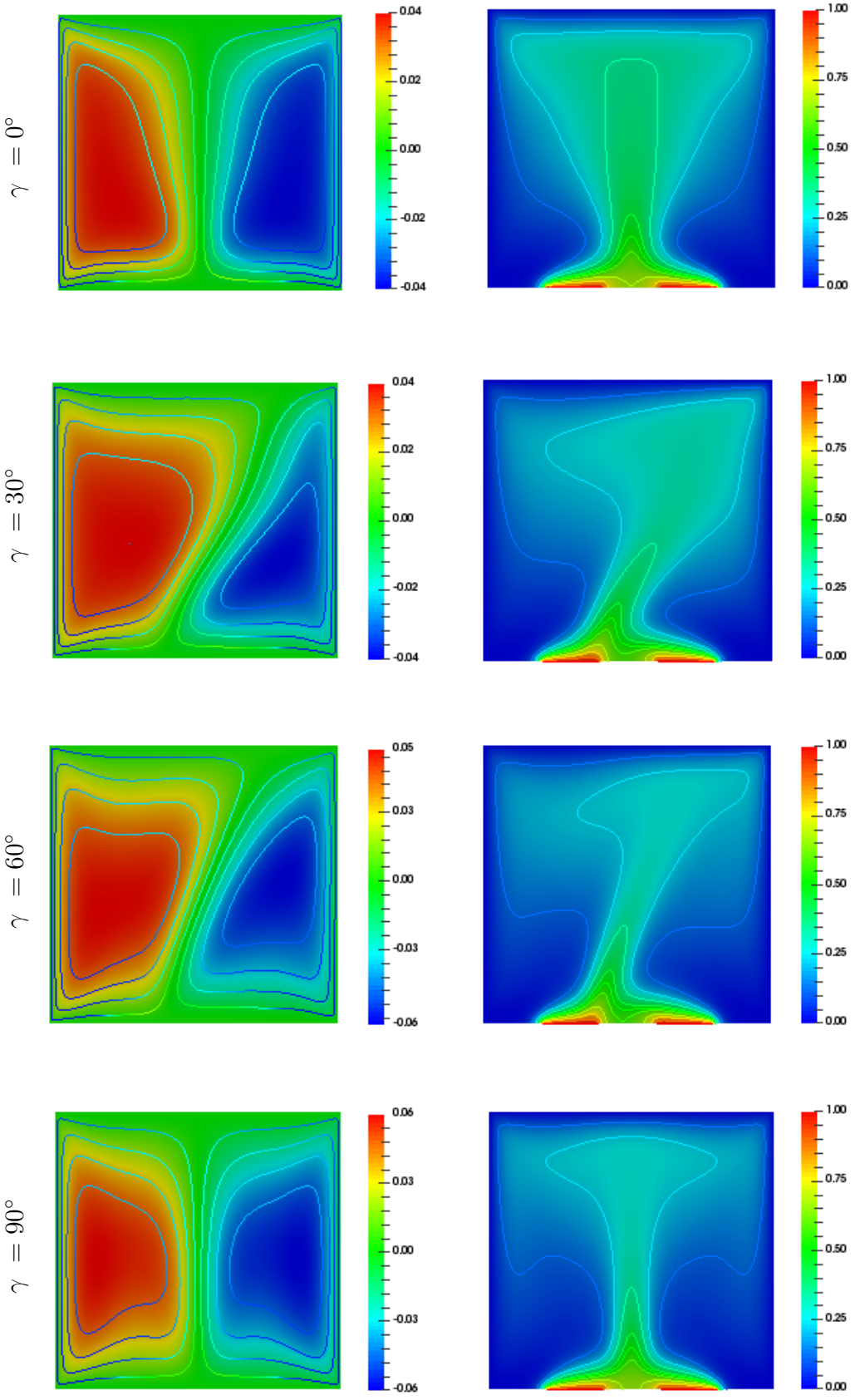

Figure 4.4: Streamlines and isotherms for different γ.

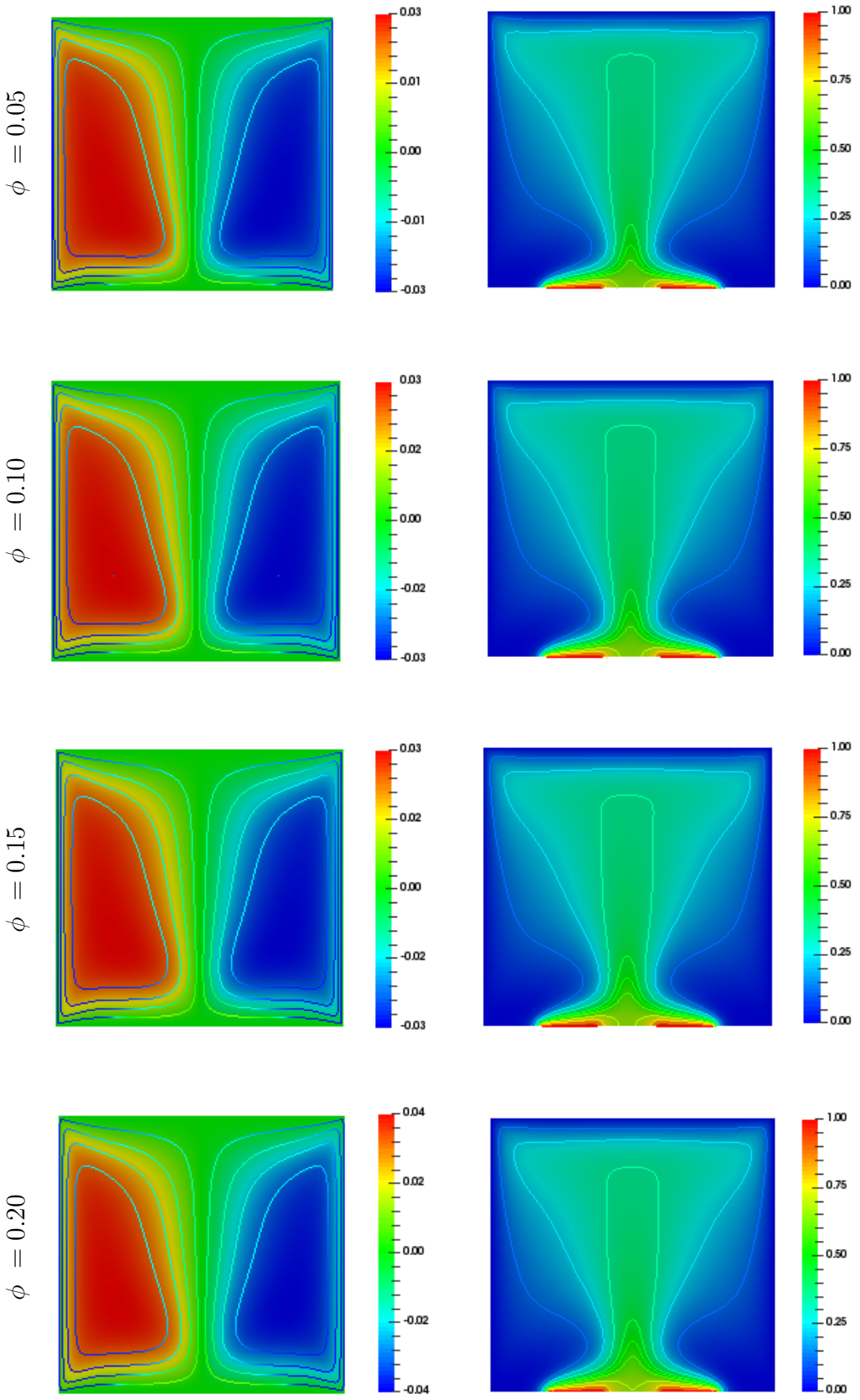

Figure 4.5: Streamlines and isotherms for different ϕ.

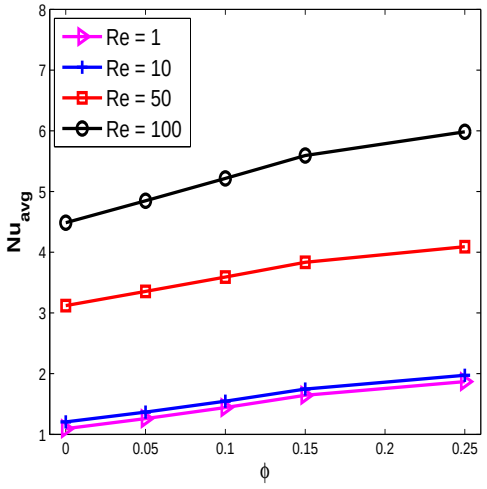

Figure 4.6: Effect of Reynolds number on average Nusselt number with different nanoparticle volume fraction.

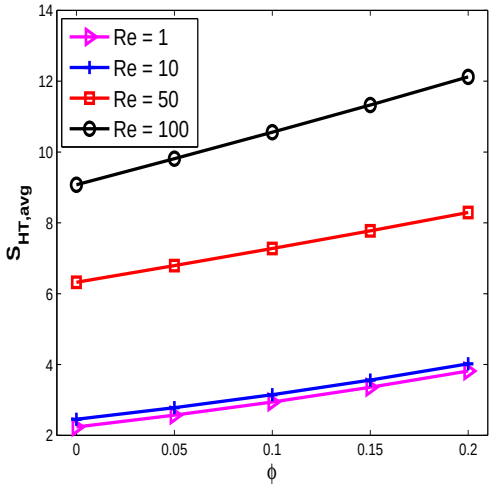

Figure 4.7: Effect of Reynolds number on entropy generation due to heat transfer with different nanoparticle volume fraction.

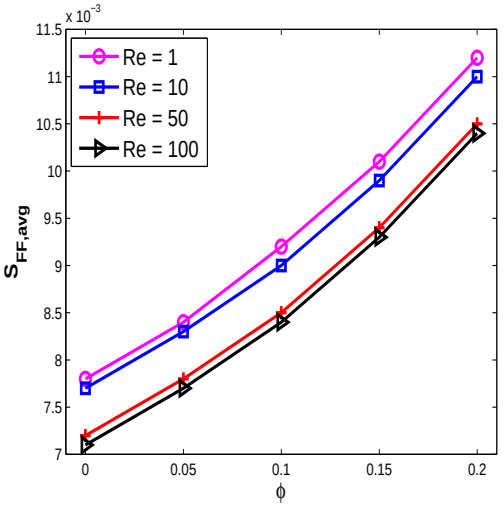

Figure 4.8: Effect of Reynolds number on entropy generation due to fluid friction with different nanoparticle volume fraction.

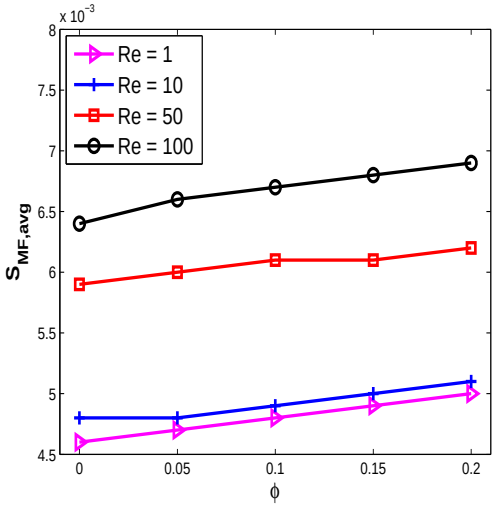

Figure 4.9: Effect of Reynolds number on entropy generation due to magnetic field with different nanoparticle volume fraction.

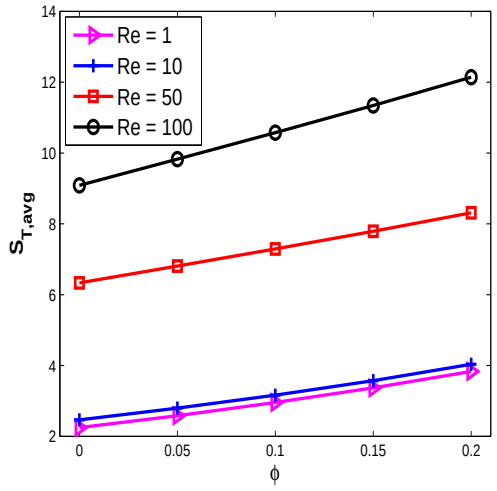

Figure 4.10: Effect of Reynolds number on total entropy generation due to magnetic field with different nanoparticle volume fraction.

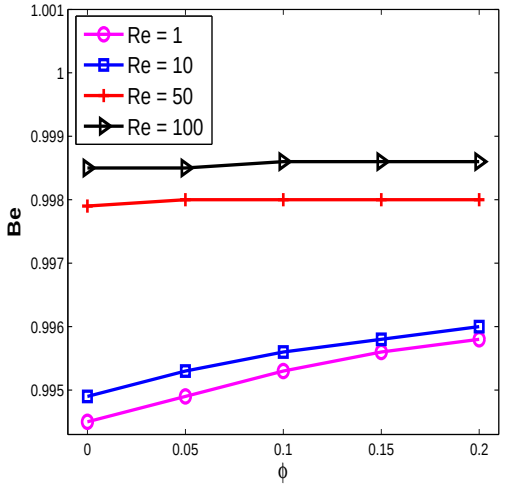

Figure 4.11: Effect of Reynolds number on Bejan number with different nanoparticle volume fraction.

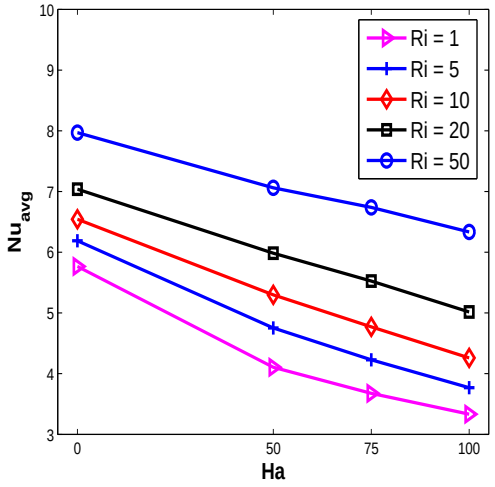

Figure 4.12: Effect of Richardson number on average Nusselt number with different Hartmann number.

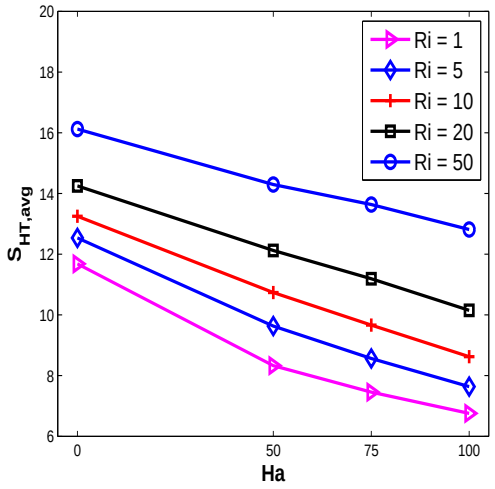

Figure 4.13: Effect of Richardson number on entropy generation due to heat transfer with different Hartmann number.

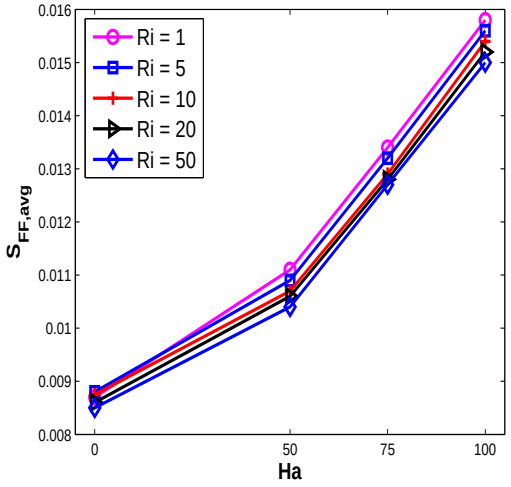

Figure 4.14: Effect of Richardson number on entropy generation due to fluid friction with different Hartmann number.

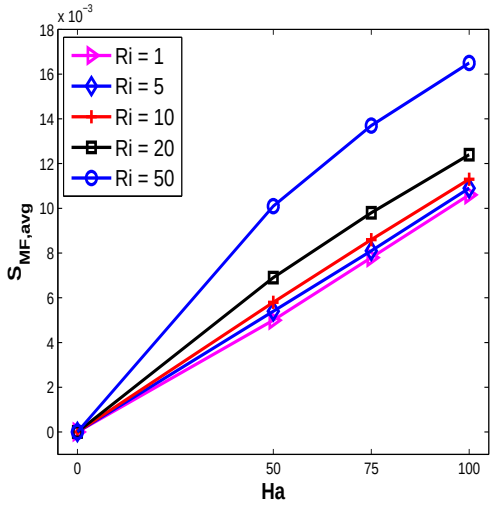

Figure 4.15: Effect of Richardson number on entropy generation due to magnetic field with different Hartmann number.

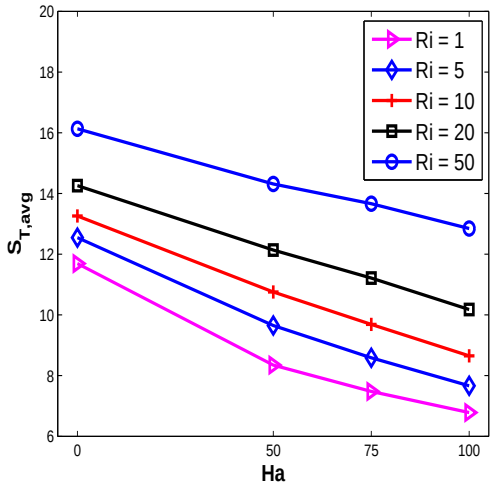

Figure 4.16: Effect of Richardson number on total entropy generation due to magnetic field with different Hartmann number.

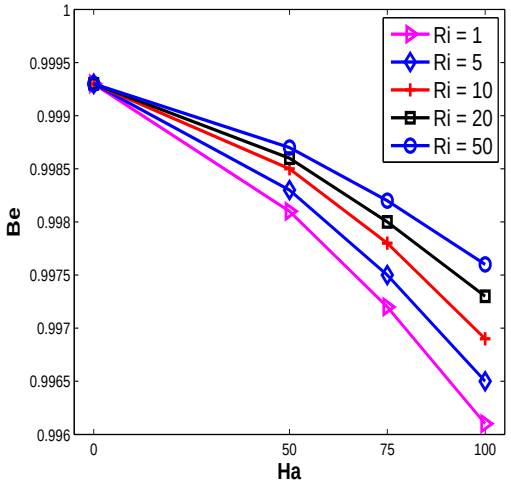

Figure 4.17: Effect of Richardson number on Bejan number with different Hartmann number.

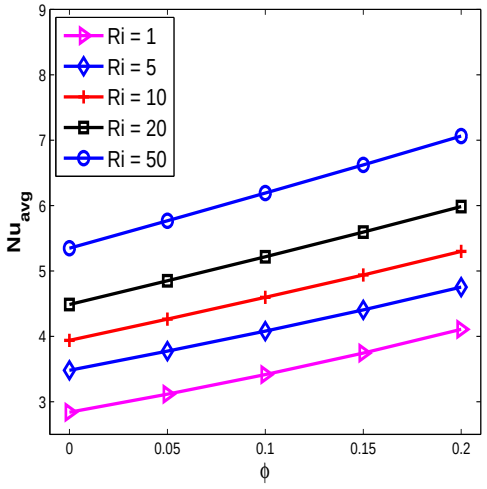

Figure 4.18: Effect of Richardson number on average Nusselt number with different nanoparticle volume fraction.

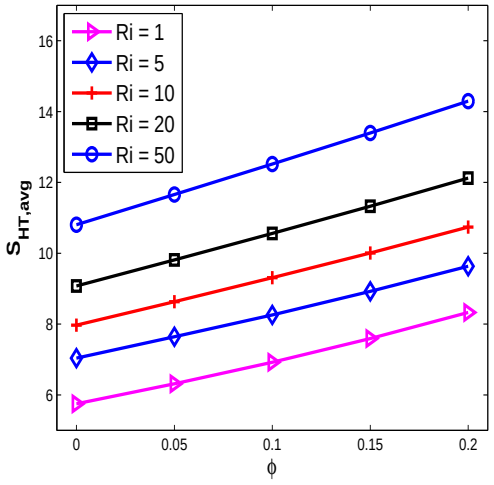

Figure 4.19: Effect of Richardson number on entropy generation due to heat transfer with different nanoparticle volume fraction.

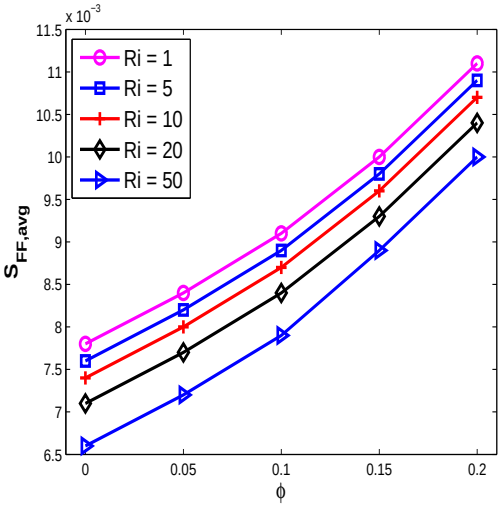

Figure 4.20: Effect of Richardson number on entropy generation due to fluid friction with different nanoparticle volume fraction.

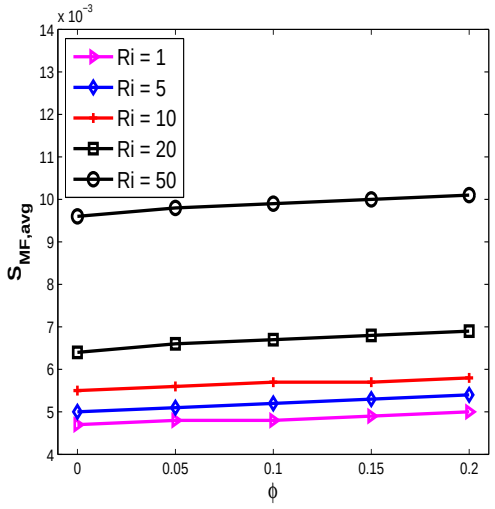

Figure 4.21: Effect of Richardson number on entropy generation due to magnetic field with different nanoparticle volume fraction.

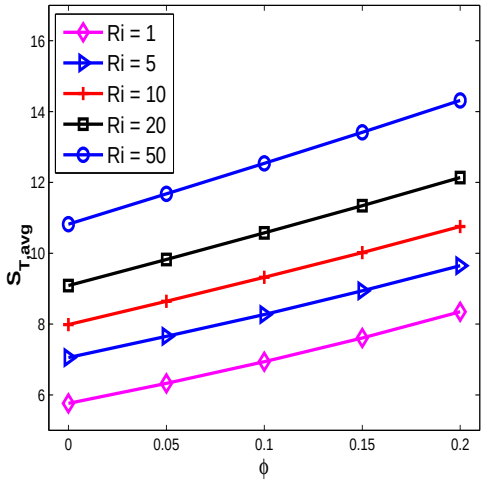

Figure 4.22: Effect of Richardson number on total entropy generation due to magnetic field with different nanoparticle volume fraction.

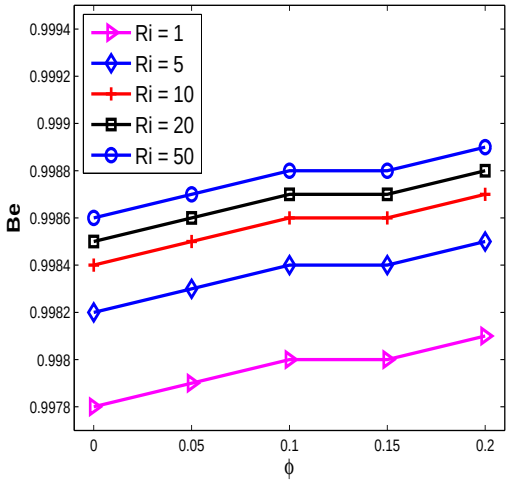

Figure 4.23: Effect of Richardson number on Bejan number with different nanoparticle volume fraction.

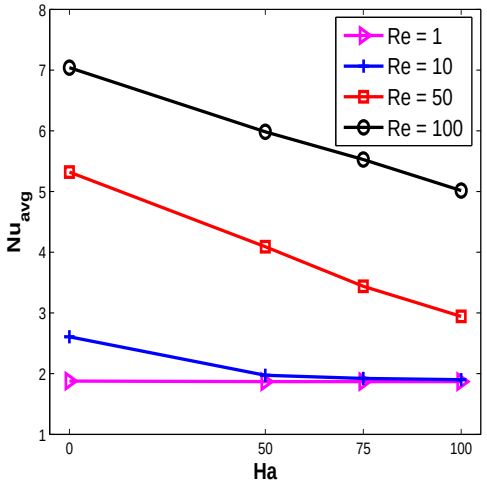

Figure 4.24: Effect of Reynolds number on average Nusselt number with different Hartmann number.

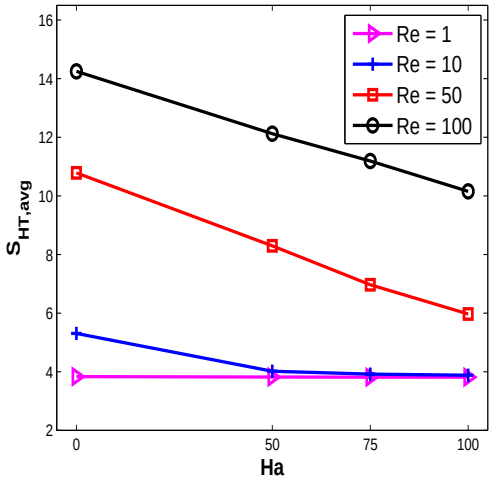

Figure 4.25: Effect of Reynolds number on entropy generation due to heat transfer with different Hartmann number.

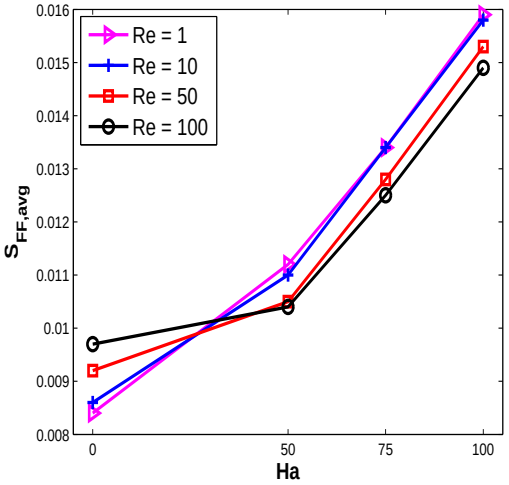

Figure 4.26: Effect of Reynolds number on entropy generation due to fluid friction with different Hartmann number.

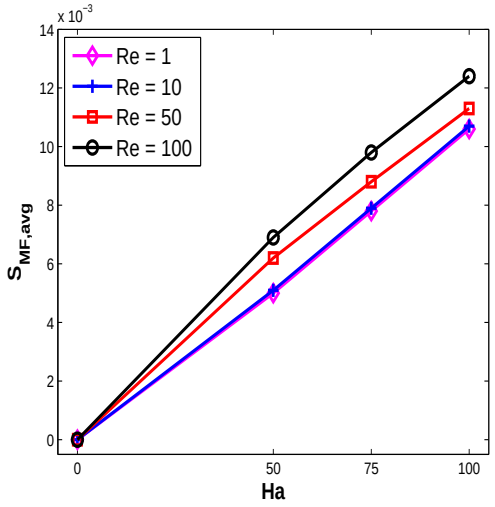

Figure 4.27: Effect of Reynolds number on entropy generation due to magnetic field with different Hartmann number.

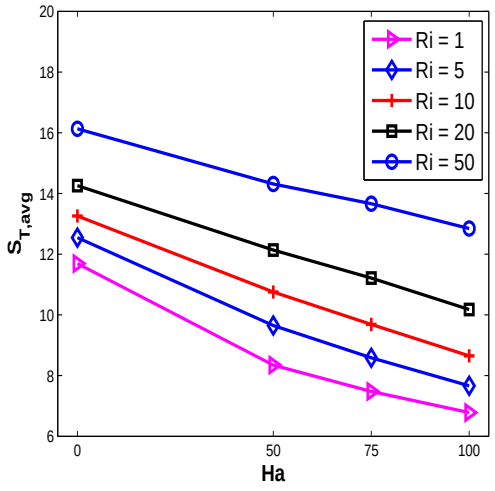

Figure 4.28: Effect of Reynolds number on total entropy generation due to magnetic field with different Hartmann number.

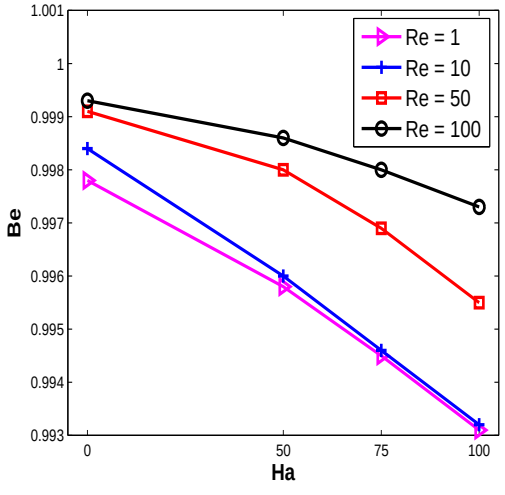

Figure 4.29: Effect of Reynolds number on Bejan number with different Hartmann number.

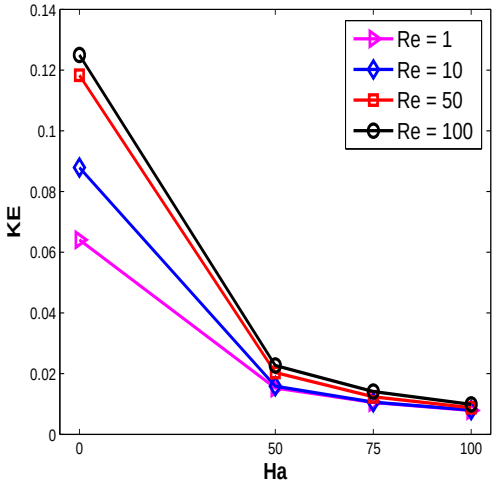

Figure 4.30: Effect of Reynolds number on kinetic energy with different Hartmann number.

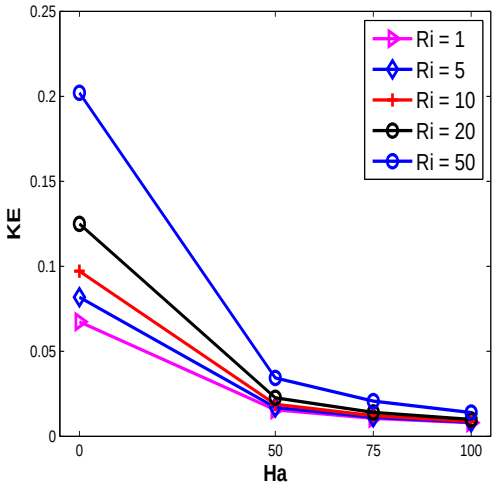

Figure 4.31: Effect of Richardson number on kinetic energy with different Hartmann number.

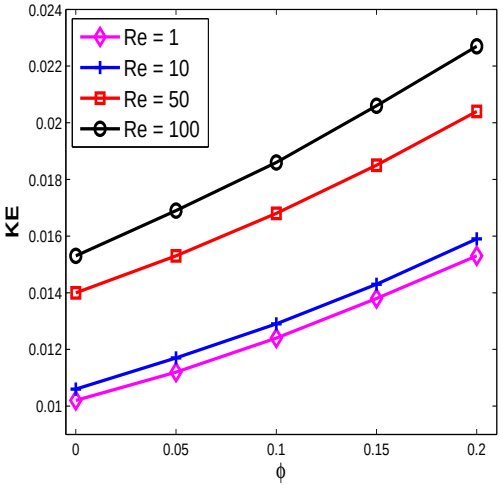

Figure 4.32: Effect of Reynolds number on kinetic energy with different nanoparticle volume fraction.

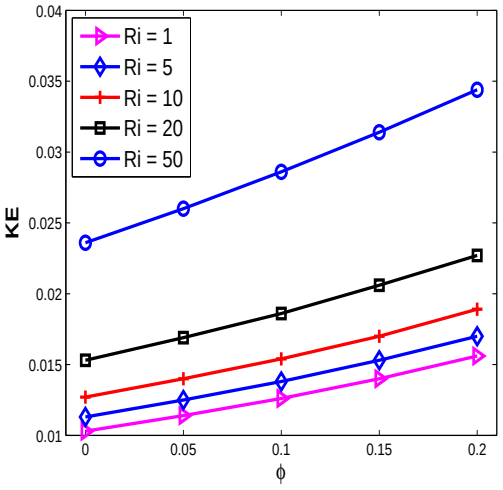

Figure 4.33: Effect of Richardson number on kinetic energy with different nanoparticle volume fraction.

4.5 Closing Remarks

In the present analysis, the mixed convective alumina-water nanofluid flow in a double lid driven cavity with discrete heating in the presence of an inclined magnetic field along with the entropy generation is investigated. The fluid motion is due to the buoyancy force along with the two moving vertical walls. Spatial discretization was carried out using the higher order finite element pair Q_2/P_1^{disc} and the fully implicit Crank-Nicolson is utilized for the temporal discretization. The governing system of nonlinear equations is linearized with the help of Newton's method and the associated linear subproblems are solved by using the Gaussian elimination method. Impacts of the emerging parameters on the fluid flow, temperature distribution and heat transfer have been computed and analyzed. Moreover, S_{HT}, S_{FF}, S_{MF}, S_T, Be and the kinetic energy have been calculated. The main findings are as follows.

- With an increase in Ri, the values of Nu and S_{HT} also increase but for a fixed value of Ri and increasing the Ha, gradual decline in Nu and S_{HT} is observed.
- Total entropy generation S_T and Be augment with an increase in Re and ϕ.

- The S_{FF} declines with a growth in Ri while for a fixed value of Ri and increase in Ha, a gradual reduction in S_{FF} is observed.
- The S_{FF} increases with an augmentation in Re and Ha.
- The Bejan number Be increases with an enhancement in Re while for a fixed value of Re, Bejan number Be gradually decreases with an increase in Ha.
- The kinetic energy increases with an increase in Re, Ri, and ϕ whereas it reduces for the increasing values of Ha.

Chapter 5

MHD Mixed Convective Nanofluid Flow With an Isothermally Heated Square Blockage Inside a Cavity

5.1 Introduction

In this chapter, mixed convection in alumina-water nanofluid filled lid-driven square cavity with an isothermally heated square blockage inside with magnetic field effect has been examined. All the walls of the cavity are at rest except the top wall. A square blockage with isothermal heating is placed at the centre of the cavity. The vertical side walls are adiabatic and the bottom wall is kept at some hot temperature. Flow is generated due to motion of the top wall and buoyancy forces that are produced in the cavity due to temperature gradient. The governing equations are discretized in space using the Galerkin finite element method and time discretization is performed using the Crank-Nicolson scheme. Newton's method is used to cope with discretized nonlinear systems of equations and the Gaussian elimination method has been applied to solve the associated linear subproblems

in each nonlinear iteration at each time level. Analysis has been performed on numerical results in the form of streamlines, isotherms, tables and some useful plots. Influence of emerging parameters on the flow, in specific ranges such as Reynolds number ($1 \leq Re \leq 200$), Richardson number ($0.01 \leq Ri \leq 10$), Hartmann number ($0 \leq Ha \leq 100$), Eckert number ($0 \leq Ec \leq 0.01$) as well as nanoparticles volume fraction ($0 \leq \phi \leq 0.2$) are investigated and findings are very closely comparable to the previous analysis for the special cases in the literature. Calculations of the average Nusselt number, the entropy generation as well as the average temperature in the cavity will be our focus of interest in this chapter. This study is organised in the following way. Section 5.2 illustrates the problem configuration. Section 5.3 contains information about space and time discretizations of the governing equations, the numerical method, code validation and grid independence test. Results based on the numerical simulation have been elaborated in Section 5.4. Finally, conclusion has been drawn in Section 5.5.

5.2 Problem Formulation

5.2.1 The Problem Configuration

The geometry of the present problem is shown in Figure 5.1. It displays a lid driven square cavity of width L containing alumina-water nanofluid. An isothermally heated square blockage with an average temperature of both top cold and bottom hot walls and of width equal to L/4 is placed in the middle of the cavity [135]. Top wall is moving to the right with constant speed U_0, other walls are at kept at rest. Vertical side walls are adiabatic and bottom wall is maintained at hot temperature T_h. Flow is produced in the cavity due to temperature gradient and movement of the top wall. The nanofluid is Newtonian and incompressible. Flow is considered to be unsteady, two dimensional and laminar. A uniform magnetic field of strength B_0 is applied in the x-direction. Induced magnetic field generated by the motion of an electrically conducting fluid is assumed to be negligible

as compared to the applied magnetic field [136]. The base fluid and solid nanoparticles are in thermal equilibrium. Slipping effect between any two phases, radiation effects and viscous dissipation in the energy equation are neglected [93, 96, 137]. Standard Boussinesq model is used to approximate the density in buoyancy term while the other thermo-physical properties [114–116] of the nanofluid are assumed to be constant (see Table 5.1).

Physical properties	H_2O	Al_2O_3
ρ (kg m^{-3})	997.1	3970
C_p (J kg^{-1}K^{-1})	4179	765
k (W m^{-1} K^{-1})	0.613	40
β (K^{-1})	21×10^{-5}	0.85×10^{-5}
σ (Ω m)$^{-1}$	0.05	1×10^{-10}

Table 5.1: Thermo-physical properties of water and alumina.

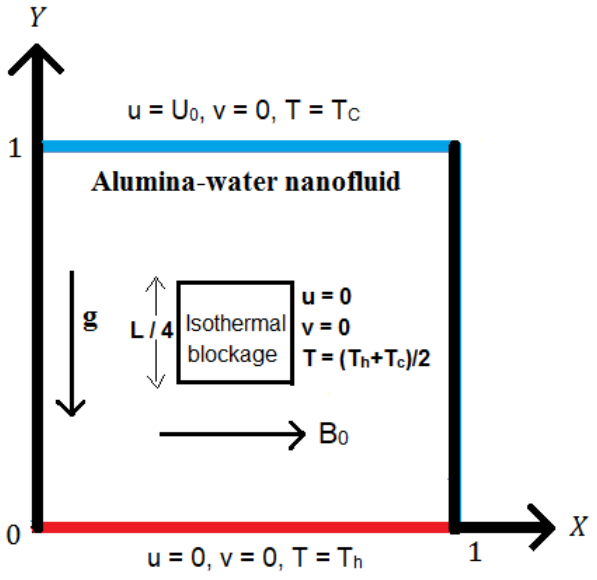

Figure 5.1: Schematic diagram of the physical model.

5.2.2 The Governing Equations

Governing equations [37] can be written as follows:

$$\frac{\partial u}{\partial t} + u\frac{\partial u}{\partial x} + v\frac{\partial u}{\partial y} = -\frac{1}{\rho_{nf}}\frac{\partial p}{\partial x} + \frac{\mu_{nf}}{\rho_{nf}}\left(\frac{\partial^2 u}{\partial x^2} + \frac{\partial^2 u}{\partial y^2}\right), \tag{5.1}$$

$$\frac{\partial v}{\partial t} + u\frac{\partial v}{\partial x} + v\frac{\partial v}{\partial y} = -\frac{1}{\rho_{nf}}\frac{\partial p}{\partial y} + \frac{\mu_{nf}}{\rho_{nf}}\left(\frac{\partial^2 v}{\partial x^2} + \frac{\partial^2 v}{\partial y^2}\right) + \frac{(\rho\beta)_{nf}}{\rho_{nf}}g(T - T_c) - \frac{\sigma_{nf}B_0^2}{\rho_{nf}}v, \tag{5.2}$$

$$\frac{\partial u}{\partial x} + \frac{\partial v}{\partial y} = 0, \tag{5.3}$$

$$\frac{\partial T}{\partial t} + u\frac{\partial T}{\partial x} + v\frac{\partial T}{\partial y} = \alpha_{nf}\left(\frac{\partial^2 T}{\partial x^2} + \frac{\partial^2 T}{\partial y^2}\right) + \frac{\sigma_{nf}B_0^2}{(\rho C_p)_{nf}}v^2. \tag{5.4}$$

5.2.3 The Dimensionless Governing Equations

To convert the governing equations in dimensionless form, following variables are used

$$X = \frac{x}{L},\ Y = \frac{y}{L},\ U = \frac{u}{U_0},\ V = \frac{v}{U_0},\ \theta = \frac{T - T_c}{T_h - T_c},\ P = \frac{p}{\rho_{nf}U_0^2}, Re = \frac{U_0 L}{\nu_f},$$
$$Gr = \frac{g\beta(T_h - T_c)L^3}{\nu_f^2},\ \tau = \frac{tU_0}{L},\ Ha = B_0 L\sqrt{\frac{\sigma_f}{\mu_f}},\ Pr = \frac{\nu_f}{\alpha_f},\ Ri = \frac{Gr}{Re^2},$$
$$S_T = \frac{sT_0^2L^2}{k_f(T_h - T_c)^2},\ Ec = \frac{U_0^2}{(C_p)_f(T_h - T_c)},$$

where U_0, ν_f, α_f and β are imposed lid velocity, kinematic viscosity, thermal diffusibility and the coefficient of thermal expansion respectively of nanofluid, g is the gravitational acceleration.

Dimensionless governing equations could be given as follows:

$$\frac{\partial U}{\partial \tau} + U\frac{\partial U}{\partial X} + V\frac{\partial U}{\partial Y} = -\frac{\partial P}{\partial X} + \frac{1}{Re}\frac{\rho_f}{\rho_{nf}}\frac{1}{(1-\phi)^{2.5}}\left(\frac{\partial^2 U}{\partial X^2} + \frac{\partial^2 U}{\partial Y^2}\right), \tag{5.5}$$

$$\frac{\partial V}{\partial \tau} + U\frac{\partial V}{\partial X} + V\frac{\partial V}{\partial Y} = -\frac{\partial P}{\partial Y} + \frac{1}{Re}\frac{\rho_f}{\rho_{nf}}\frac{1}{(1-\phi)^{2.5}}\left(\frac{\partial^2 V}{\partial X^2} + \frac{\partial^2 V}{\partial Y^2}\right) + Ri\frac{\rho_f}{\rho_{nf}}\left(1 - \phi + \frac{\rho_s\beta_s}{\rho_f\beta_f}\phi\right)\theta - \frac{\rho_f}{\rho_{nf}}\frac{\sigma_{nf}}{\sigma_f}\frac{Ha^2}{Re}V, \tag{5.6}$$

$$\frac{\partial U}{\partial X} + \frac{\partial V}{\partial Y} = 0, \tag{5.7}$$

$$\frac{\partial \theta}{\partial \tau} + U\frac{\partial \theta}{\partial X} + V\frac{\partial \theta}{\partial Y} = \frac{\alpha_{nf}}{\alpha_f}\frac{1}{RePr}\left(\frac{\partial^2 \theta}{\partial X^2} + \frac{\partial^2 \theta}{\partial Y^2}\right) + \frac{Ha^2 Ec}{Re}\frac{\sigma_{nf}}{\sigma_f}\frac{(\rho C_p)_f}{(\rho C_p)_{nf}}V^2. \tag{5.8}$$

The boundary conditions are given in the following way:

At the top wall : $U = 1, \quad V = 0, \quad \theta = 0,$

At the bottom wall : $U = 0, \quad V = 0, \quad \theta = 1,$

At the left and right walls : $U = 0, \quad V = 0, \quad \dfrac{\partial \theta}{\partial X} = 0,$

At the blockage inside : $U = 0, \quad V = 0, \quad \theta = 0.5$

5.2.4 The Effective Nanofluid Properties

The effective density, thermal diffusivity, electrical conductivity, specific heat and the coefficient of thermal expansion of the nanofluid are the same as given in the section 4.2.4 of Chapter 4.

5.2.5 The Entropy Generation

The entropy generation due to various physical sources can be written as follows:

$$s = \frac{k_{nf}}{T_0^2}\left[\left(\frac{\partial T}{\partial x}\right)^2 + \left(\frac{\partial T}{\partial y}\right)^2\right] + \frac{\mu_{nf}}{T_0}\left[2\left(\left(\frac{\partial u}{\partial x}\right)^2 + \left(\frac{\partial v}{\partial y}\right)^2\right) + \left(\frac{\partial u}{\partial y} + \frac{\partial v}{\partial x}\right)^2\right] + \frac{\sigma_{nf} B_0^2}{T_0} v^2, \tag{5.9}$$

where $T_0 = \frac{T_h + T_c}{2}$. The dimensionless entropy generation obtained from Eq. (5.9) is given as follows:

$$S_T = \frac{k_{nf}}{k_f}\left[\left(\frac{\partial \theta}{\partial X}\right)^2 + \left(\frac{\partial \theta}{\partial Y}\right)^2\right] + \chi\frac{\mu_{nf}}{\mu_f}\left[2\left(\left(\frac{\partial U}{\partial X}\right)^2 + \left(\frac{\partial V}{\partial Y}\right)^2\right)\right] + \chi\frac{\mu_{nf}}{\mu_f}\left[\left(\frac{\partial U}{\partial Y} + \frac{\partial V}{\partial X}\right)^2\right] + \chi Ha^2 \frac{\sigma_{nf}}{\sigma_f} V^2, \tag{5.10}$$

where χ is the irreversibility factor that is given by

$$\chi = \frac{\mu_f T_0}{k_f}\left(\frac{U_0}{T_h - T_c}\right)^2. \tag{5.11}$$

Let us write

$$S_T = S_{HT} + S_{FF} + S_{MF}, \tag{5.12}$$

where

$$S_{HT} = \frac{k_{nf}}{k_f}\left[\left(\frac{\partial\theta}{\partial X}\right)^2 + \left(\frac{\partial\theta}{\partial Y}\right)^2\right]. \tag{5.13}$$

Here

$$S_{FF} = \chi\frac{\mu_{nf}}{\mu_f}\left[2\left(\left(\frac{\partial U}{\partial X}\right)^2 + \left(\frac{\partial V}{\partial Y}\right)^2\right) + \left(\frac{\partial U}{\partial Y} + \frac{\partial V}{\partial X}\right)^2\right], \tag{5.14}$$

$$S_{MF} = \chi Ha^2\frac{\sigma_{nf}}{\sigma_f}V^2, \tag{5.15}$$

where S_{HT}, S_{FF} and S_{MF} represent the non-dimensional entropy generation due to heat transfer, fluid friction and magnetic field, respectively. Integrating Eq. (5.10) yields the dimensionless average entropy generation $S_{T,\text{avg}}$ that could be given as follows

$$S_{T,\text{avg}} = \frac{1}{\vartheta}\int S_T d\vartheta = S_{HT,\text{avg}} + S_{FF,\text{avg}} + S_{MF,\text{avg}}. \tag{5.16}$$

Here, ϑ denotes total volume of the nanofluid. Bejan number is given by

$$Be = \frac{S_{HT}}{S_T}. \tag{5.17}$$

5.2.6 Calculation of the Nusselt number

Local Nusselt number and average Nusselt number are given by

$$Nu = -\frac{k_{nf}}{k_f}\left(\frac{\partial\theta}{\partial Y}\right)\Big|_{Y=0,1}, \tag{5.18}$$

$$Nu_{\text{avg}} = \int_0^1 Nu\ dX. \tag{5.19}$$

5.3 The Numerical Approach

5.3.1 Spatial and Temporal Discretization

The system of coupled non-linear partial dierential equations together with given boundary conditions have been discretized numerically by the finite element formulation. The numerical procedure used to solve the governing equations for the present work is based on the Galerkin weighted residual method in which we have used the higher order Stokes element Q_2/P_1^{disc}, where Q_2 element is utilized for the velocity and temperature and P_1^{disc} element is used for the pressure (see 2.5 for detail). The variational or weak form of the governing Eqs. (5.5) - (5.8) is given in the following:

$$\int_\Omega \frac{\partial U}{\partial \tau}\, w\, d\Omega + \int_\Omega \left(U\frac{\partial U}{\partial X} + V\frac{\partial U}{\partial Y}\right) w\, d\Omega = -\int_\Omega \frac{\partial P}{\partial X}\, w\, d\Omega + \frac{1}{Re}\frac{\rho_f}{\rho_{nf}}\frac{1}{(1-\phi)^{2.5}} \int_\Omega \left(\frac{\partial^2 U}{\partial X^2} + \frac{\partial^2 U}{\partial Y^2}\right) w\, d\Omega, \tag{5.20}$$

$$\int_\Omega \frac{\partial V}{\partial \tau}\, w\, d\Omega + \int_\Omega \left(U\frac{\partial V}{\partial X} + V\frac{\partial V}{\partial Y}\right) w\, d\Omega = -\int_\Omega \frac{\partial P}{\partial Y}\, w\, d\Omega + \frac{1}{Re}\frac{\rho_f}{\rho_{nf}}\frac{1}{(1-\phi)^{2.5}} \int_\Omega \left(\frac{\partial^2 V}{\partial X^2} + \frac{\partial^2 V}{\partial Y^2}\right) w\, d\Omega + Ri\frac{\rho_f}{\rho_{nf}}\left(1-\phi+\frac{\rho_s\beta_s}{\rho_f\beta_f}\phi\right)\int_\Omega \theta\, w\, d\Omega - \frac{\rho_f}{\rho_{nf}}\frac{\sigma_{nf}}{\sigma_f}\frac{Ha^2}{Re}\int_\Omega V w\, d\Omega, \tag{5.21}$$

$$\int_\Omega \left(\frac{\partial U}{\partial X} + \frac{\partial V}{\partial Y}\right) q\, d\Omega = 0, \tag{5.22}$$

$$\int_\Omega \frac{\partial \theta}{\partial \tau}\, w\, d\Omega + \int_\Omega \left(U\frac{\partial \theta}{\partial X} + V\frac{\partial \theta}{\partial Y}\right) w\, d\Omega = \frac{\alpha_{nf}}{\alpha_f}\frac{1}{RePr}\int_\Omega \left(\frac{\partial^2 \theta}{\partial X^2} + \frac{\partial^2 \theta}{\partial Y^2}\right) w\, d\Omega + \frac{Ha^2 Ec}{Re}\frac{\sigma_{nf}}{\sigma_f}\frac{(\rho C_p)_f}{(\rho C_p)_{nf}}\int_\Omega V^2 w\, d\Omega \quad . \tag{5.23}$$

Now, the infinite dimensional trial spaces U, V, θ and P are approximated by U_h, V_h, θ_h and P_h, respectively. Moreover, the infinite dimensional test spaces W and Q are approximated by the finite dimensional test spaces W_h and Q_h, respectively,

in such a way that

$$w_h \in W_h \subset H^1(\Omega) = \left\{ s : \Omega \to \mathbb{R} : \int_\Omega |s(x)|^2 dx < \infty, \int_\Omega |s'(x)|^2 dx < \infty \right\},$$
$$q_h \in Q_h \subset L_2(\Omega) = \left\{ g : \Omega \to \mathbb{R} : \int_\Omega |g(x)|^2 dx < \infty \right\}.$$

After the finite dimensional approximation, the Eqs. (5.20) - (5.23) takes the form, given as follows:

$$\int_\Omega \frac{\partial U_h}{\partial \tau}\, w_h\, d\Omega + \int_\Omega \left(U_h \frac{\partial U_h}{\partial X} + V_h \frac{\partial U_h}{\partial Y} \right) w_h\, d\Omega = -\int_\Omega \frac{\partial P_h}{\partial X}\, w_h\, d\Omega + \frac{1}{Re} \frac{\rho_f}{\rho_{nf}} \frac{1}{(1-\phi)^{2.5}} \int_\Omega \left(\frac{\partial^2 U_h}{\partial X^2} + \frac{\partial^2 U_h}{\partial Y^2} \right) w_h\, d\Omega, \tag{5.24}$$

$$\int_\Omega \frac{\partial V_h}{\partial \tau}\, w_h\, d\Omega + \int_\Omega \left(U_h \frac{\partial V_h}{\partial X} + V_h \frac{\partial V_h}{\partial Y} \right) w_h\, d\Omega = -\int_\Omega \frac{\partial P_h}{\partial Y}\, w_h\, d\Omega + \frac{1}{Re} \frac{\rho_f}{\rho_{nf}} \frac{1}{(1-\phi)^{2.5}} \int_\Omega \left(\frac{\partial^2 V_h}{\partial X^2} + \frac{\partial^2 V_h}{\partial Y^2} \right) w_h\, d\Omega + Ri \frac{\rho_f}{\rho_{nf}} \left(1 - \phi + \frac{\rho_s \beta_s}{\rho_f \beta_f} \phi \right) \int_\Omega \theta_h\, w_h\, d\Omega - \frac{\rho_f}{\rho_{nf}} \frac{\sigma_{nf}}{\sigma_f} \frac{Ha^2}{Re} \int_\Omega V_h w_h\, d\Omega, \tag{5.25}$$

$$\int_\Omega \left(\frac{\partial U_h}{\partial X} + \frac{\partial V_h}{\partial Y} \right) q_h\, d\Omega = 0, \tag{5.26}$$

$$\int_\Omega \frac{\partial \theta_h}{\partial \tau}\, w_h\, d\Omega + \int_\Omega \left(U_h \frac{\partial \theta_h}{\partial X} + V_h \frac{\partial \theta_h}{\partial Y} \right) w_h\, d\Omega = \frac{\alpha_{nf}}{\alpha_f} \frac{1}{RePr} \int_\Omega \left(\frac{\partial^2 \theta_h}{\partial X^2} + \frac{\partial^2 \theta_h}{\partial Y^2} \right) w_h\, d\Omega + \frac{Ha^2 Ec}{Re} \frac{\sigma_{nf}}{\sigma_f} \frac{(\rho C_p)_f}{(\rho C_p)_{nf}} \int_\Omega V_h^2 w_h\, d\Omega \quad . \tag{5.27}$$

Using the FEM approximation $U_h(\tau, X, Y) = \sum_{j=1}^{N} U_j(\tau)\xi_j(X, Y)$, $V_h(\tau, X, Y) = \sum_{j=1}^{N} V_j(\tau)\xi_j(X, Y)$, $\theta_h(\tau, X, Y) = \sum_{j=1}^{N} \theta_j(\tau)\xi_j(X, Y)$ and $P_h(X, Y) = \sum_{j=1}^{K} P_j \eta_j(X, Y)$ are the trial functions. Similarly $w_h = \sum_{i=1}^{N} w_i\ \xi_i$ and $q_h = \sum_{i=1}^{K} q_i\ \eta_i$ are the test functions. By the Galerkin finite element model for a typical element Ω_e, the Eqs. (5.24) - (5.27) are transformed into the following system:

$$\int_{\Omega_e} \frac{\partial U_j}{\partial \tau}\xi_j\xi_i \; d\Omega_e + U_j \int_{\Omega_e} \left(\overline{U}\xi_i \frac{\partial \xi_j}{\partial X} + \overline{V}\xi_i \frac{\partial \xi_j}{\partial Y} \right) \; d\Omega_e = -P_j \int_{\Omega_e} \eta_j \frac{\partial \xi_i}{\partial X} \; d\Omega_e$$
$$+ \frac{1}{Re}\frac{\rho_f}{\rho_{nf}}\frac{1}{(1-\phi)^{2.5}} U_j \int_{\Omega_e} \left(\frac{\partial \xi_j}{\partial X}\frac{\partial \xi_i}{\partial X} + \frac{\partial \xi_j}{\partial Y}\frac{\partial \xi_i}{\partial Y} \right) \; d\Omega_e, \tag{5.28}$$

$$\int_{\Omega_e} \frac{\partial V_j}{\partial \tau}\xi_j\xi_i \; d\Omega_e + V_j \int_{\Omega_e} \left(\overline{U}\xi_i \frac{\partial \xi_j}{\partial X} + \overline{V}\xi_i \frac{\partial \xi_j}{\partial Y} \right) \; d\Omega_e = -P_j \int_{\Omega_e} \eta_j \frac{\partial \xi_i}{\partial Y} \; d\Omega_e$$
$$+ \frac{1}{Re}\frac{\rho_f}{\rho_{nf}}\frac{1}{(1-\phi)^{2.5}} V_j \int_{\Omega_e} \left(\frac{\partial \xi_j}{\partial X}\frac{\partial \xi_i}{\partial X} + \frac{\partial \xi_j}{\partial Y}\frac{\partial \xi_i}{\partial Y} \right) \; d\Omega_e$$
$$+ Ri\frac{\rho_f}{\rho_{nf}} \left(1 - \phi + \frac{\rho_s \beta_s}{\rho_f \beta_f}\phi \right) \theta_j \int_{\Omega_e} \xi_j\xi_i \; d\Omega_e - \frac{\rho_f}{\rho_{nf}}\frac{\sigma_{nf}}{\sigma_f}\frac{Ha^2}{Re} V_j \int_{\Omega_e} \xi_j\xi_i \; d\Omega_e, \tag{5.29}$$

$$U_j \int_{\Omega_e} \frac{\partial \xi_j}{\partial X}\eta_i \; d\Omega_e + V_j \int_{\Omega_e} \frac{\partial \xi_j}{\partial Y}\eta_i \; d\Omega_e = 0, \tag{5.30}$$

$$\int_{\Omega_e} \frac{\partial \theta_j}{\partial \tau}\xi_j\xi_i \; d\Omega_e + \theta_j \int_{\Omega_e} \left(\overline{U}\xi_i \frac{\partial \xi_j}{\partial X} + \overline{V}\xi_i \frac{\partial \xi_j}{\partial Y} \right) \; d\Omega_e$$
$$= \frac{1}{RePr}\theta_j \int_{\Omega_e} \left(\frac{\partial \xi_j}{\partial X}\frac{\partial \xi_i}{\partial X} + \frac{\partial \xi_j}{\partial Y}\frac{\partial \xi_i}{\partial Y} \right) \; d\Omega_e$$
$$+ \frac{Ha^2 Ec}{Re}\frac{\sigma_{nf}}{\sigma_f}\frac{(\rho C_p)_f}{(\rho C_p)_{nf}} V_j \int_{\Omega_e} \overline{V}\xi_j\xi_i \; d\Omega_e. \tag{5.31}$$

The final system can be expressed in the following comprehensive form:

$$[\mathbf{M^e}]\{\dot{\mathbf{u}}^\mathbf{e}\} + [\mathbf{K^e}][\mathbf{u^e}] = \{\mathbf{F^e}\}, \tag{5.32}$$

$$[\mathbf{M^e}]\{\dot{\mathbf{u}}^\mathbf{e}\} + \underbrace{\begin{bmatrix} [K_{ji}^{11}] & [K_{ji}^{12}] & [K_{ji}^{13}] & [K_{ji}^{14}] \\ [K_{ji}^{21}] & [K_{ji}^{22}] & [K_{ji}^{23}] & [K_{ji}^{24}] \\ [K_{ji}^{31}] & [K_{ji}^{32}] & [K_{ji}^{33}] & [K_{ji}^{34}] \\ [K_{ji}^{41}] & [K_{ji}^{42}] & [K_{ji}^{43}] & [K_{ji}^{44}] \end{bmatrix}}_{\mathbf{K^e}} \underbrace{\begin{bmatrix} \{\underline{U}\} \\ \{\underline{V}\} \\ \{\underline{P}\} \\ \{\underline{\theta}\} \end{bmatrix}}_{\mathbf{u^e}} = \underbrace{\begin{bmatrix} \{\underline{F^1}\} \\ \{\underline{F^2}\} \\ \{\underline{F^3}\} \\ \{\underline{F^4}\} \end{bmatrix}}_{\mathbf{F^e}}, \tag{5.33}$$

where

$$[\mathbf{M^e}] = \begin{bmatrix} [M_{ji}^{11}] & [M_{ji}^{12}] & [M_{ji}^{13}] & [M_{ji}^{14}] \\ [M_{ji}^{21}] & [M_{ji}^{22}] & [M_{ji}^{23}] & [M_{ji}^{24}] \\ [M_{ji}^{31}] & [M_{ji}^{32}] & [M_{ji}^{33}] & [M_{ji}^{34}] \\ [M_{ji}^{41}] & [M_{ji}^{42}] & [M_{ji}^{43}] & [M_{ji}^{44}] \end{bmatrix} \tag{5.34}$$

In the above expression (5.34), $[\mathbf{M^e}]$ is the elemental block mass matrix in which all the block matrices are zero except $[M_{ji}^{11}] = [M_{ji}^{22}] = [M_{ji}^{44}] = M = \int_{\Omega_e} \xi_j \xi_i \, d\Omega_e$ where the variation of i and j depends on the choice of the basis function and the geometric element considered. Furthermore, $\{\dot{\mathbf{u}}^\mathbf{e}\}$, $\mathbf{K^e}$, $\mathbf{u^e}$ and $\mathbf{F^e}$ in the expression (5.33) are said to be the time derivative vector for the nodal unknowns, the stiffness block matrix, the block solution vector for the nodal unknowns and the right hand side block vector at an element level, respectively. For the sake of brevity, the boundary integral is also included in $\mathbf{F^e}$. In stiffness block matrix,

$$
\begin{aligned}
K_{ji}^{11} &= \frac{1}{Re}\frac{\rho_f}{\rho_{nf}}\frac{1}{(1-\phi)^{2.5}}\int_{\Omega_e}\left(\left(\frac{\partial \xi_j}{\partial X}\frac{\partial \xi_i}{\partial X}+\frac{\partial \xi_j}{\partial Y}\frac{\partial \xi_i}{\partial Y}\right)+\left(\overline{U}\xi_i\frac{\partial \xi_j}{\partial X}+\overline{V}\xi_i\frac{\partial \xi_j}{\partial Y}\right)\right)\, d\Omega_e,\\
K_{ji}^{22} &= \frac{1}{Re}\frac{\rho_f}{\rho_{nf}}\frac{1}{(1-\phi)^{2.5}}\int_{\Omega_e}\left(\left(\frac{\partial \xi_j}{\partial X}\frac{\partial \xi_i}{\partial X}+\frac{\partial \xi_j}{\partial Y}\frac{\partial \xi_i}{\partial Y}\right)+\left(\overline{U}\xi_i\frac{\partial \xi_j}{\partial X}+\overline{V}\xi_i\frac{\partial \xi_j}{\partial Y}\right)\right)\, d\Omega_e,\\
&\quad+\frac{\rho_f}{\rho_{nf}}\frac{\sigma_{nf}}{\sigma_f}\frac{Ha^2}{Re}\int_{\Omega_e}\xi_j\xi_i d\Omega_e,\\
K_{ji}^{42} &= -\frac{Ha^2 Ec}{Re}\frac{\sigma_{nf}}{\sigma_f}\frac{(\rho C_p)_f}{(\rho C_p)_{nf}}\int_{\Omega_e}\overline{V}\xi_j\xi_i\, d\Omega_e,\\
K_{ji}^{44} &= \frac{\alpha_{nf}}{\alpha_f}\frac{1}{RePr}\int_{\Omega_e}\left(\frac{\partial \xi_j}{\partial X}\frac{\partial \xi_i}{\partial X}+\frac{\partial \xi_j}{\partial Y}\frac{\partial \xi_i}{\partial Y}\right)\, d\Omega_e+\int_{\Omega_e}\left(\overline{U}\xi_i\frac{\partial \xi_j}{\partial X}+\overline{V}\xi_i\frac{\partial \xi_j}{\partial Y}\right)\, d\Omega_e \quad ,\\
K_{ji}^{24} &= -Ri\frac{\rho_f}{\rho_{nf}}\left(1-\phi+\frac{\rho_s\beta_s\phi}{\rho_f\beta_f}\right)\int_{\Omega_e}\xi_j\xi_i\, d\Omega_e \quad ,\\
K_{ji}^{13} &= -\int_{\Omega_e}\eta_j\frac{\partial \xi_i}{\partial X}d\Omega_e \quad ,\\
K_{ji}^{23} &= -\int_{\Omega_e}\eta_j\frac{\partial \xi_i}{\partial Y}d\Omega_e \quad ,\\
K_{ji}^{31} &= \int_{\Omega_e}\frac{\partial \xi_j}{\partial X}\eta_i d\Omega_e \quad ,\\
K_{ji}^{32} &= \int_{\Omega_e}\frac{\partial \xi_j}{\partial Y}\eta_i d\Omega_e \quad ,\\
K_{ji}^{12} &= K_{ji}^{21} = K_{ji}^{14} = K_{ji}^{33} = K_{ji}^{34} = K_{ji}^{41} = K_{ji}^{43} = 0,\\
\overline{U} &= \sum_{j=1}^{N} U_j\xi_j, \overline{V} = \sum_{j=1}^{N} V_j\xi_j.
\end{aligned}
$$

The above system (5.33) involves the nodal unknowns $\mathbf{u^e}$ and the time dependent terms $\{\dot{\mathbf{u}}^\mathbf{e}\}$. Time discretization of the nodal unknowns still remains to do. Time discretization have been performed utilizing the Crank-Nicolson method (see 2.4 for detail). We have utilized Q_2/P_1^{disc} for space discretization (see 2.5 for detail).

After discretization in the space and time, we obtain an algebraic system of nonlinear equations. Integration regarding each term of these equations is performed by the Gaussian quadrature method. Then the implementation of boundary conditions is carried out and linear algebraic equations are obtained from nonlinear equations using the iterative Newton's method. Some tolerance value is prescribed to see the optimized minimum difference of the current values of the variables to the previous iteration values by achieving the convergence of the solution of an iterative scheme. In other words, the adopted criterion to stop the iterative scheme could be given as follows

$$\left|\frac{\Gamma^{n+1}-\Gamma^{n}}{\Gamma^{n+1}}\right| \leq 10^{-6}, \tag{5.35}$$

where U, V, P or θ are denoted by a general variable Γ. Superscript n represents the iteration number in the above expression. Finally, these linear equations are computed by the Gaussian elimination method in each time level.

5.3.2 Code Validation and Grid Independence Test

Code validation has been performed for free convection results published in the literature and given in Table 3.4 of chapter 3, for various computed variables. Code validation has also been presented in Table 3.3 for mixed convection flow in the section 3.3.2 of Chapter 3 and the results have an excellent agreement for both of the cases. In addition, code validation has been provided in Table 5.2 for a particular case of isothermal blockage in a cavity and results are found to agree with [138]. Grid convergence test is performed for average Nusselt number and given in Table 5.3 for $Re = 100, \phi = 0.2, Pr = 6.2, Ha = 25, Ec = 0.0001$ together with the number of elements (#EL) and the total number of all space degrees of freedom (#DOFs) which are needed to represent the discrete velocity, temperature and pressure solution with respect to the used discretization. A uniform grid at mesh level $\ell = 8$ with #EL = 65536 is found to meet the requirements of both the grid independency study and the computational time limits. Further refinement

of grids produce no significant changes. However, finer grids may be considered for higher values of Reynolds or Richardson number.

Eccentricity	$(0,0)$		
Nu_{avg}	Ri	Present	Islam *et al.* [138]
	0.1	5.5317	5.6118
	1	5.5684	5.6935
	10	7.9029	7.9083

Table 5.2: Comparison of the present results with those of Islam *et al.* [138]

ℓ	#EL	#DOFs	$Nu_{\text{avg}}(Ri=1)$	$Nu_{\text{avg}}(Ri=10)$
3	64	1056	4.459971	7.081795
4	256	4032	5.138374	8.390714
5	1024	15744	5.508233	9.150767
6	4096	62208	5.674757	9.534331
7	16384	247296	5.741560	9.719424
8	65536	986112	5.774757	9.814020
9	262144	3938304	5.780689	9.810275

Table 5.3: Results of grid independence test for alumina-water nanofluid.

5.4 Results and Discussion

In this work, mixed convection in alumina-water nanofluid filled lid driven square cavity with an isothermally heated square blockage inside with magnetic field effect has been examined. In the whole study standard values ($Re = 100, Ri = 10, \phi = 0.2, Ha = 25, Ec = 0.0001, Pr = 6.2$) have been taken unless these are mentioned. We have considered three cases including the forced convection, the mixed convection and the free convection.

Figure 5.2 demonstrates the influence of Hartmann number on streamlines and isotherms for forced convection case ($Ri = 0.1$). Magnetic field is applied parallel to x-axis. In the absence of magnetic field ($Ha = 0$) clockwise rotating

vortex with its centre above the blockage near the right top corner of the cavity has been noticed. Streamlines are more densely distributed near the top moving wall that indicates the region of higher fluid velocity whereas coarse distribution of streamlines has been observed away from the top moving wall. When magnetic field strength is increased up to $Ha = 25$, flow circulation is reduced that indicates a decrease in fluid velocity and more of the streamlines occur near the top moving wall and above the central block. When magnetic field strength is increased up to $Ha = 50$ and $Ha = 100$, all the streamlines are restricted to the small area near the top moving wall and above the central blockage that indicate a reduction in the fluid flow in the cavity. In fact, the Lorentz force is generated in opposite direction of flow due to the existence of the magnetic field. For $Ha = 0$, isotherms are clustered near the hot bottom wall and around isothermal blockage that indicate the high temperature gradient in that region. Due to shear forces, isotherms are moved towards top of the left adiabatic wall. Hence, thermal boundary layer occurs in this region. When strength of magnetic field is increased up to $Ha = 100$, a slight change has been observed in isotherms behavior. The diagonal lines from bottom of the right adiabatic wall to the top of left adiabatic wall gradually become parallel to the bottom hot wall.

Figure 5.3 depicts the effect of Hartmann number on streamlines and isotherms for mixed convection case ($Ri = 1$). In this case, buoyancy-induced flow due to hot bottom wall or isothermal blockage and shear-driven flow due to top moving wall play an equal role in the fluid flow and temperature distribution in the cavity. For $Ha = 0$, more streamlines (compared to forced convection case) are densely distributed around the central block that show buoyancy also play its role this time. Moreover, weak circulation region is observed in the centre of rotating vortex above the block. When strength of magnetic field is increased up to $Ha = 25$, number of coarsely distributed streamlines around the block is less (compared to $Ha = 0$) but is more as compared to forced convection regime. It indicates a reduction in the fluid flow in the cavity due to application of magnetic field. For the case of $Ha = 50$ and $Ha = 100$, streamlines are clustered to the top wall and

are restricted to a small area showing more decrease in fluid velocity in the cavity. Isotherms behavior slightly changes as compared to the case of forced convection.

Figure 5.4 displays the impact of Hartmann numbers on streamlines and isotherms for natural or free convection regime ($Ri = 10$). In this case buoyancy-driven flow is dominant over shear-driven flow. For $Ha = 0$, streamlines are almost equally distributed and are slightly stretched diagonally to the top right corner due to movement of the top wall. This indicates that fluid flow occurs due to bottom hot wall. Moreover, weak circulation of rotating vortex is observed in the centre of the cavity around the central blockage that shows reduction in fluid flow in this area. When magnetic field strength is enhanced up to $Ha = 25$, weak circulating centre of clockwise rotating vortex has been shifted to the area above the blockage that shows a decrease in fluid velocity. For $Ha = 50$, coarse distribution of streamlines around the left, right and bottom of the blockage has been observed. Similarly, more streamlines are squeezed to the area near the top wall above the blockage for the case of $Ha = 100$ indicating that most of the fluid flow occurs in this region. Isotherms are densely distributed near the hot bottom wall and around isothermal blockage. This indicates high temperature gradient and development of thin boundary layer over the hot wall and blockage surfaces.

Figure 5.5 demonstrates the influence of Richardson number on streamlines and isotherms for Eckert number 10^{-2} . For $Ri = 0.01$, shear forces are dominant in the cavity and streamlines are mostly restricted to the area near the top moving wall above the central blockage. Increasing Ri up to 1, shear forces and buoyancy forces contribute equally thus more streamlines can be seen near the bottom wall. Enhancing Ri from 1 to 10, fluid movement has been observed throughout the whole cavity around the central blockage due to free convection. Isotherms move diagonally from the bottom of right adiabatic wall to the top of left adiabatic wall and become clustered around the central isothermal blockage for forced convection regime ($Ri = 0.1$). For mixed convection mode ($Ri = 1$), isotherms are clustered near the bottom hot wall. For free convection case ($Ri = 10$), most of

the isotherms become parallel to the hot bottom wall due to dominating buoyancy forces.

Effect of Eckert number on average Nusselt number, average temperature, average entropy generation due to heat transfer and average total entropy generation has been demonstrated by Figures 5.6-5.9. Since we have selected very small variation of Eckert number therefore mild effect has been observed in all of the convection regimes for $Ec = 10^{-4}, 10^{-3}$ and 10^{-2}. Variation is almost same for the case of $B_0 = 0$, i.e. , $Ec = 0$ to that of $Ec = 10^{-4}$, so this is not shown in Figures 5.6-5.9. A slight decrease in average Nusselt number with an increase in Eckert number has been noticed in Figure 5.6. Eckert number generates an enhancement in average temperature of the cavity that can be visualized from Figure 5.7. Average entropy generation due to heat transfer and average total entropy generation increase with a growth in Eckert number as depicted in Figures 5.8 and 5.9, respectively.

Figures 5.10-5.13 delineate the effect of Hartmann number on average Nusselt number, entropy generation due to heat transfer, Bejan number and kinetic energy with $Re = 1, 10, 100, 200$. It is evident from Figure 5.10 that increase in magnetic field strength causes to decrease in average Nusselt number. This is due to the fact that movement of buoyancy-induced flow slow down and shear forces becomes dominant by the application of magnetic field. In fact, Lorentz forces have resistance against thermal buoyancy forces. Influence of magnetic field intensity on average entropy generation due to heat transfer, Bejan number and kinetic energy has been illustrated by Figures 5.11-5.13, respectively. All these quantities reduce with a rise in the strength of magnetic field.

For optimum utilization of energy, it becomes important to better understand different convection modes in the cavity. Here, effect of three convection modes namely forced convection ($Ri = 0.1$), mixed convection ($Ri = 1$) and free convection ($Ri = 10$) on various emerging parameters as a function of Hartmann

number has been illustrated in Figures 5.14-5.21. It can be viewed from Figure 5.14 that average Nusselt number decreases with an increase in magnetic field strength for different Richardson number. Average temperature in the cavity is augmented with a growth in Hartmann number as ellucidated by Figure 5.15. Average entropy generation due to heat transfer, fluid friction and magnetic field have been portrayed by Figures 5.16, 5.17 and 5.18, respectively. Average entropy generation due to heat transfer declines by the application of magnetic field. Entropy generation due to fluid friction is increased for forced and mixed convection cases whereas in natural convection regime, increasing Ha from 0 to 50, it decreases then starts increasing beyond $Ha = 50$. Entropy generation due to magnetic field is enhanced monotonically for small values of Richardson number ($Ri = 0.1, 1$) but for natural convection case ($Ri = 10$), it amplifies up to $Ha = 50$ then starts decreasing for higher magnetic field strength. Average total entropy generation and Bejan number gradually decrease with an augmentation in magnetic field strength that can be visualized from Figures 5.19 and 5.20, respectively. By comparing the Figures 5.16 and 5.19 quantitatively, one can see that average entropy generation due to heat transfer and average total entropy generation have almost same magnitudes. Hence, it can be deduced that irreversibility is mostly generated due to heat transfer. Fluid friction and magnetic field play a little role in total irreversibility in the cavity. Kinetic energy declines with an increase in the intensity of magnetic field as shown in Figure 5.21.

Effect of Eckert number on average Nusselt number and kinetic energy as a function of nanoparticles volume fraction has been illustrated by Figures 5.22 and 5.23, respectively. It is examined that average Nusselt number and kinetic energy increase with an augmentation in nanoparticles volume fraction but with an enhancement in Eckert both have opposite behaviors, i.e., average Nusselt number decrease whereas kinetic energy amplifies. Figures 5.24 and 5.25 demonstrate the effect of nanoparticles volume fraction as a function of Eckert number on average temperature and average total entropy generation, respectively. It is found that both quantities augment with a growth in Eckert number.

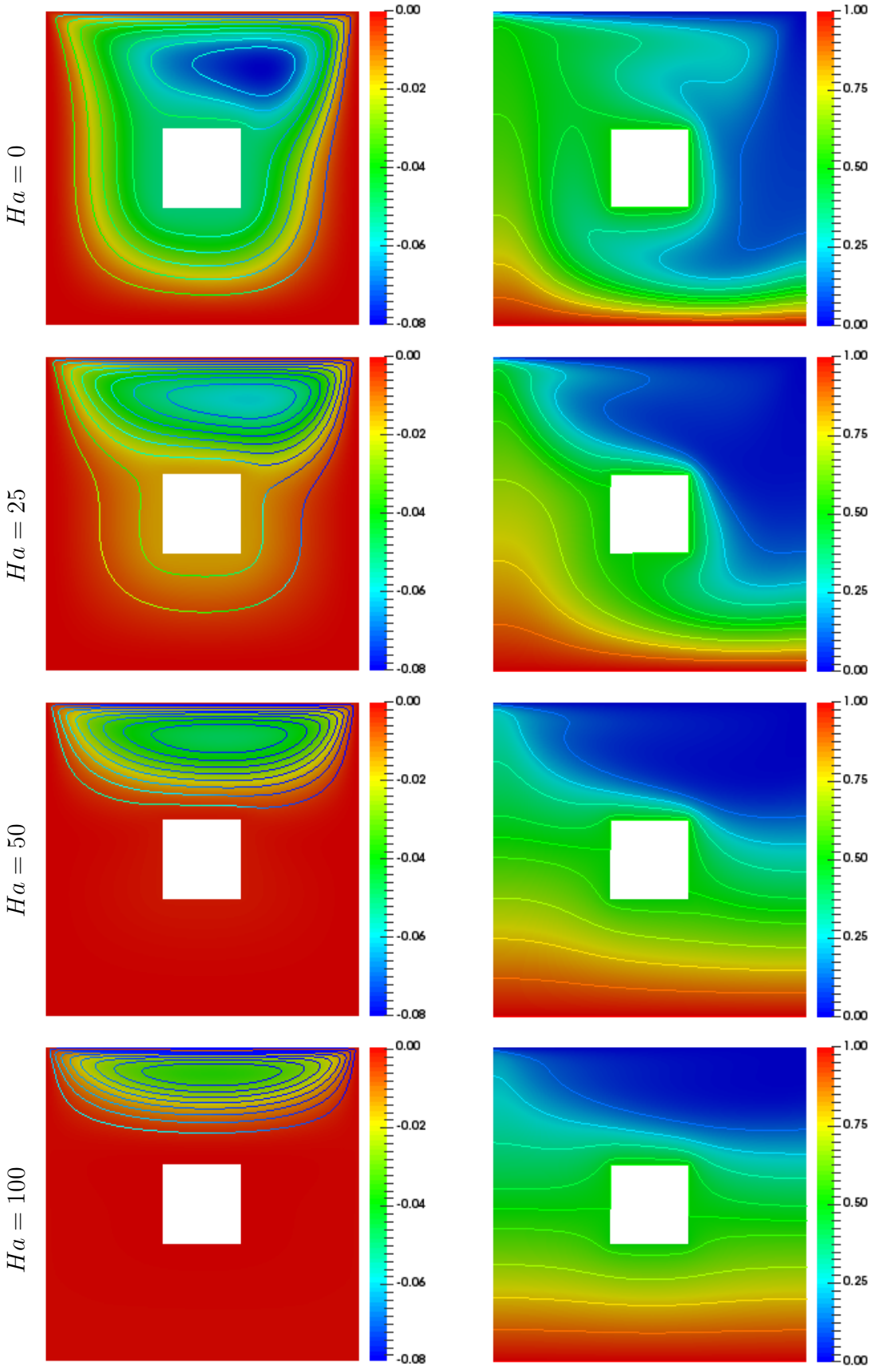

Figure 5.2: Effect of Hartmann number on streamlines and isotherms for $Ri = 0.1$.

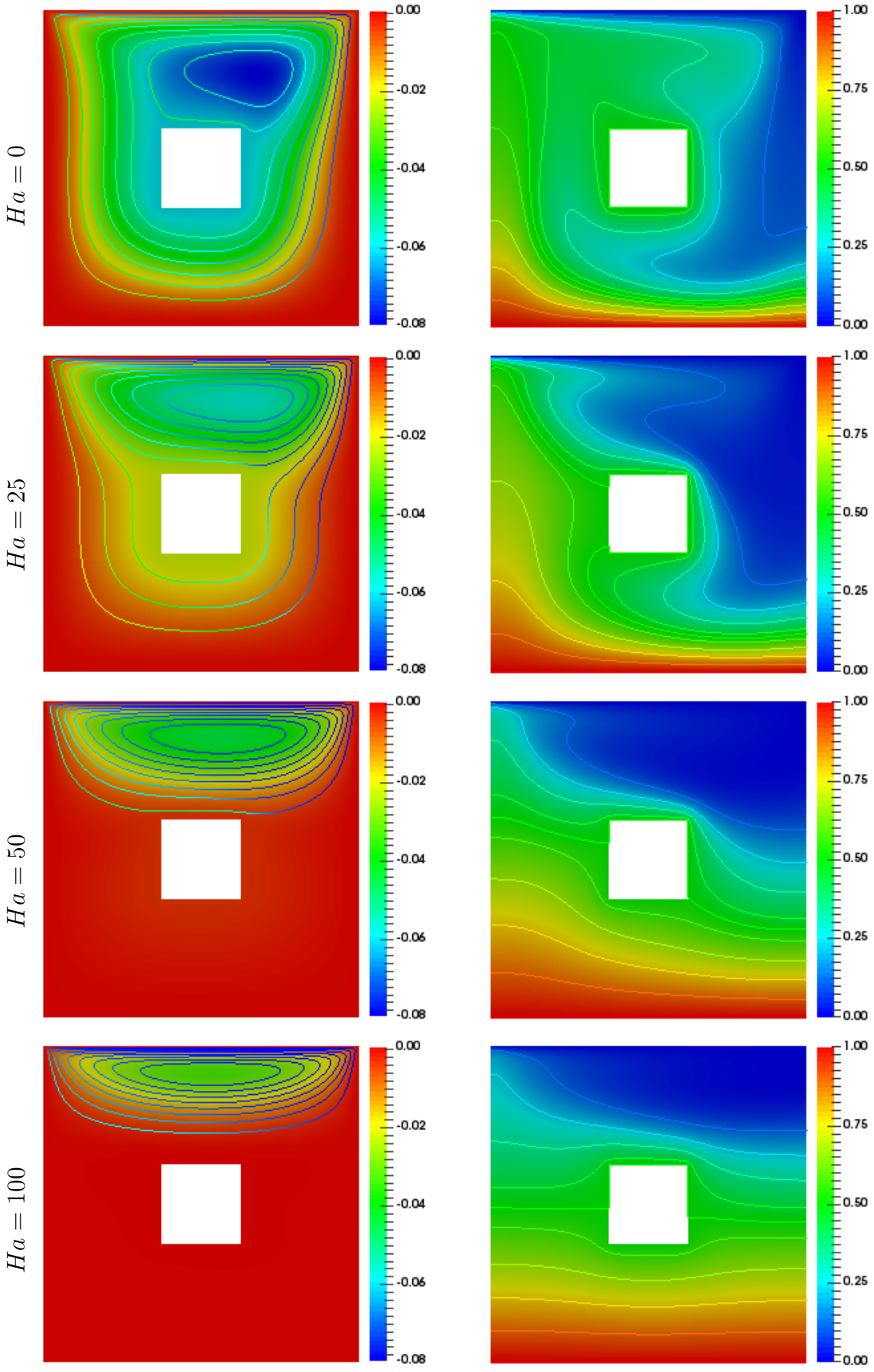

Figure 5.3: Effect of Hartmann number on streamlines and isotherms for $Ri = 1$.

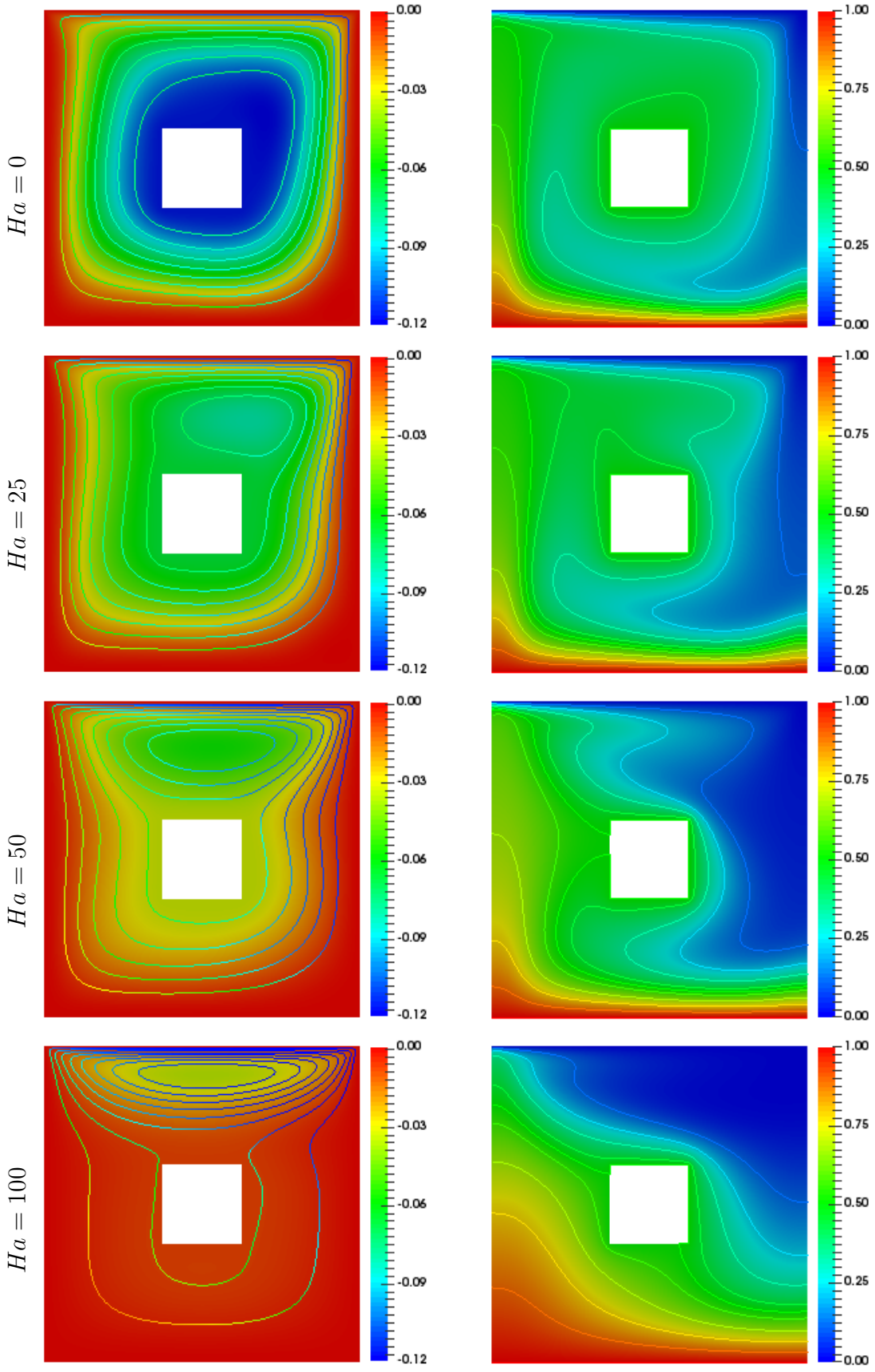

Figure 5.4: Effect of Hartmann number on streamlines and isotherms for $Ri = 10$.

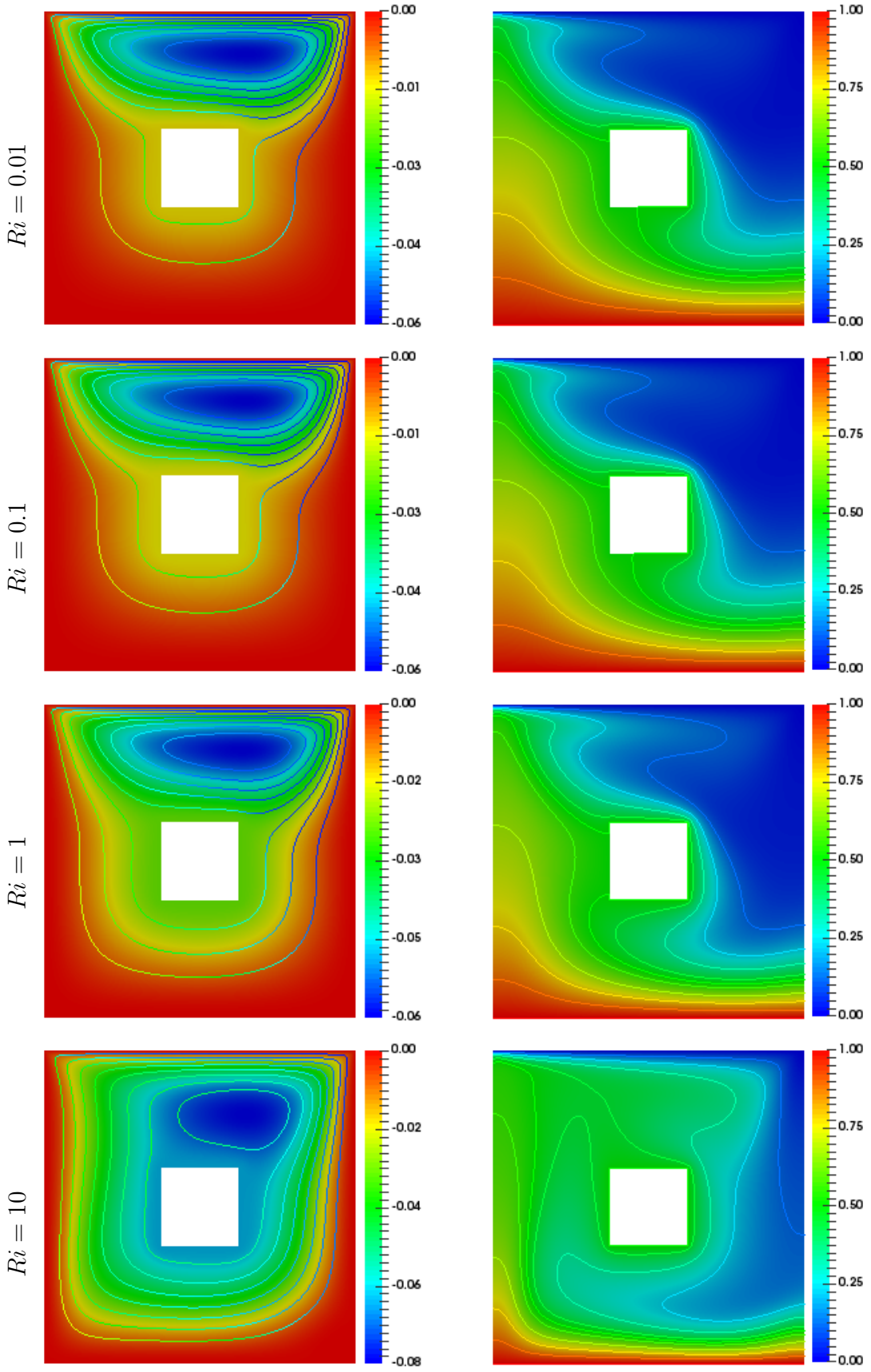

Figure 5.5: Effect of Richardson number on streamlines and isotherms.

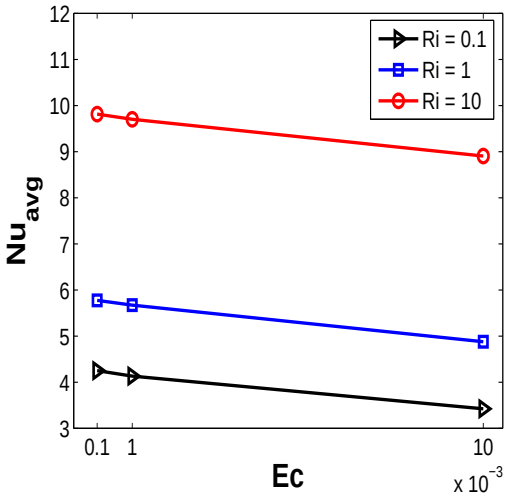

Figure 5.6: Variation of average Nusselt number as a function of Eckert number for different Richardson numbers.

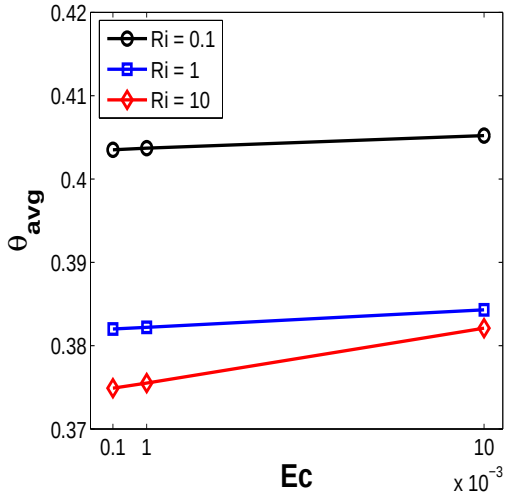

Figure 5.7: Variation of average temperature as a function of Eckert number for different Richardson numbers.

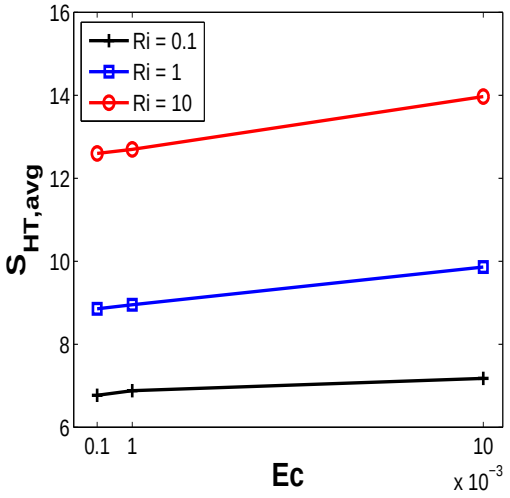

Figure 5.8: Variation of average entropy generation due to heat transfer as a function of Eckert number for different Richardson numbers.

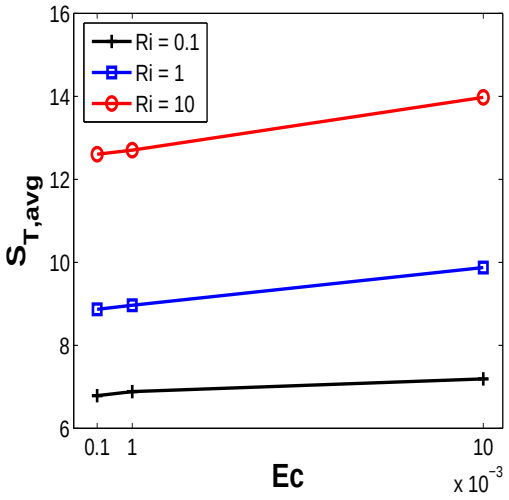

Figure 5.9: Variation of average total entropy generation as a function of Eckert number for different Richardson numbers.

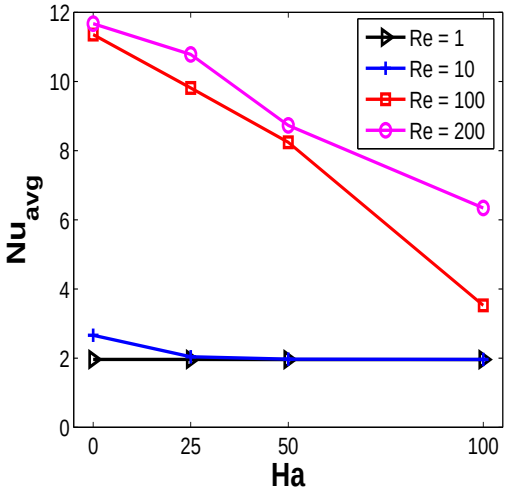

Figure 5.10: Variation of average Nusselt number as a function of Hartmann number for different Reynolds number.

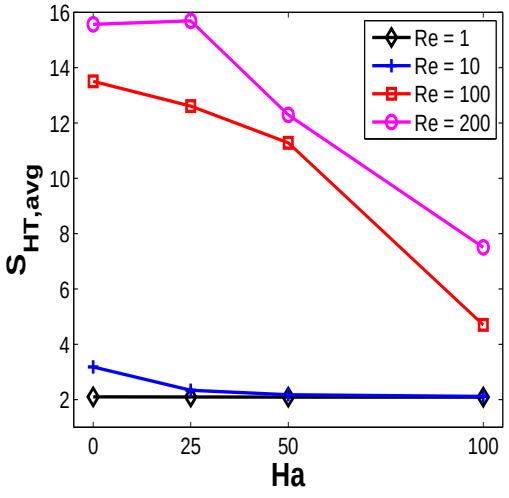

Figure 5.11: Variation of average entropy generation due to heat transfer as a function of Hartmann number for different Reynolds number.

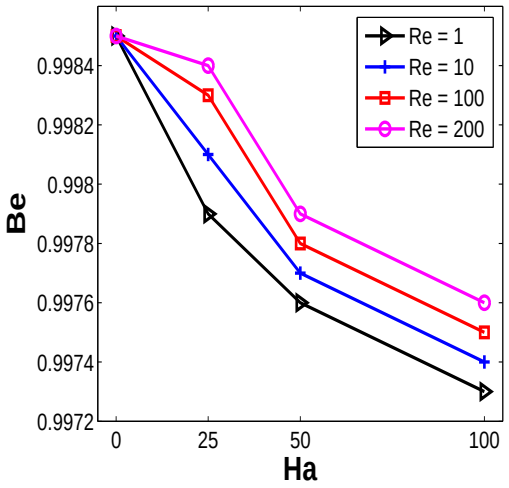

Figure 5.12: Variation of Bejan number as a function of Hartmann number for different Reynolds number.

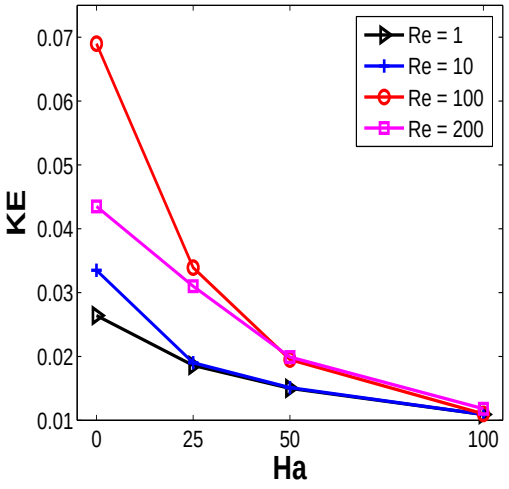

Figure 5.13: Variation of kinetic energy as a function of Hartmann number for different Reynolds number.

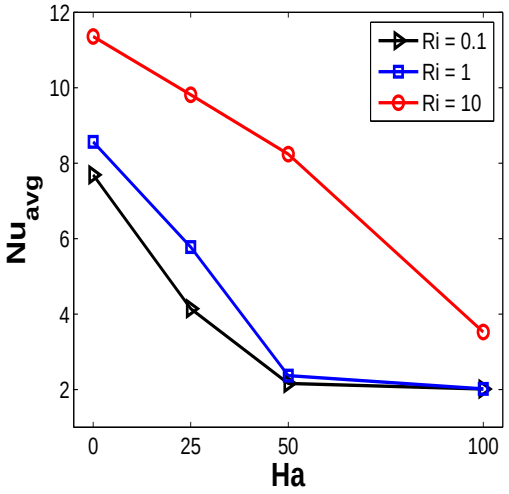

Figure 5.14: Variation of average Nusselt number as a function of Hartmann number for different Richardson numbers.

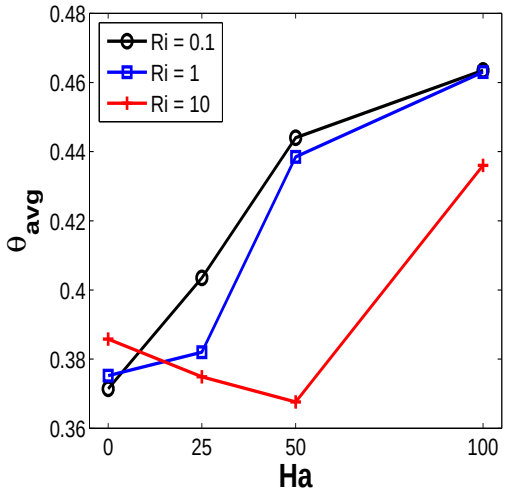

Figure 5.15: Variation of average temperature as a function of Hartmann number for different Richardson numbers.

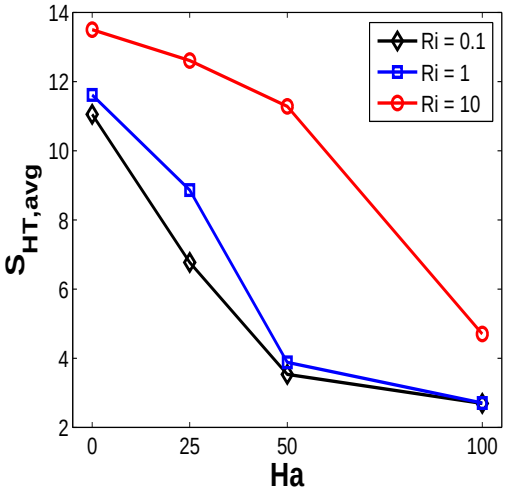

Figure 5.16: Variation of average entropy generation due to heat transfer as a function of Hartmann number for different Richardson numbers.

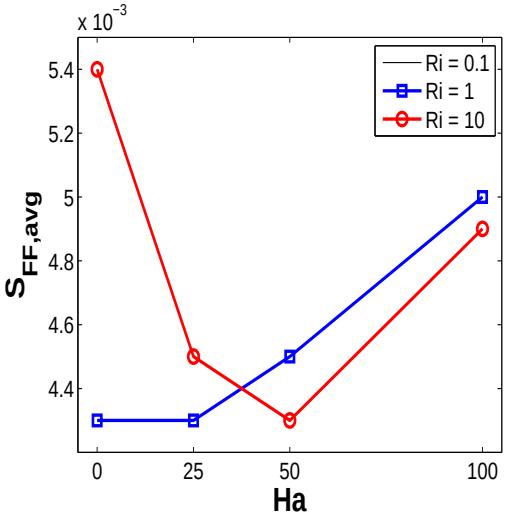

Figure 5.17: Variation of average entropy generation due to fluid friction as a function of Hartmann number for different Richardson numbers.

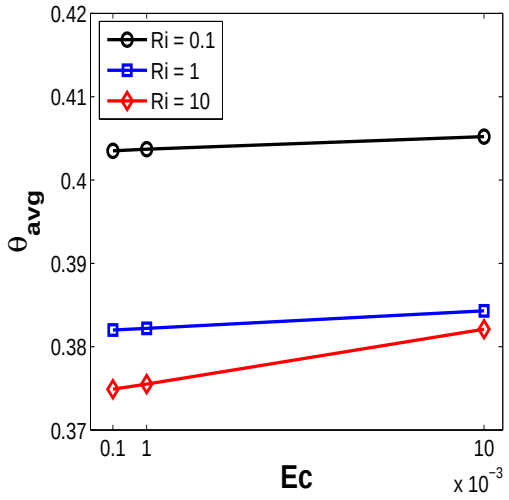

Figure 5.18: Variation of average temperature as a function of Eckert number for different Richardson numbers.

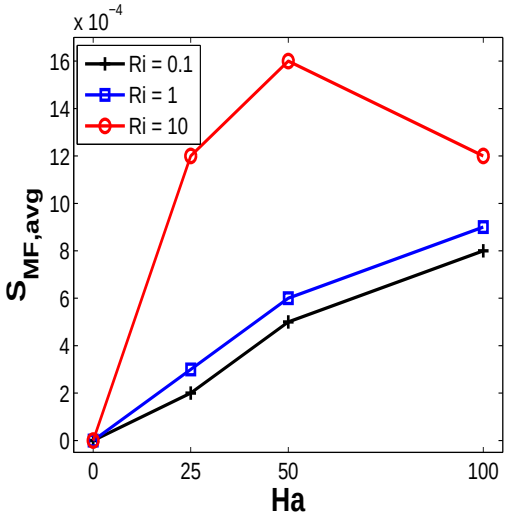

Figure 5.19: Variation of average entropy generation due to magnetic field as a function of Hartmann number for different Richardson numbers.

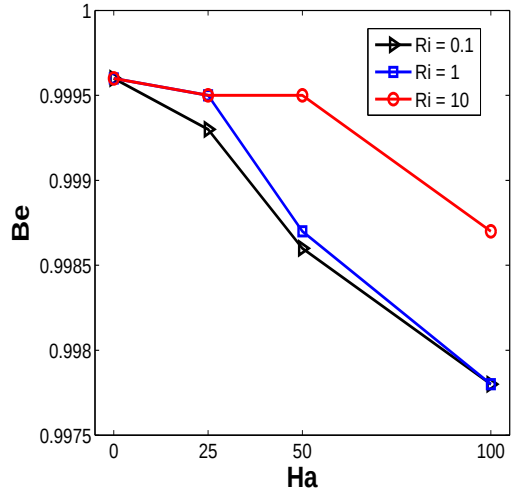

Figure 5.20: Variation of Bejan number as a function of Hartmann number for different Richardson numbers.

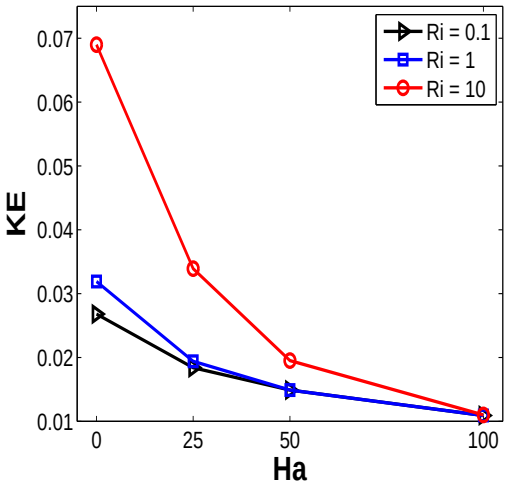

Figure 5.21: Variation of kinetic energy as a function of Hartmann number for different Richardson numbers.

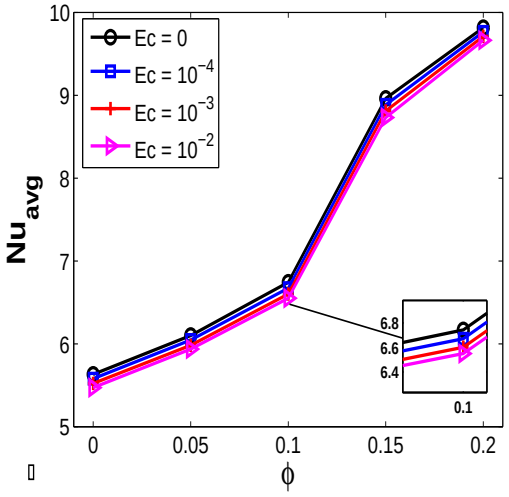

Figure 5.22: Variation of average Nusselt number as a function of nanoparticles volume fraction.

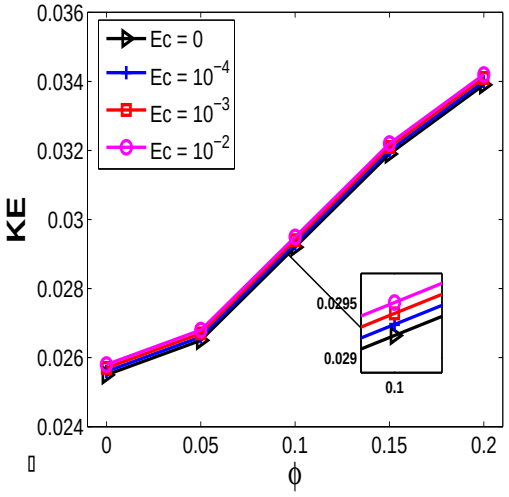

Figure 5.23: Variation of kinetic energy as a function of nanoparticles volume fraction.

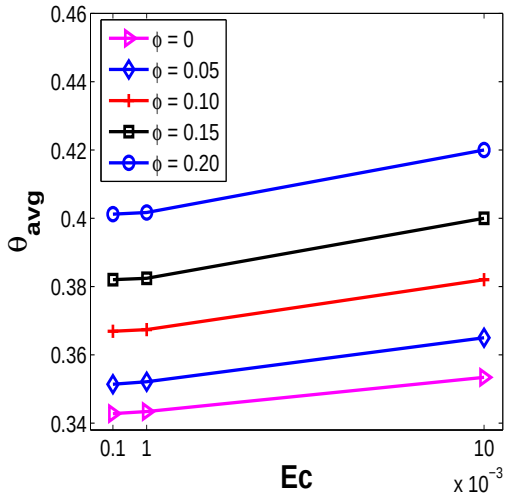

Figure 5.24: Variation of average temperature as a function of Eckert number.

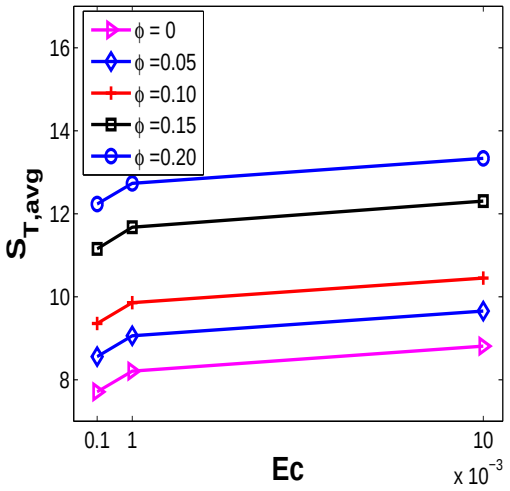

Figure 5.25: Variation of average total entropy generation as a function of Eckert number.

5.5 Closing Remarks

In the present analysis, the mixed convection in alumina-water nanofluid filled lid driven square cavity with an isothermally heated square blockage inside with magnetic field effect has been examined. The top moving wall and buoyancy force are responsible for motion of fluid. The Galerkin finite element method is used for

space discretization and the Crank-Nicolson is utilized for the time discretization. Newton's method has been used to linearize the governing system of nonlinear equations and the Gaussian elimination method is applied to solve the linear subproblems. The computations have been performed to observe influence of pertinent parameters on the heat transfer, temperature distribution and the fluid flow. The main findings of this chapter can be given as follows.

1. The streamlines strength in the whole cavity declines and in the proximity of the bottom hot wall, the isotherms become less concentrated with an amplification in the Hartmann number.

2. A reduction in the average Nusselt number and an augmentation in the average entropy generation due to the heat transfer, average total entropy generation and average temperature have been observed with an increment in Eckert number.

3. An increase in average temperature in the cavity has been noticed with an augmentation in the Eckert number and magnetic field strength.

4. A decline in the average Nusselt number, average entropy generation due to the heat transfer, Bejan number and kinetic energy has been perceived with an increase in the magnetic field strength.

5. An increase in the average Nusselt number and kinetic energy has been examined with an increase in the nanoparticles volume fraction.

Chapter 6

MHD Mixed Convective Nanofluid Flow in a Porous Cavity

6.1 Introduction

This chapter examines the influence of non-linear thermal radiation and inclined magnetic field on the mixed convection in a square porous cavity. Here, the cavity is saturated with alumina–water nanofluid. The Darcy-Brinkman-Forchheimer model has been used to formulate governing differential equations. After transforming equations to dimensionless form, these are solved by utilizing the weighted residual Galerkin finite element method. Latest KKL model is employed for the evaluation of effective thermal conductivity and dynamic viscosity of nanofluid. The effect of pertinent parameters in specific ranges such as Richardson number ($0.01 \leq Ri \leq 100$), radiation parameter ($0 \leq Rd \leq 5$), temperature ratio parameter ($1.1 \leq Nr \leq 1.4$), inclined magnetic field parameter ($0° \leq \gamma \leq 90°$), Darcy number ($10^{-6} \leq Da \leq 10^{-3}$), porosity parameter ($0.2 \leq \epsilon \leq 0.8$) and volume fraction of solid particles ($0 \leq \phi \leq 0.04$) has been studied and presented in the form of streamlines, isotherms and plots. Moreover, kinetic energy and average

temperature have also been taken into account for better understanding the flow philosophy. It is found that the radiation parameter, temperature ratio parameter, Darcy number and porosity parameter augment the heat transfer, kinetic energy and average temperature while inclined magnetic field parameter in the selected aforementioned ranges declines the heat transfer due to the hot bottom wall. This study is organised in the following way. Section 6.2 illustrates problem configuration. Section 6.3 contains information about the space and time discretizations of the governing equations, the numerical method, code validation and grid independence test. Results based on the numerical simulation have been elaborated in Section 6.4. Finally, conclusion has been drawn in Section 6.5.

6.2 Problem Formulation

6.2.1 The Problem Configuration

The flow model under consideration (see Figure. 6.1) consists of two dimensional square porous cavity filled with alumina-water nanofluid. The bottom wall of the cavity is hot with dimensional temperature T_h and the top wall has been kept at cold temperature T_c while both of the vertical walls are adiabatic and moving with velocity V_w in opposite directions. Shear forces due to vertical moving walls and buoyancy forces due to the hot bottom wall are responsible for the fluid movement. The porous medium is considered to be homogenous and isotropic. Base fluid and nanoparticles are in thermal equilibrium and there exists no slip velocity between them. Fluid is assumed to be Newtonian and incompressible. The flow is designated as steady and laminar. Joule heating, viscous dissipation and internal heat generation are neglected in the energy equation. Thermo-physical properties (see Table 6.1) of water and alumina are invariant except for density that is evaluated through Boussinesq approximation.

Physical properties	H_2O	Al_2O_3
ρ (kg m^{-3})	997.1	3970
C_p (J kg^{-1}K^{-1})	4179	765
k (W m^{-1} K^{-1})	0.613	40
β (K^{-1})	21×10^{-5}	1.89×10^{-5}
$\sigma\,(\Omega m)^{-1}$	0.05	1×10^{-10}
d_s (nm)	-	47

Table 6.1: Thermo-physical properties of water and alumina.

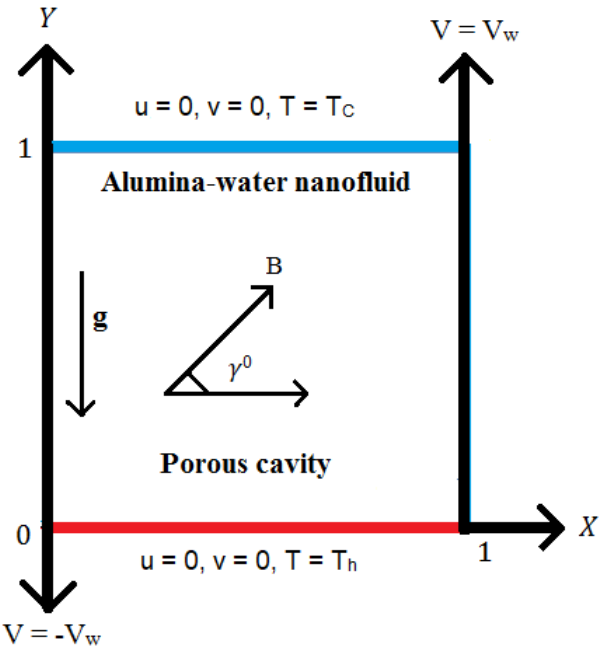

Figure 6.1: Schematic diagram of the physical model.

6.2.2 The Governing Equations

Governing equations of continuity, momentum and energy under the above-mentioned assumptions are given by

$$\begin{aligned}
\frac{\rho_{nf}}{\epsilon^2}\left(u\frac{\partial u}{\partial x} + v\frac{\partial u}{\partial y}\right) &= -\frac{\partial p}{\partial x} + \frac{\mu_{nf}}{\epsilon}\left(\frac{\partial^2 u}{\partial x^2} + \frac{\partial^2 u}{\partial y^2}\right) \\
&\quad + \sigma_{nf}B_0^2\left(v\sin\gamma\cos\gamma - u\sin^2\gamma\right) - \frac{\mu_{nf}}{K}u \\
&\quad - \frac{1.75\rho_{nf}}{\sqrt{150K}\epsilon^{\frac{3}{2}}}\left(\sqrt{u^2 + v^2}\right)u, \qquad (6.1) \\
\frac{\rho_{nf}}{\epsilon^2}\left(u\frac{\partial v}{\partial x} + v\frac{\partial v}{\partial y}\right) &= -\frac{\partial p}{\partial y} + \frac{\mu_{nf}}{\epsilon}\left(\frac{\partial^2 v}{\partial x^2} + \frac{\partial^2 v}{\partial y^2}\right) \\
&\quad + \sigma_{nf}B_0^2\left(u\sin\gamma\cos\gamma - v\cos^2\gamma\right) - \frac{\mu_{nf}}{K}v
\end{aligned}$$

$$+ \ (\rho\beta)_{nf} g(T - T_c) \ - \ \frac{1.75\rho_{nf}}{\sqrt{150K}\epsilon^{\frac{3}{2}}} \left(\sqrt{u^2 \ + \ v^2}\right) v, \tag{6.2}$$

$$\frac{\partial u}{\partial x} \ + \ \frac{\partial v}{\partial y} \ = \ 0, \tag{6.3}$$

$$u\frac{\partial T}{\partial x} \ + \ v\frac{\partial T}{\partial y} \ = \ \alpha_{nf}\left(\frac{\partial^2 T}{\partial x^2} \ + \ \frac{\partial^2 T}{\partial y^2}\right) \ + \ \left(\frac{\partial q_{rx}}{\partial x} \ + \ \frac{\partial q_{ry}}{\partial y}\right). \tag{6.4}$$

Applying Rosseland approximation [139] for the radiation and expanding T^4 as in Taylor series about T_c just like $T^4 \approx 4TT_c^3 - 3T_c^4$ and neglecting higher order terms, thermal radiation terms can be expressed by

$$q_{rx} = -\frac{4\sigma_*}{3a_R}\frac{\partial T^4}{\partial x} = -\frac{16\sigma_*}{3a_R}T^3\frac{\partial T}{\partial x}, \tag{6.5}$$

$$q_{ry} = -\frac{4\sigma_*}{3a_R}\frac{\partial T^4}{\partial y} = -\frac{16\sigma_*}{3a_R}T^3\frac{\partial T}{\partial y}. \tag{6.6}$$

The above Eqs. (6.5) and (6.6) are non-linear in T.

6.2.3 The Dimensionless Governing Equations

Following variables are utilized to transform the system into dimensionless form

$$X = \frac{x}{L}, \quad Y = \frac{y}{L}, \quad U = \frac{u}{V_w}, \quad V = \frac{v}{V_w}, \quad \theta = \frac{T - T_c}{T_h - T_c}, \quad P = \frac{p}{\rho_{nf}U_0^2}, \quad Da = \frac{K}{L^2},$$

$$Rd = \frac{4\sigma_* T_c^3}{a_R\alpha}, \quad Re = \frac{V_w L}{\nu_f}, \quad Gr = \frac{g\beta\Delta T L^3}{\nu_f^2}, \quad Pr = \frac{\nu_f}{\alpha_f}, \quad Ha = B_0\sqrt{\frac{\sigma_{nf}K}{\mu_{nf}}},$$

$$Ri = \frac{Gr}{Re^2}, \quad Nr = \frac{T_h}{T_c}.$$

The dimensionless governing equations are reduced as follows:

$$\begin{aligned}\frac{1}{\epsilon^2}\left(U\frac{\partial U}{\partial X} \ + \ V\frac{\partial U}{\partial Y}\right) \ = \ & -\frac{\partial P}{\partial X} \ + \ \frac{1}{\epsilon Re}\frac{\mu_{nf}}{\rho_{nf}\nu_f}\left(\frac{\partial^2 U}{\partial X^2} \ + \ \frac{\partial^2 U}{\partial Y^2}\right) \\ & + \frac{\rho_f}{\rho_{nf}}\frac{\sigma_{nf}}{\sigma_f}\frac{Ha^2}{Re}\left(V\sin\gamma\cos\gamma \ - \ U\sin^2\gamma\right) \\ & - \frac{\mu_{nf}}{\rho_{nf}\nu_f}\frac{1}{ReDa}U\end{aligned}$$

$$- \frac{1.75}{\sqrt{150Da}\epsilon^{\frac{3}{2}}}\left(\sqrt{U^2 + V^2}\right)U, \tag{6.7}$$

$$\begin{aligned}\frac{1}{\epsilon^2}\left(U\frac{\partial V}{\partial X} + V\frac{\partial V}{\partial Y}\right) &= -\frac{\partial P}{\partial Y} + \frac{1}{\epsilon Re}\frac{\mu_{nf}}{\rho_{nf}\nu_f}\left(\frac{\partial^2 V}{\partial X^2} + \frac{\partial^2 V}{\partial Y^2}\right) \\ &+ Ri\frac{\rho_f}{\rho_{nf}}\left(1-\phi+\frac{\rho_s\beta_s}{\rho_f\beta_f}\phi\right)\theta \\ &+ \frac{\rho_f}{\rho_{nf}}\frac{\sigma_{nf}}{\sigma_f}\frac{Ha^2}{Re}\left(U\sin\gamma\cos\gamma - V\cos^2\gamma\right) \\ &- \frac{\mu_{nf}}{\rho_{nf}\nu_f}\frac{1}{ReDa}V \\ &- \frac{1.75}{\sqrt{150Da}\epsilon^{\frac{3}{2}}}\left(\sqrt{U^2 + V^2}\right)V,\end{aligned} \tag{6.8}$$

$$\frac{\partial U}{\partial X} + \frac{\partial V}{\partial Y} = 0, \tag{6.9}$$

$$\begin{aligned}U\frac{\partial \theta}{\partial X} + V\frac{\partial \theta}{\partial Y} &= \frac{1}{RePr}\frac{\alpha_{nf}}{\alpha_f}\frac{k_m}{k_{nf}}\left(\frac{\partial^2\theta}{\partial X^2} + \frac{\partial^2\theta}{\partial Y^2}\right) \\ &+ \frac{Rd}{RePr}\left((1 + (Nr - 1)\theta)^3\right)\left(\frac{\partial^2\theta}{\partial X^2} + \frac{\partial^2\theta}{\partial Y^2}\right).\end{aligned} \tag{6.10}$$

Associated with the problem, the boundary conditions are given by

At the top wall : $U = 0, \quad V = 0, \quad \theta = 0,$

At the bottom wall : $U = 0, \quad V = 0, \quad \theta = 1,$

At the left wall : $U = 0, \quad V = -1, \quad \dfrac{\partial\theta}{\partial X} = 0,$

At the right wall : $U = 0, \quad V = 1, \quad \dfrac{\partial\theta}{\partial X} = 0.$

6.2.4 The Effective Nanofluid Properties

The thermal diffusivity, effective density, coefficient of thermal expansion, specific heat and electrical conductivity of the nanofluid [20, 140] could be expressed as follows

$$\rho_{nf} = (1-\phi)\rho_f + \phi\rho_p, \tag{6.11}$$

$$\alpha_{nf} = \frac{k_{nf}}{(\rho C_p)_{nf}}, \tag{6.12}$$

$$(\rho C_p)_{nf} = (1-\phi)(\rho C_p)_f + \phi(\rho C_p)_p, \tag{6.13}$$

$$(\rho\beta)_{nf} = (1-\phi)(\rho\beta)_f + \phi(\rho\beta)_p, \tag{6.14}$$

$$\sigma_{nf} = \sigma_f \left[1 + \frac{3(\sigma-1)\phi}{(\sigma+2)-(\sigma-1)\phi}\right], \ \sigma = \frac{\sigma_p}{\sigma_f}. \tag{6.15}$$

The Brownian motion has considerable influence on the thermal conductivity of the nanofluid. Koo and Kleinstreuer [141] proposed the following model for effective thermal conductivity.

$$k_{static} = k_f \left[1 + \frac{3\,(k_p/k_f - 1)\,\phi}{(k_p/k_f + 2) - (k_p/k_f - 1)\,\phi}\right], \tag{6.16}$$

$$k_{eff} = k_{static} + k_{Brownian}, \tag{6.17}$$

where k_p and k_f are the thermal conductivities of solid nanosized particles and pure fluid, respectively, k_{static} is the static thermal conductivity based on Maxwell model [45] and $k_{Brownian}$ is the thermal conductivity proposed by KKL model and given by

$$k_{Brownian} = 5 \times 10^4 \phi \rho_f (C_p)_f \sqrt{\frac{\kappa_b T}{\rho_p d_p}}\, g'(T, \phi, d_p), \tag{6.18}$$

where empirical function g' for the Al_2O_3-water nanofluid can be given by

$$\begin{aligned} g'(T,\phi,d_p) = {} & (a_1 + a_2\ln(d_p) + a_3\ln(\phi) + a_4\ln(\phi)\ln(d_p) + a_5\ln(d_p)^2)\ln(T) \\ & + (a_6 + a_7\ln(d_p) + a_8\ln(\phi) + a_9\ln(d_p)\ln(\phi) + a_{10}\ln(d_p)^2). \end{aligned} \tag{6.19}$$

The coefficients $a_i (i = 1, 2, ..., 10)$ are tabulated in Table 6.2. Koo and Kleinstreuer [119] further proposed following model for the effective viscosity due to micromixing in suspensions.

$$\mu_{eff} = \mu_{static} + \mu_{Brownian} = \mu_{static} + \frac{k_{Brownian}}{k_f} \times \frac{\mu_f}{Pr_f}, \tag{6.20}$$

where $\mu_{static} = \mu_f/(1-\phi)^{2.5}$ is the viscosity of nanofluid, given by Brinkman [44]. Also, by incorporating the interfacial thermal resistence $R_f = 4 \times 10^{-8}\mathrm{m^2K/W}$,

the original k_p in Eq. (6.16) is replaced by $k_{p,eff}$ in the form

$$R_f + \frac{d_p}{k_p} = \frac{d_p}{k_{p,eff}}. \tag{6.21}$$

Effective heat capacity and effective thermal conductivity of the porous medium

Coefficient values	Al_2O_3-water
a_1	52.813488759
a_2	6.115637295
a_3	0.6955745084
a_4	0.041745555278
a_5	0.176919300241
a_6	-298.19819084
a_7	-34.532716906
a_8	-3.9225289283
a_9	-0.2354329626
a_{10}	-0.999063481

Table 6.2: The coefficient values of Al_2O_3-water nanofluid [22].

are calculated from the relations [71, 72] given by

$$(\rho C_p)_m = (1-\epsilon)(\rho C_p)_p + \epsilon(\rho C_p)_{nf}, \tag{6.22}$$

$$k_m = (1-\epsilon)k_p + \epsilon k_{nf}. \tag{6.23}$$

We used the glass fibers to simulate the porous medium [142, 143].

6.2.5 Calculation of the Nusselt number

Local and average Nusselt number at the hot bottom wall are given by

$$Nu = -\frac{k_{nf}}{k_f}\left(1 + RdNr^3\right)\left(\frac{\partial\theta}{\partial Y}\right)\Bigg|_{Y=0,1}, \tag{6.24}$$

$$Nu_{\text{avg}} = \int_0^1 Nu\ dX. \tag{6.25}$$

6.3 The Numerical Approach

6.3.1 The Spatial Discretization

The system of coupled non-linear partial dierential equations together with given boundary conditions have been discretized numerically by the finite element formulation. The numerical procedure used to solve the governing equations for the present work is based on the Galerkin weighted residual method in which we have used the higher order Stokes element Q_2/P_1^{disc}, where Q_2 element is utilized for the velocity and temperature and P_1^{disc} element is used for the pressure (see 2.5 for detail). The variational or weak form of the governing Eqs. (6.7) - (6.10) is given in the following:

$$
\begin{aligned}
&\frac{1}{\epsilon^2}\int_\Omega \left(U\frac{\partial U}{\partial X} + V\frac{\partial U}{\partial Y}\right) w \, d\Omega = -\int_\Omega \frac{\partial P}{\partial X} w \, d\Omega \\
&+ \frac{1}{\epsilon Re}\frac{\mu_{nf}}{\rho_{nf}\nu_f}\int_\Omega \left(\frac{\partial^2 U}{\partial X^2} + \frac{\partial^2 U}{\partial Y^2}\right) w \, d\Omega \\
&+ \frac{\rho_f}{\rho_{nf}}\frac{\sigma_{nf}}{\sigma_f}\frac{Ha^2}{Re}\left(\sin\gamma\cos\gamma \int_\Omega Vw \, d\Omega - \sin^2\gamma\int_\Omega Uw \, d\Omega\right) \\
&- \frac{\mu_{nf}}{\rho_{nf}\nu_f}\frac{1}{ReDa}\int_\Omega U \, w \, d\Omega \\
&- \frac{1.75}{\sqrt{150Da}\epsilon^{\frac{3}{2}}}\int_\Omega \left(\sqrt{U^2 + V^2}\right) Uw \, d\Omega,
\end{aligned} \tag{6.26}
$$

$$
\begin{aligned}
&\frac{1}{\epsilon^2}\int_\Omega \left(U\frac{\partial V}{\partial X} + V\frac{\partial V}{\partial Y}\right) w \, d\Omega = -\int_\Omega \frac{\partial P}{\partial Y} w \, d\Omega \\
&+ \frac{1}{\epsilon Re}\frac{\mu_{nf}}{\rho_{nf}\nu_f}\int_\Omega \left(\frac{\partial^2 V}{\partial X^2} + \frac{\partial^2 V}{\partial Y^2}\right) w \, d\Omega \\
&+ Ri\frac{\rho_f}{\rho_{nf}}\left(1 - \phi + \frac{\rho_s\beta_s}{\rho_f\beta_f}\phi\right)\int_\Omega \theta \, w \, d\Omega \\
&+ \frac{\rho_f}{\rho_{nf}}\frac{\sigma_{nf}}{\sigma_f}\frac{Ha^2}{Re}\left(\sin\gamma\cos\gamma \int_\Omega Uw \, d\Omega - \cos^2\gamma\int_\Omega Vw \, d\Omega\right) \\
&- \frac{\mu_{nf}}{\rho_{nf}\nu_f}\frac{1}{ReDa}\int_\Omega V \, w \, d\Omega \\
&- \frac{1.75}{\sqrt{150Da}\epsilon^{\frac{3}{2}}}\int_\Omega \left(\sqrt{U^2 + V^2}\right) Vw \, d\Omega,
\end{aligned} \tag{6.27}
$$

$$
\int_\Omega \left(\frac{\partial U}{\partial X} + \frac{\partial V}{\partial Y}\right) q \, d\Omega = 0, \tag{6.28}
$$

$$\int_\Omega \left(U\frac{\partial\theta}{\partial X} + V\frac{\partial\theta}{\partial Y} \right) w \, d\Omega = \frac{1}{RePr}\frac{\alpha_{nf}}{\alpha_f}\frac{k_m}{k_{nf}} \int_\Omega \left(\frac{\partial^2\theta}{\partial X^2} + \frac{\partial^2\theta}{\partial Y^2} \right) w \, d\Omega$$
$$+ \frac{Rd}{RePr}\int_\Omega \left((1 + (Nr - 1)\,\theta)^3 \right) \left(\frac{\partial^2\theta}{\partial X^2} + \frac{\partial^2\theta}{\partial Y^2} \right) w \, d\Omega \quad . \tag{6.29}$$

Now, the infinite dimensional trial spaces U, V, θ and P are approximated by U_h, V_h, θ_h and P_h, respectively. Moreover, the infinite dimensional test spaces W and Q are approximated by the finite dimensional test spaces W_h and Q_h, respectively, in such a way that

$$w_h \in W_h \subset H^1(\Omega) = \left\{ s : \Omega \to \mathbb{R} : \int_\Omega |s(x)|^2 dx < \infty, \int_\Omega |s'(x)|^2 dx < \infty \right\},$$
$$q_h \in Q_h \subset L_2(\Omega) = \left\{ g : \Omega \to \mathbb{R} : \int_\Omega |g(x)|^2 dx < \infty \right\}.$$

After the finite dimensional approximation the Eqs. (6.26) - (6.29) takes the form, given as follows:

$$\begin{aligned}
&\frac{1}{\epsilon^2}\int_\Omega \left(U_h\frac{\partial U_h}{\partial X} + V_h\frac{\partial U_h}{\partial Y} \right) w_h \, d\Omega = -\int_\Omega \frac{\partial P_h}{\partial X} w_h \, d\Omega \\
&+ \frac{1}{\epsilon Re}\frac{\mu_{nf}}{\rho_{nf}\nu_f}\int_\Omega \left(\frac{\partial^2 U_h}{\partial X^2} + \frac{\partial^2 U_h}{\partial Y^2} \right) w_h \, d\Omega \\
&+ \frac{\rho_f}{\rho_{nf}}\frac{\sigma_{nf}}{\sigma_f}\frac{Ha^2}{Re}\left(\sin\gamma\cos\gamma \int_\Omega V_h w_h \, d\Omega - \sin^2\gamma \int_\Omega U_h w_h \, d\Omega \right) \\
&- \frac{\mu_{nf}}{\rho_{nf}\nu_f}\frac{1}{ReDa}\int_\Omega U_h \, w_h \, d\Omega \\
&- \frac{1.75}{\sqrt{150Da}\epsilon^{\frac{3}{2}}}\int_\Omega \left(\sqrt{U_h^2 + V_h^2} \right) U_h w_h \, d\Omega, \\
&\frac{1}{\epsilon^2}\int_\Omega \left(U_h\frac{\partial V_h}{\partial X} + V_h\frac{\partial V_h}{\partial Y} \right) w_h \, d\Omega = -\int_\Omega \frac{\partial P_h}{\partial Y} w_h \, d\Omega \\
&+ \frac{1}{\epsilon Re}\frac{\mu_{nf}}{\rho_{nf}\nu_f}\int_\Omega \left(\frac{\partial^2 V_h}{\partial X^2} + \frac{\partial^2 V_h}{\partial Y^2} \right) w_h \, d\Omega \\
&+ Ri\frac{\rho_f}{\rho_{nf}}\left(1 - \phi + \frac{\rho_s\beta_s}{\rho_f\beta_f}\phi \right)\int_\Omega \theta_h \, w_h \, d\Omega \\
&+ \frac{\rho_f}{\rho_{nf}}\frac{\sigma_{nf}}{\sigma_f}\frac{Ha^2}{Re}\left(\sin\gamma\cos\gamma \int_\Omega U_h w_h \, d\Omega - \cos^2\gamma \int_\Omega V_h w_h \, d\Omega \right) \\
&- \frac{\mu_{nf}}{\rho_{nf}\nu_f}\frac{1}{ReDa}\int_\Omega V_h \, w_h \, d\Omega
\end{aligned} \tag{6.30}$$

$$- \frac{1.75}{\sqrt{150Da}\epsilon^{\frac{3}{2}}} \int_{\Omega} \left(\sqrt{U_h^2 + V_h^2} \right) V_h w_h \, d\Omega, \tag{6.31}$$

$$\int_{\Omega} \left(\frac{\partial U_h}{\partial X} + \frac{\partial V_h}{\partial Y} \right) q_h \, d\Omega = 0, \tag{6.32}$$

$$\int_{\Omega} \left(U_h \frac{\partial \theta_h}{\partial X} + V_h \frac{\partial \theta_h}{\partial Y} \right) w_h \, d\Omega = \frac{1}{RePr} \frac{\alpha_{nf}}{\alpha_f} \frac{k_m}{k_{nf}} \int_{\Omega} \left(\frac{\partial^2 \theta_h}{\partial X^2} + \frac{\partial^2 \theta_h}{\partial Y^2} \right) w_h \, d\Omega + \frac{Rd}{RePr} \int_{\Omega} \left((1 + (Nr - 1)\theta_h)^3 \right) \left(\frac{\partial^2 \theta_h}{\partial X^2} + \frac{\partial^2 \theta_h}{\partial Y^2} \right) w_h \, d\Omega \; . \tag{6.33}$$

Using the finite element approximation $U_h(X,Y) = \sum_{j=1}^{N} U_j \xi_j(X,Y)$, $V_h(X,Y) = \sum_{j=1}^{N} V_j \xi_j(X,Y)$, $\theta_h(X,Y) = \sum_{j=1}^{N} \theta_j \xi_j(X,Y)$ and $P_h(X,Y) = \sum_{j=1}^{K} P_j \eta_j(X,Y)$ are the trial functions. Similarly $w_h = \sum_{i=1}^{N} w_i \, \xi_i$ and $q_h = \sum_{i=1}^{K} q_i \, \eta_i$ are the test functions. By the Galerkin finite element model for a typical element Ω_e, the Eqs. (6.30) - (6.33) are transformed into the following system:

$$\begin{aligned}
&\frac{1}{\epsilon^2} U_j \int_{\Omega_e} \left(\overline{U} \xi_i \frac{\partial \xi_j}{\partial X} + \overline{V} \xi_i \frac{\partial \xi_j}{\partial Y} \right) d\Omega_e = -P_j \int_{\Omega_e} \eta_j \frac{\partial \xi_i}{\partial X} \, d\Omega_e \\
&+ \frac{1}{\epsilon Re} \frac{\mu_{nf}}{\rho_{nf} \nu_f} U_j \int_{\Omega_e} \left(\frac{\partial \xi_j}{\partial X} \frac{\partial \xi_i}{\partial X} + \frac{\partial \xi_j}{\partial Y} \frac{\partial \xi_i}{\partial Y} \right) d\Omega_e \\
&+ \frac{\rho_f}{\rho_{nf}} \frac{\sigma_{nf}}{\sigma_f} \frac{Ha^2}{Re} \left(\sin\gamma \cos\gamma V_j \int_{\Omega_e} \xi_j \xi_i d\Omega_e - \sin^2\gamma U_j \int_{\Omega_e} \xi_j \xi_i d\Omega_e \right) \\
&- \frac{\mu_{nf}}{\rho_{nf} \nu_f} \frac{1}{ReDa} U_j \int_{\Omega_e} \xi_j \xi_i \, d\Omega_e \\
&- \frac{1.75}{\sqrt{150Da}\epsilon^{\frac{3}{2}}} U_j \int_{\Omega_e} \left(\sqrt{\overline{U} \, \overline{U} + \overline{V} \, \overline{V}} \right) \xi_j \xi_i \, d\Omega_e,
\end{aligned} \tag{6.34}$$

$$\begin{aligned}
&\frac{1}{\epsilon^2} V_j \int_{\Omega_e} \left(\overline{U} \xi_i \frac{\partial \xi_j}{\partial X} + \overline{V} \xi_i \frac{\partial \xi_j}{\partial Y} \right) d\Omega_e = -P_j \int_{\Omega_e} \eta_j \left(\frac{\partial \xi_i}{\partial Y} \right) d\Omega_e \\
&+ \frac{1}{\epsilon Re} \frac{\mu_{nf}}{\rho_{nf} \nu_f} V_j \int_{\Omega_e} \left(\frac{\partial \xi_j}{\partial X} \frac{\partial \xi_i}{\partial X} + \frac{\partial \xi_j}{\partial Y} \frac{\partial \xi_i}{\partial Y} \right) d\Omega_e \\
&+ Ri \frac{\rho_f}{\rho_{nf}} \left(1 - \phi + \frac{\rho_s \beta_s}{\rho_f \beta_f} \phi \right) \theta_j \int_{\Omega_e} \xi_j \xi_i d\Omega_e \\
&+ \frac{\rho_f}{\rho_{nf}} \frac{\sigma_{nf}}{\sigma_f} \frac{Ha^2}{Re} \left(\sin\gamma \cos\gamma U_j \int_{\Omega_e} \xi_j \xi_i d\Omega_e - \sin^2\gamma V_j \int_{\Omega_e} \xi_j \xi_i d\Omega_e \right) \\
&- \frac{\mu_{nf}}{\rho_{nf} \nu_f} \frac{1}{ReDa} V_j \int_{\Omega_e} \xi_j \xi_i d\Omega_e \\
&- \frac{1.75}{\sqrt{150Da}\epsilon^{\frac{3}{2}}} V_j \int_{\Omega_e} \left(\sqrt{\overline{U} \, \overline{U} + \overline{V} \, \overline{V}} \right) \xi_j \xi_i \, d\Omega_e,
\end{aligned} \tag{6.35}$$

$$U_j \int_{\Omega_e} \frac{\partial \xi_j}{\partial X} \eta_i \, d\Omega_e + V_j \int_{\Omega_e} \frac{\partial \xi_j}{\partial Y} \eta_i \, d\Omega_e = 0, \tag{6.36}$$

$$\begin{aligned}
&\theta_j \int_{\Omega_e} \left(\overline{U} \xi_i \frac{\partial \xi_j}{\partial X} + \overline{V} \xi_i \frac{\partial \xi_j}{\partial Y} \right) d\Omega_e \\
&= \frac{1}{RePr} \frac{\alpha_{nf}}{\alpha_f} \frac{k_m}{k_{nf}} \theta_j \int_{\Omega_e} \left(\frac{\partial \xi_j}{\partial X} \frac{\partial \xi_i}{\partial X} + \frac{\partial \xi_j}{\partial Y} \frac{\partial \xi_i}{\partial Y} \right) d\Omega_e \\
&+ \frac{Rd}{RePr} \theta_j \int_{\Omega_e} \left(1 + (Nr - 1)(\overline{\theta}) \right)^3 \left(\frac{\partial \xi_j}{\partial X} \frac{\partial \xi_i}{\partial X} + \frac{\partial \xi_j}{\partial Y} \frac{\partial \xi_i}{\partial Y} \right) d\Omega_e.
\end{aligned} \tag{6.37}$$

The final system can be expressed in the following comprehensive form

$$[\mathbf{K^e}][\mathbf{u^e}] = \{\mathbf{F^e}\}, \tag{6.38}$$

$$\underbrace{\begin{bmatrix} [K_{ji}^{11}] & [K_{ji}^{12}] & [K_{ji}^{13}] & [K_{ji}^{14}] \\ [K_{ji}^{21}] & [K_{ji}^{22}] & [K_{ji}^{23}] & [K_{ji}^{24}] \\ [K_{ji}^{31}] & [K_{ji}^{32}] & [K_{ji}^{33}] & [K_{ji}^{34}] \\ [K_{ji}^{41}] & [K_{ji}^{42}] & [K_{ji}^{43}] & [K_{ji}^{44}] \end{bmatrix}}_{\mathbf{K^e}} \underbrace{\begin{bmatrix} \{\underline{U}\} \\ \{\underline{V}\} \\ \{\underline{P}\} \\ \{\underline{\theta}\} \end{bmatrix}}_{\mathbf{u^e}} = \underbrace{\begin{bmatrix} \{\underline{F^1}\} \\ \{\underline{F^2}\} \\ \{\underline{F^3}\} \\ \{\underline{F^4}\} \end{bmatrix}}_{\mathbf{F^e}}, \tag{6.39}$$

where $\mathbf{K^e}$, $\mathbf{u^e}$ and $\mathbf{F^e}$ are said to be the stiffness block matrix, the block solution vector and the right hand side block vector at an element level, respectively. For the sake of brevity, the boundary integral is also included in $\mathbf{F^e}$. In stiffness block matrix,

$$\begin{aligned}
K_{ji}^{11} &= \frac{1}{\epsilon Re} \frac{\rho_f}{\rho_{nf}} \frac{1}{(1-\phi)^{2.5}} \int_{\Omega_e} \left(\frac{\partial \xi_j}{\partial X} \frac{\partial \xi_i}{\partial X} + \frac{\partial \xi_j}{\partial Y} \frac{\partial \xi_i}{\partial Y} \right) d\Omega_e + \frac{\mu_{nf}}{\nu_{nf} \rho_{nf}} \frac{1}{ReDa} \int_{\Omega_e} \xi_j \xi_i d\Omega_e \\
&\quad + \frac{1}{\epsilon^2} \int_{\Omega_e} \left(\overline{U} \xi_i \frac{\partial \xi_j}{\partial X} + \overline{V} \xi_i \frac{\partial \xi_j}{\partial Y} \right) d\Omega_e + \frac{1.75}{\sqrt{150 Da} \epsilon^{\frac{3}{2}}} \int_{\Omega_e} \left(\sqrt{\overline{U} \ \overline{U} + \overline{V} \ \overline{V}} \right) \xi_j \xi_i d\Omega_e \quad , \\
K_{ji}^{22} &= \frac{1}{\epsilon Re} \frac{\rho_f}{\rho_{nf}} \frac{1}{(1-\phi)^{2.5}} \int_{\Omega_e} \left(\frac{\partial \xi_j}{\partial X} \frac{\partial \xi_i}{\partial X} + \frac{\partial \xi_j}{\partial Y} \frac{\partial \xi_i}{\partial Y} \right) d\Omega_e + \frac{\mu_{nf}}{\nu_{nf} \rho_{nf}} \frac{1}{ReDa} \int_{\Omega_e} \xi_j \xi_i d\Omega_e \\
&\quad + \frac{1}{\epsilon^2} \int_{\Omega_e} \left(\overline{U} \xi_i \frac{\partial \xi_j}{\partial X} + \overline{V} \xi_i \frac{\partial \xi_j}{\partial Y} \right) d\Omega_e + \frac{1.75}{\sqrt{150 Da} \epsilon^{\frac{3}{2}}} \int_{\Omega_e} \left(\sqrt{\overline{U} \ \overline{U} + \overline{V} \ \overline{V}} \right) \xi_j \xi_i d\Omega_e, \\
K_{ji}^{12} &= -\frac{\rho_f}{\rho_{nf}} \frac{\sigma_{nf}}{\sigma_f} \frac{Ha^2}{Re} \left(\sin\gamma \cos\gamma \int_{\Omega_e} \xi_j \xi_i d\Omega_e \right), \\
K_{ji}^{21} &= -\frac{\rho_f}{\rho_{nf}} \frac{\sigma_{nf}}{\sigma_f} \frac{Ha^2}{Re} \left(\sin\gamma \cos\gamma \int_{\Omega_e} \xi_j \xi_i d\Omega_e \right), \\
K_{ji}^{44} &= \frac{\alpha_{nf}}{\alpha_f} \frac{1}{RePr} \int_{\Omega_e} \left(\frac{\partial \xi_j}{\partial X} \frac{\partial \xi_i}{\partial X} + \frac{\partial \xi_j}{\partial Y} \frac{\partial \xi_i}{\partial Y} \right) d\Omega_e + \int_{\Omega_e} \left(\overline{U} \xi_i \frac{\partial \xi_j}{\partial X} + \overline{V} \xi_i \frac{\partial \xi_j}{\partial Y} \right) d\Omega_e \quad ,
\end{aligned}$$

$$+\frac{Rd}{RePr}\int_{\Omega_e}\left(1+(Nr-1)(\overline{\theta})\right)^3\left(\frac{\partial\xi_j}{\partial X}\frac{\partial\xi_i}{\partial X}+\frac{\partial\xi_j}{\partial Y}\frac{\partial\xi_i}{\partial Y}\right)\,d\Omega_e,$$

$$K_{ji}^{24}=-Ri\frac{\rho_f}{\rho_{nf}}\left(1-\phi+\frac{\rho_s\beta_s\phi}{\rho_f\beta_f}\right)\int_{\Omega_e}\xi_j\xi_i\,d\Omega_e,$$

$$K_{ji}^{13}=-\int_{\Omega_e}\eta_j\frac{\partial\xi_i}{\partial X}d\Omega_e \quad ,$$

$$K_{ji}^{23}=-\int_{\Omega_e}\eta_j\frac{\partial\xi_i}{\partial Y}d\Omega_e \quad ,$$

$$K_{ji}^{31}=\int_{\Omega_e}\frac{\partial\xi_j}{\partial X}\eta_i d\Omega_e \quad ,$$

$$K_{ji}^{32}=\int_{\Omega_e}\frac{\partial\xi_j}{\partial Y}\eta_i d\Omega_e \quad ,$$

$$K_{ji}^{14}=K_{ji}^{33}=K_{ji}^{34}=K_{ji}^{41}=K_{ji}^{42}=K_{ji}^{43}=0,$$

$$\overline{U}=\sum_{j=1}^{N}U_j\xi_j,\ \overline{V}=\sum_{j=1}^{N}V_j\xi_j \text{ and } \overline{\theta}=\sum_{j=1}^{N}\theta_j\xi_j.$$

We have utilized Q_2/P_1^{disc} for space discretization (see 2.5 for detail). After discretization in space, we obtain an algebraic system of nonlinear algebraic equations. Integration regarding each term of these equations is performed by Gaussian quadrature method. Then implementation of boundary conditions is carried out and linear algebraic equations are obtained from nonlinear equations utilizing iterative Newton method. Some tolerance value is prescribed to see the optimised minimum difference of the current values of the variables to the previous iteration values by achieving the convergence of the solution of an iterative scheme. In other words, the adopted criterion to stop the iterative scheme could be given as follows

$$\left|\frac{\Gamma^{n+1}-\Gamma^n}{\Gamma^{n+1}}\right|\leq 10^{-6}, \tag{6.40}$$

where U, V, P or θ are denoted by a general variable Γ. Superscript n represents the iteration number in the above expression. Finally, these linear equations are computed by the Gaussian elimination method.

6.3.2 Code Validation and Grid Independence Test

Code validation has been performed for free convection results published in the literature and given in Table 3.4 of chapter 3, for various computed variables. Code validation has also been presented in Table 3.3 for mixed convection flow in the section 3.3.2 of Chapter 3 and the results have an excellent agreement for both of the cases. Code has also been validated graphically with that investigated by Moumni *et al.* [144] as shown in Fig. 6.2. Grid independent study is executed by considering the uniform grids at different computation levels for average Nusselt number with $Re = 100, Ri = 1$ and $Ri = 10, \phi = 0.04, \gamma = 0°, \epsilon = 0.6, Rd = 1, Ha = 25, Da = 0.1, Nr = 1.1$. First, coarsest grid containing one element at level $\ell = 1$ is considered, then level $\ell = \ell + 1$ is obtained by dividing each element into four new elements by joining the opposite midpoints. Table 6.3 suggests that average Nusselt number values for mesh level $\ell = 9$ and $\ell = 10$ are almost the same. It indicates that further increase in mesh level merely boosts computational cost and there will be no significant effect on results. Therefore, all the simulations have been carried out at mesh level $\ell = 9$.

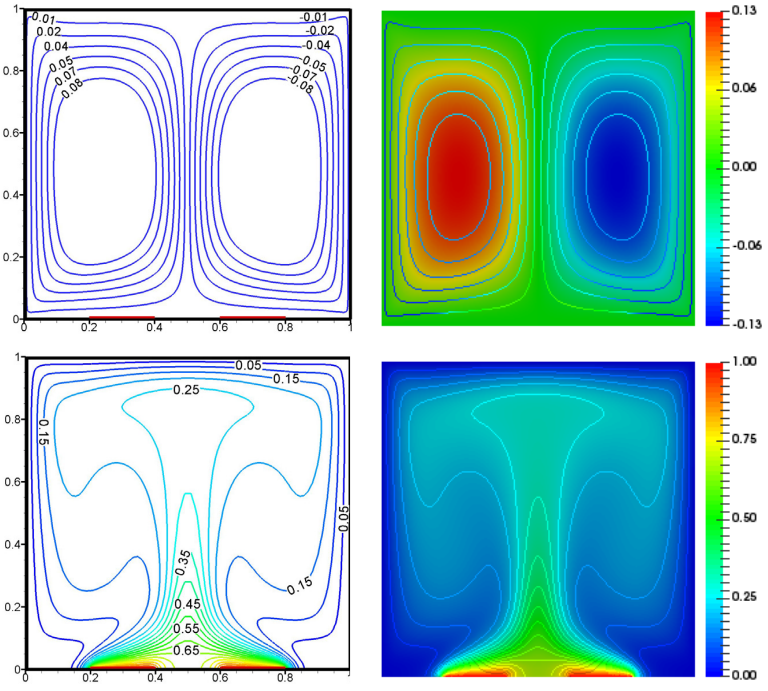

Figure 6.2: Code validation of streamlines (above row) and isotherms (bottom row) contours of present solver (right column) to that of Moumni *et al.* [144] (left column) for $Re = 50$, $Ri = 20$ and $\phi = 0.2$.

ℓ	#EL	#DOFs	$Nu_{\text{avg}}(Ri = 1)$	$Nu_{\text{avg}}(Ri = 10)$
4	64	1059	4.959023	8.079592
5	256	4035	6.382236	9.232417
6	1024	15747	5.988722	8.418373
7	4096	62211	5.750869	7.838208
8	16384	247299	5.379401	7.285173
9	65536	986115	5.181349	6.979336
10	262144	3938307	5.116674	6.918256

Table 6.3: Results of grid independence test for alumina-water nanofluid.

6.4 Results and Discussion

Numerical simulation has been accomplished on mixed convective alumina-water nanofluid filled porous square cavity considering the effect of non-linear thermal radiation and inclined magnetic field. In the whole study, considered standard parameters are $Re = 100, Ri = 1, Ha = 25, \phi = 0.04, \gamma = 0°, Rd = 1, Nr = 1.1, Da = 10^{-3}, \epsilon = 0.6$ unless mentioned, otherwise.

Effect of radiation parameter on streamline maps for $Ri = 0.01, 1$ and 100 has been demonstrated by Figure 6.3. Streamlines show almost the same pattern for small Richardson numbers, i.e., $Ri = 0.01$ and $Ri = 1$, two weak rotating cells along vertical walls are observed in these cases. Increasing the Richardson number up to $Ri = 100$, deeper flow activity in the cavity is induced due to dominant buoyancy forces which carries more energy from the hot bottom wall, thus causing significant changes in flow behavior. When radiation parameter is gradually increased from $Rd = 0$ to $Rd = 5$, maximum absolute stream function value increases that is more pronounced for the case of $Ri = 100$. In this situation, weak rotating vortices eventually coalesce into a single vortex in the middle of the cavity indicating higher fluid velocity in the cavity.

Impact of radiation parameter on isotherm maps for $Ri = 0.01, 1$ and 100 has been portrayed by Figure 6.4. Isotherms show nearly the same behavior for small

Richardson numbers. Initially, for low radiation parameter, isotherms with large magnitude occur in the right bottom and lines with small values exist in the top left corner of the cavity. Isotherms with intermediate values seem to travel diagonally from left bottom to top right vertex of the cavity. With an increase in the radiation parameter up to $Rd = 5$, isothermal lines are distributed uniformly that indicates dominance of conduction in the cavity.

Influence of Darcy number on streamline contours for $Ri = 0.01, 1$ and 100 has been elaborated by Figure 6.5. Initially, for $Da = 10^{-6}$, $Ri = 0.01$ and $Ri = 1$, two parabolic shaped rotating eddies appeared near the vertical adiabatic walls due to their movement in the opposite direction. An increase in Darcy number up to 10^{-3} causes in reduction in the resistance of fluid friction that results in the form of higher fluid velocity ($\psi_{max} = 0.0034$) in the cavity. Moreover, for the case of $Ri = 100$ and low Darcy numbers, two weak rotating vortices near the vertical walls appeared that are eventually combine into a central main vertex in the middle of the cavity, with an increase in Darcy number up to $Da = 10^{-3}$. This indicates an increase in fluid velocity due to decline in fluid friction resistance. This fact is also evident from maximum stream function values, i.e., $\psi_{max} = 0.0150$.

Impact of Darcy number on isotherm contours for $Ri = 0.01, 1$ and 100 has been manifested by Figure 6.6. Isotherm sketches appear to be almost the same for $Ri = 0.01$ and $Ri = 1$ whereas significant variation has been observed for $Ri = 100$. For $Da = 10^{-6}$, $Ri = 0.01$ and $Ri = 1$, isotherms are nearly parallel to hot bottom and top cold horizontal walls that are uniformly distributed indicating conduction in the cavity. Increasing Da, gradual slight variation has been noticed by transforming conduction to convection flow regime for low Richardson numbers. But for $Ri = 100$ and $Da = 10^{-3}$, thin thermal boundary layer is seen along the bottom hot and top cold walls. In this case, isotherms in the vicinity of adiabatic vertical walls become almost parallel to the walls.

Effect of porosity parameter on streamline and isotherm maps for $Ri = 0.01$, 1, 100

has been shown by Figures 6.7 and 6.8. As long as streamlines are concerned, for $Ri = 0.01$,$Ri = 1$ and $\epsilon = 0.2$, initially, two weaker eddies along opposite vertical adiabatic walls appear. As porosity parameter increases, strength of these eddies starts increasing slightly and becomes maximum for $\epsilon = 0.8$ that is also evident from maximum stream function value, $\psi_{max} = 0.0183$. Significant growth in maximum stream function value moves from low value of porosity to high porosity value. Slight variation in isotherm patterns is observed for $Ri = 0.01$ and $Ri = 1$ for fixed value of porosity parameter but significant changes occur for $Ri = 100$. Increase in porosity gradually converts conduction to convection flow behavior.

Average Nusselt number is a decreasing function of magnetic field inclination angle as illustrated by Figure 6.9. Moreover, nanofluid with $\phi = 0.04$ has the capability to transfer more heat in the cavity as compared to base fluid with $\phi = 0$. Effect of radiation parameter on average Nusselt number has been shown in Figure 6.10 and observed that heat transfer enhances with an increase in radiation parameter that is more highlighted for $Ri = 10$ and ($\phi = 0.04$). As a consequence of non-linear thermal radiation, an emerging control temperature ratio parameter Nr arises that increases heat transfer due to hot bottom wall as portrayed by Figure 6.11. Darcy number relates directly to the permeability of porous medium. Higher Darcy number penetrates powerful penetration that results in the form of higher heat transfer rate. This is also evident from Figures 6.12 and 6.13 that average Nusselt number is an increasing functions of Darcy number and porosity parameter and this increment is more pronounced for the case of nanofluid with $\phi = 0.04$. This enhancement in heat transfer becomes more pronounced for free convective flow regime ($Ri = 10$). Kinetic energy slightly rises with magnetic field inclinaton angle for small Richardson number but interestingly it decreases for $Ri = 10$ as exhibited by Figure 6.14. From Figure 6.15, kinetic energy is an increasing function of radiation parameter for free convection dominated regime ($Ri = 10$) and for pure fluid ($\phi = 0$) whereas kinetic energy is almost constant for mixed and forced convection flows. Kinetic energy augments with porosity parameter and Darcy number as shown by Figures 6.16 and 6.17, respectively.

The plots for $Ri = 0.01$ and $Ri = 1$ overlap each other to show the same behavior. Furthermore, it is witnessed from mentioned sketches that kinetic energy has greater value at higher Darcy number ($Da = 0.001$) due to less contribution from non-linear inertial drag in the momentum equations.

Influence of different physical parameters on average temperature has been presented in Figures 6.18-6.21. Average temperature in the cavity declines for forced convection ($Ri = 0.01$) and mixed convection ($Ri = 1$) regimes with magnetic field inclination angle whereas interestingly, it slightly increases for free convective flows ($Ri = 10$) at $\gamma = 60^\circ$ and $\gamma = 90^\circ$ that can be noticed from Figure 6.18. Moreover, average temperature due to nanofluids is less than pure fluids. Average temperature in the cavity is an increasing function of thermal radiation parameter as can be inferred from Figure 6.19. Average temperature increases linearly with temperature ratio parameter that is illustrated by Figure 6.20. From Figure 6.21, average temperature increases with porosity parameter.

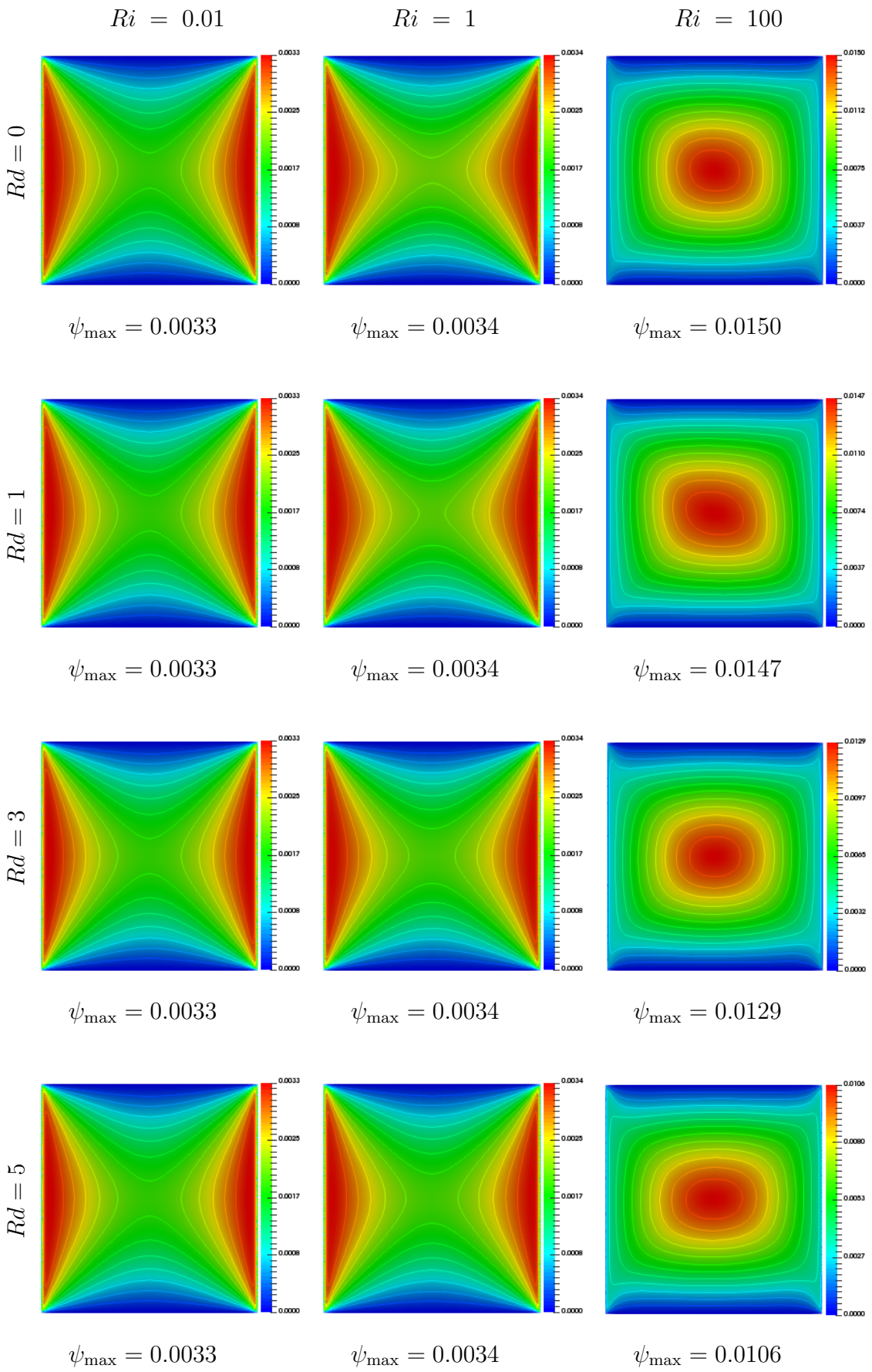

Figure 6.3: Streamline contours for different radiation parameters.

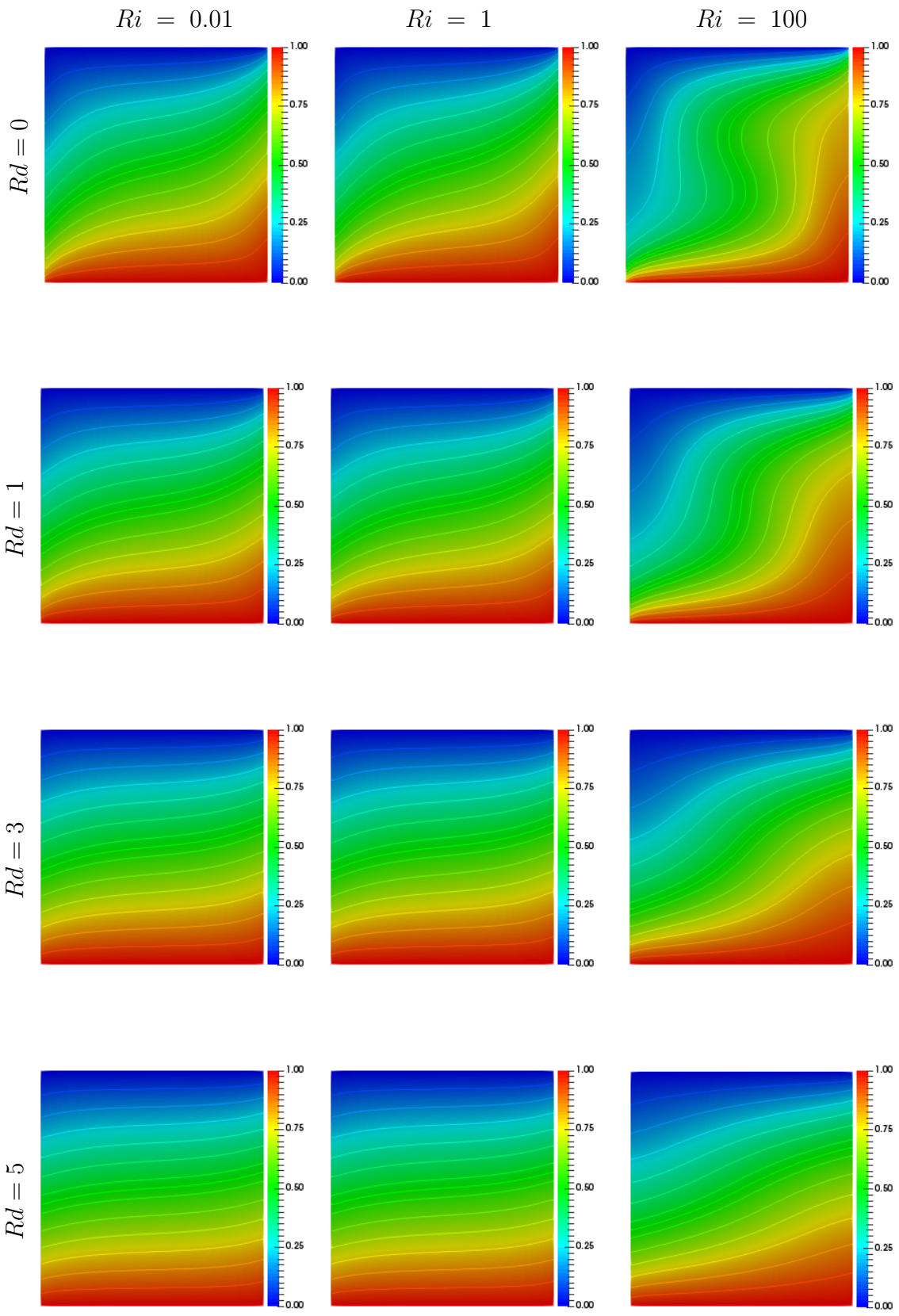

Figure 6.4: Isotherm contours for different radiation parameters.

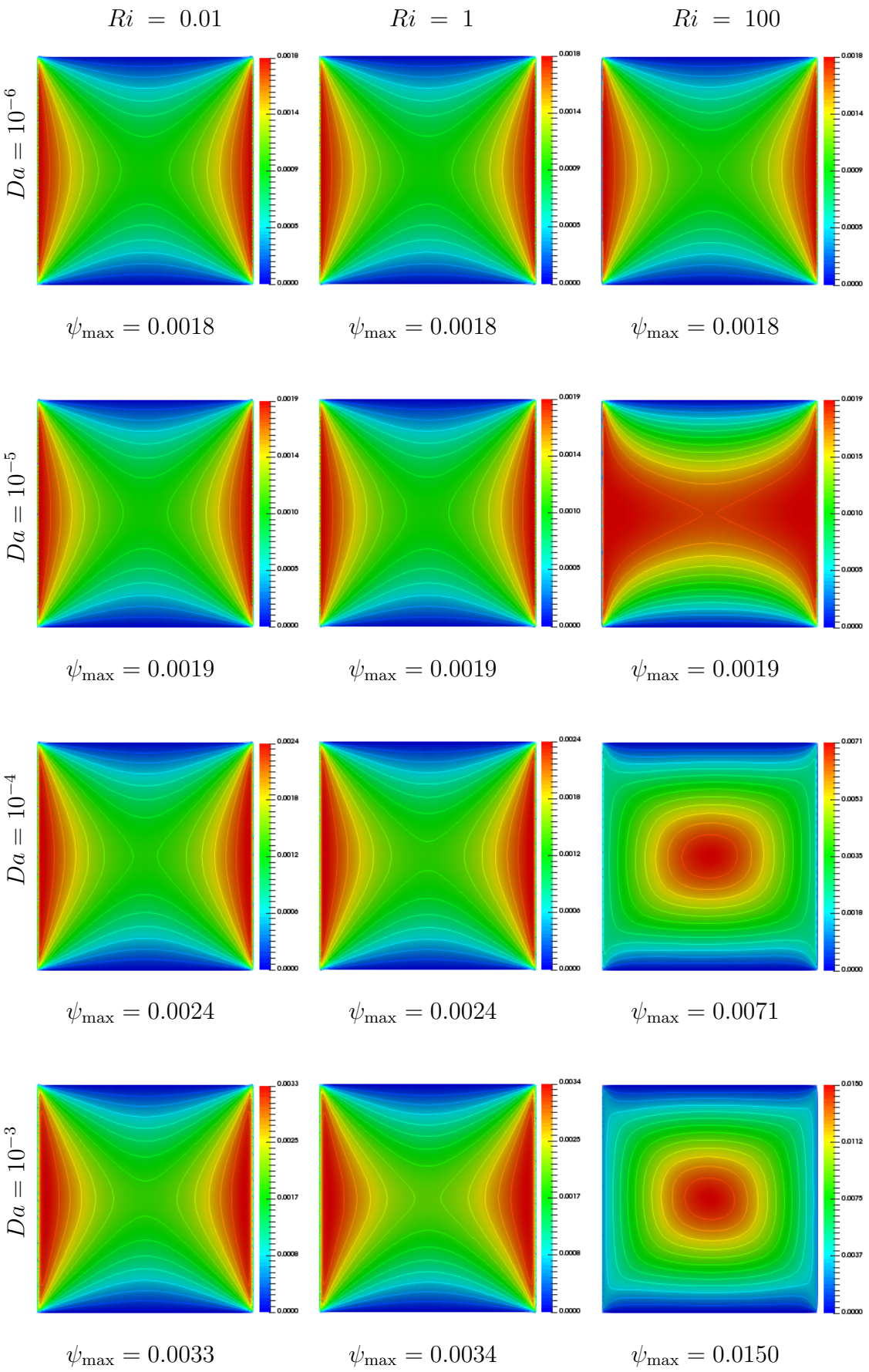

Figure 6.5: Streamline contours for different Darcy numbers.

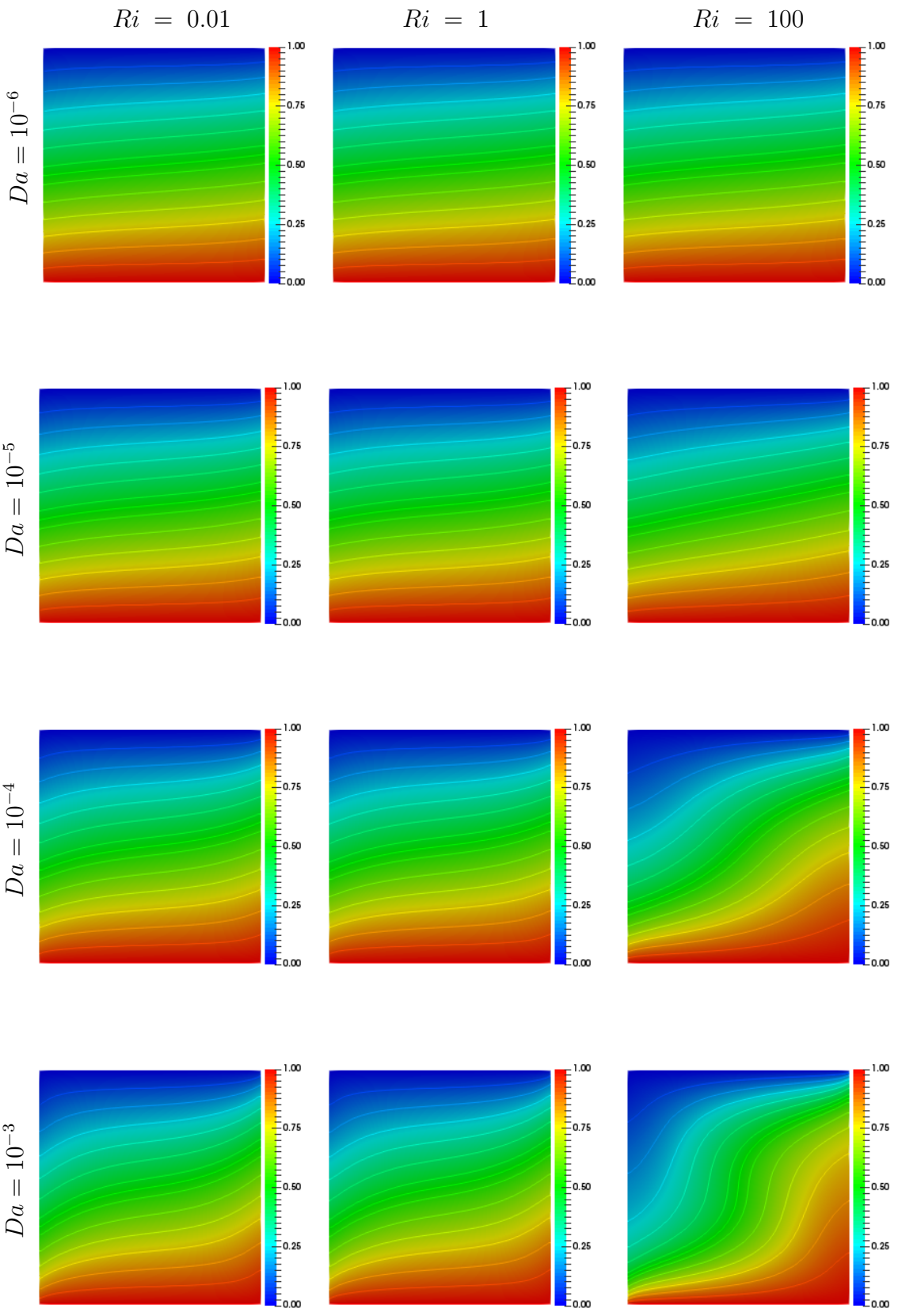

Figure 6.6: Isotherm contours for different Darcy numbers.

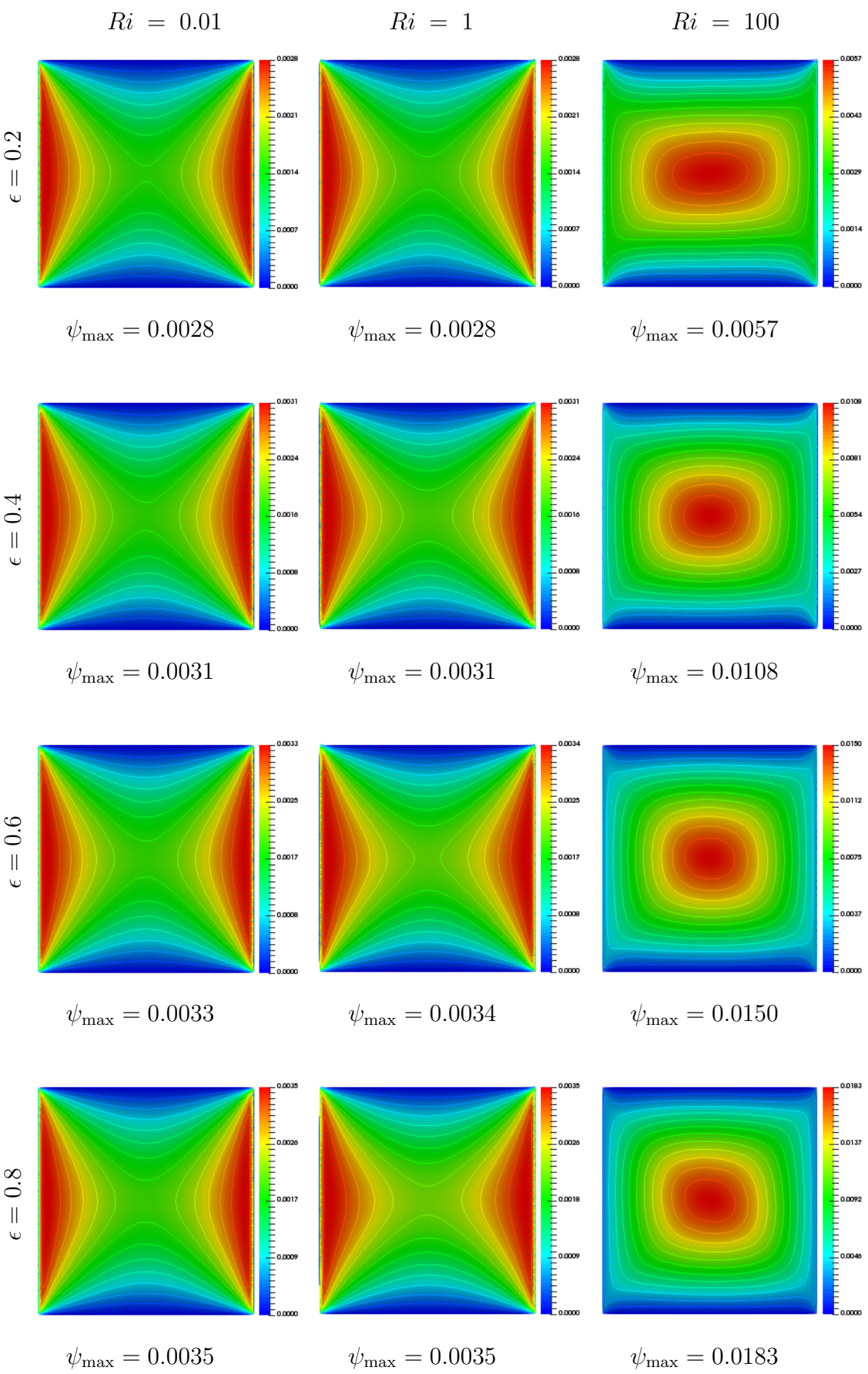

Figure 6.7: Streamline contours for different porosity parameters.

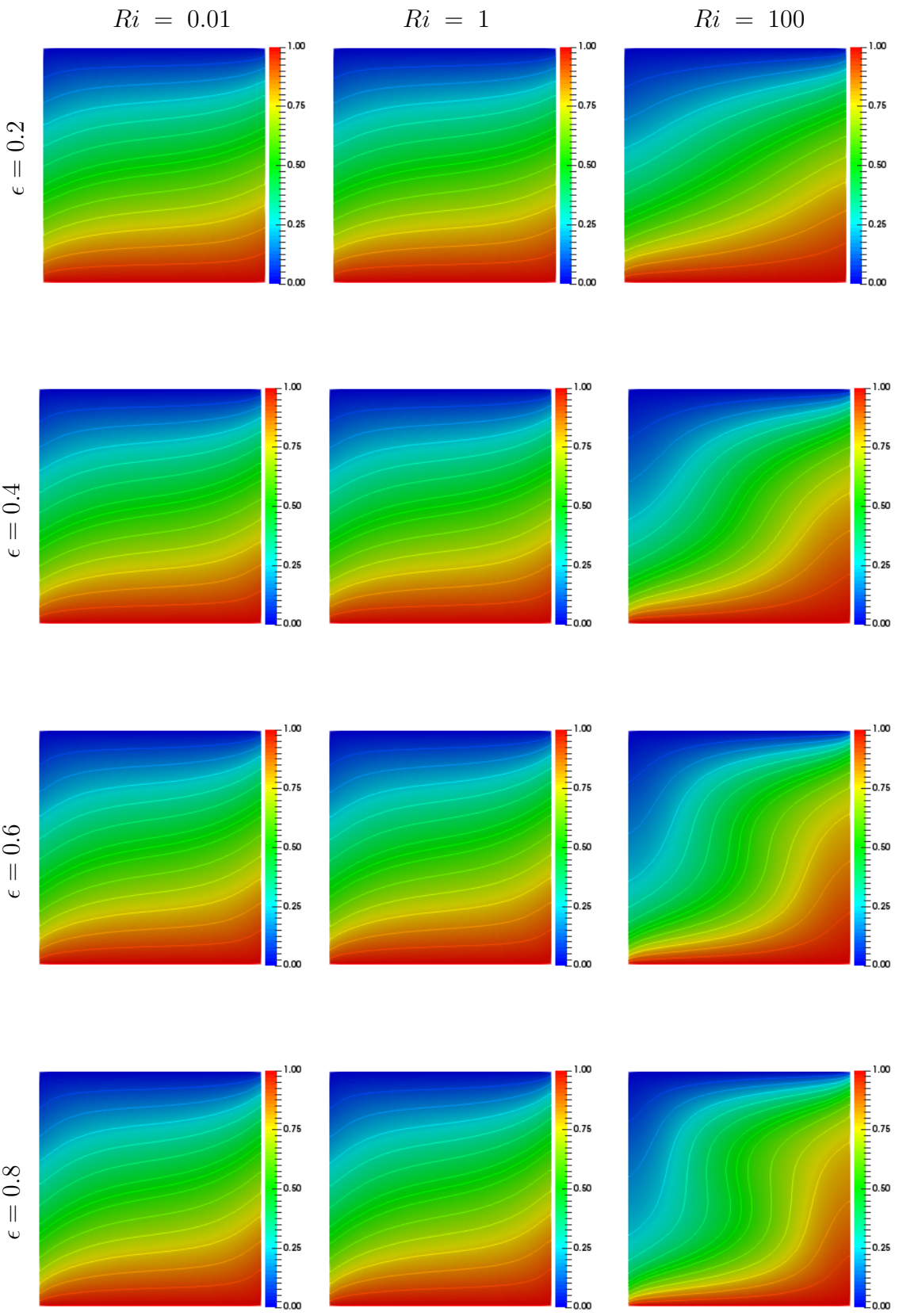

Figure 6.8: Isotherm contours for different porosity parameters.

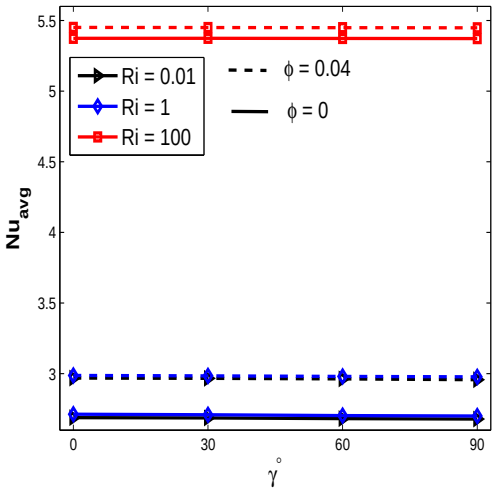

Figure 6.9: Effect of Richardson number on average Nusselt number at the bottom hot wall due to magnetic field inclined angle.

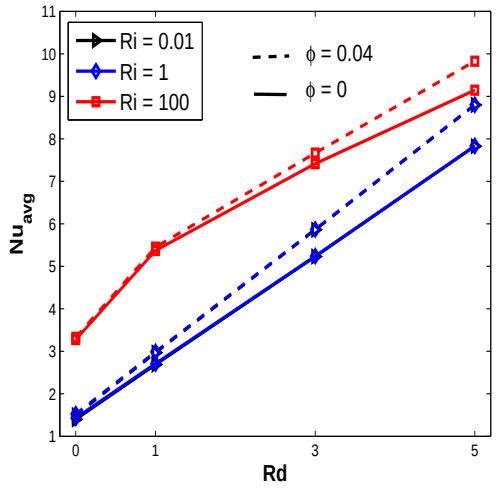

Figure 6.10: Effect of Richardson number on average Nusselt number at the bottom hot wall due to radiation parameter.

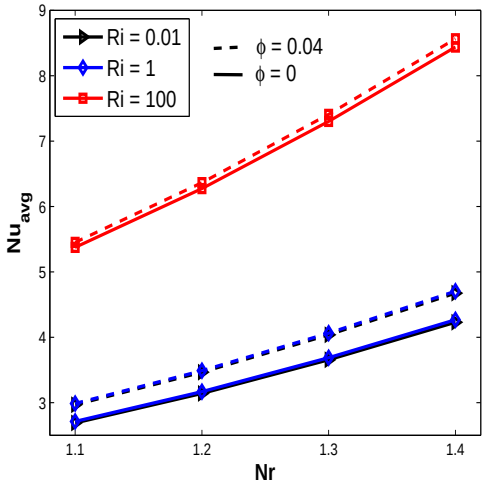

Figure 6.11: Effect of Richardson number on average Nusselt number at the bottom hot wall due to temperature ratio parameter.

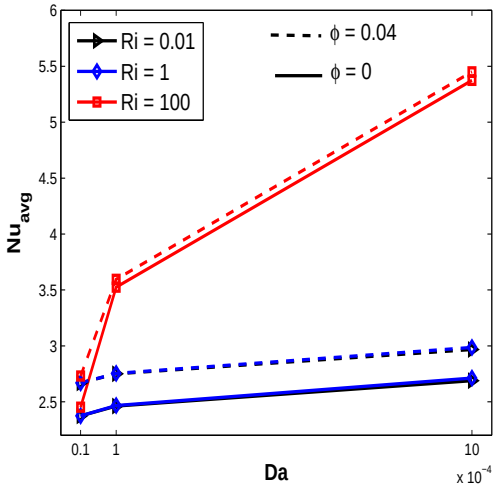

Figure 6.12: Effect of Richardson number on average Nusselt number at the bottom hot wall due to Darcy number.

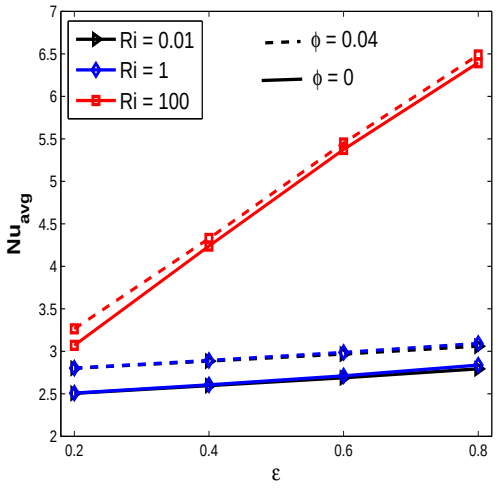

Figure 6.13: Effect of Richardson number on kinetic energy due to porosity parameter.

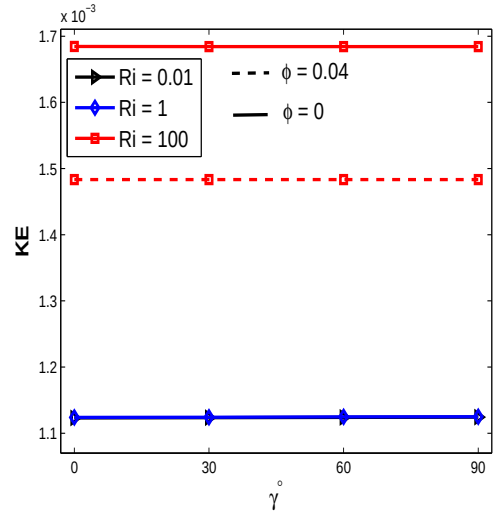

Figure 6.14: Effect of Richardson number on kinetic energy due to magnetic field inclined angle.

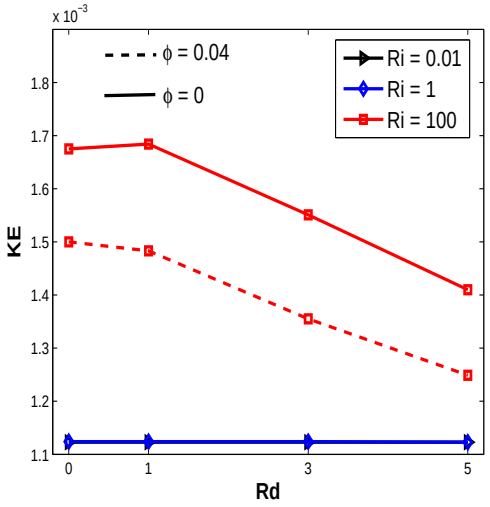

Figure 6.15: Effect of Richardson number on kinetic energy due to radiation parameter.

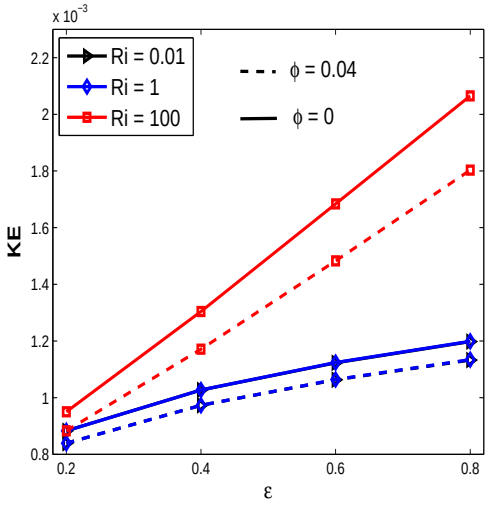

Figure 6.16: Effect of Richardson number on kinetic energy due to porosity parameter.

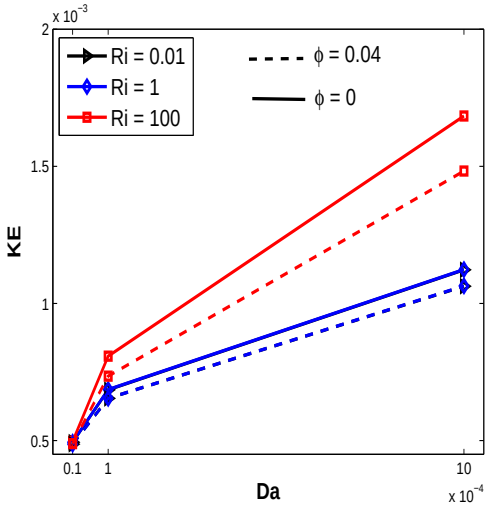

Figure 6.17: Effect of Richardson number on kinetic energy due to Darcy number.

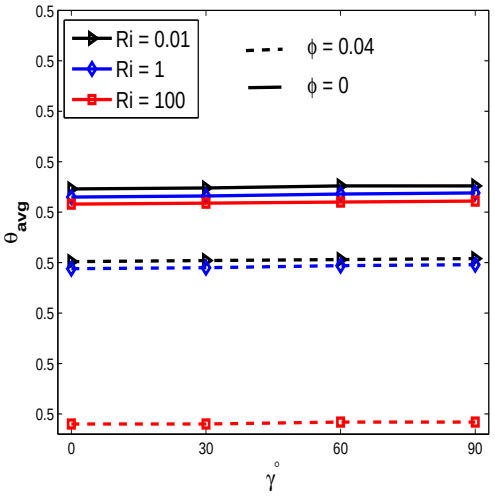

Figure 6.18: Effect of Richardson number on average temperature as a function of magnetic field inclined angle.

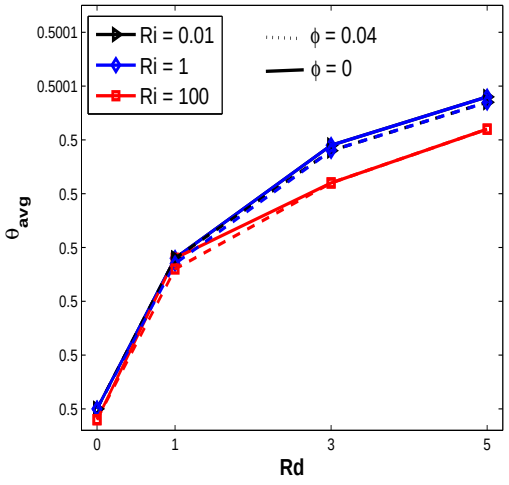

Figure 6.19: Effect of Richardson number on average temperature as a function of radiation parameter.

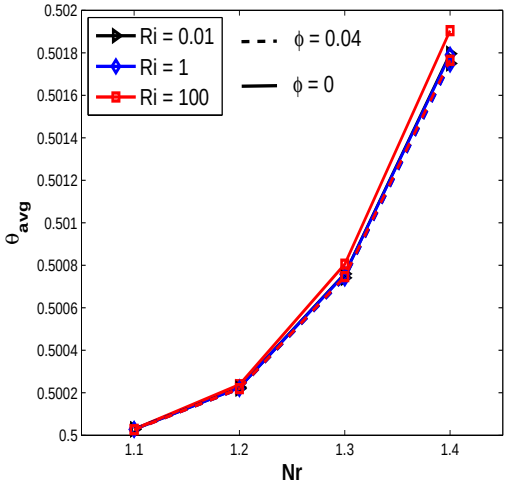

Figure 6.20: Effect of Richardson number on average temperature as a function of temperature ratio parameter.

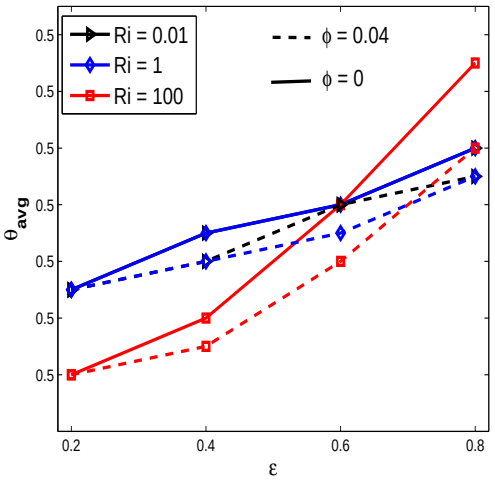

Figure 6.21: Effect of Richardson number on average temperature as a function of porosity parameter.

6.5 Closing Remarks

In this study, numerical simulation has been performed on the mixed convective alumina-water nanofluid filled porous square cavity considering the effects of non-linear thermal radiation and inclined magnetic field. The governing equations are solved through the Galerkin finite element method. The streamlines, isotherms and some important plots are sketched in order to explore the influence of pertinent parameters on the flow. Some significant points of the present investigation may be summarized as follows

- For a fixed value of Richardson number, an increase in maximum stream function value has been observed with a rise in porosity parameter and Darcy number that is more pronounced for dominant free convective flows.
- An augmentation in maximum stream function value has been noticed with a growth in thermal radiation parameter as well, for free convection flows.
- The amplification in the heat transfer has been observed with an extension in Darcy number, solid volume fraction, porosity, radiation and temperature ratio parameters.

- A reduction in average Nusselt number has been explored with an increase in magnetic field inclined angle.

- More heat transfer has been seen as a function of Darcy number, porosity, temperature ratio, radiation and magnetic field inclination parameters for the case of nanofluid with $\phi = 0.04$ as compared to the pure fluid $\phi = 0$.

- The kinetic energy and the average temperature are increasing functions of Darcy number, thermal radiation and porosity parameter but interestingly pure fluid with $\phi = 0$ has greater values for average temperature and kinetic energy as compared to nanofluid with $\phi = 0.04$.

- The average temperature is almost constant up to $\gamma = 30°$, further increment in magnetic field inclined angle results a decline in average temperature for forced and mixed convective regimes whereas opposite behavior has been inspected for free convection flows.

- An augmentation in the inclined magnetic field angle results a slight increase in kinetic energy for forced and mixed convection cases whereas opposite response is observed for free convective flow regime.

Chapter 7

Conclusion and Future Work

7.1 Introduction

In this thesis, numerical simulation of mixed convective alumina-water nanofluid flow in a double lid driven square cavity is executed. Initially, we considered the influence of cavity inclination angle on the mixed convective nanofluid flow in a double lid-driven cavity. Then the magnetohydrodynamics mixed convective nanofluid flow and entropy generation in a double lid-driven square cavity with discrete heating was examined. Furthermore, the mixed convection in nanofluid filled lid-driven square cavity with an isothermally heated square blockage inside with magnetic field effect is analyzed. At the end, the mixed convective nanofluid flow in a lid-driven square porous cavity using the KKL model considering the effect of thermal radiation and inclined magnetic field was discussed. Furthermore, the behaviour of the average Nusselt number, the entropy generation due to heat transfer, fluid friction, magnetic field, the total entropy generation, the average temperature, kinetic energy and Bejan number have been investigated under the influence of different physical parameters like Reynolds number, Richardson number, Hartmann number, Eckert number, Darcy number, nanoparticles volume fraction, cavity inclination angle, magnetic field inclination angle, porosity and thermal radiation parameter. The whole study can be concluded in the following remarks.

7.2 The Concluding Remarks

- With an increase in the buoyancy forces, an augmentation in the heat transfer and the entropy generation due to heat transfer is observed.
- The total entropy generation and the Bejan number enhance with an increase in the Reynolds number and the nanoparticle volume fraction.
- The entropy generation due to the fluid friction declines with a rise in the buoyancy forces.
- The entropy generation due to the fluid friction grows with an increment in the Reynolds number and magnetic field strength.
- Bejan number increases with a rise in the Reynolds number.
- The kinetic energy increases with an increase in the Reynolds number, Richardson number and nanoparticle volume fraction whereas it reduces for the increasing values of the magnetic field.
- An augmentation in the nanoparticles volume fraction causes a significant increase in the heat transfer.
- An increase in the cavity inclination angle diminishes the entropy generation due to heat transfer, fluid friction, average temperature and kinetic energy.
- An increase in the inclination angle causes to increase the heat transfer due to the left discrete heat source while an opposite behavior is observed for the right discrete heat source.
- A reduction in the average Nusselt number and an augmentation in the average entropy generation due to the heat transfer, the average total entropy generation and the average temperature are observed with an increment in the Eckert number.
- An increase in the average temperature in the cavity has been noticed with an augmentation in the Eckert number and magnetic field strength.

- A decline in the heat transfer, the entropy generation due to the heat transfer, Bejan number and the kinetic energy is perceived with an increase in the magnetic field strength.

- An increase in the heat transfer is seen with a growth in the thermal radiation parameter that is more pronounced for the case of nanofluid and free convective flow regime.

- For a fixed value of the Richardson number, an increase in the maximum stream function value is observed with a rise in the porosity parameter and the Darcy number that is more pronounced for dominant free convective flows.

- An augmentation in the maximum stream function value is noticed with a growth in the thermal radiation parameter as well, for free convection flows.

- A magnification in the heat transfer is observed with a rise in the Darcy number, solid volume fraction, porosity, radiation and temperature ratio parameters.

- A reduction in the heat transfer is explored with an increase in the magnetic field inclined angle.

- More heat transfer is seen as a function of Darcy number, porosity, temperature ratio, radiation and magnetic field inclination parameters for the case of nanofluid as compared to the pure fluid.

- The kinetic energy and the average temperature are increasing functions of the Darcy number, thermal radiation and porosity parameter but interestingly pure fluid has greater values for the average temperature and the kinetic energy as compared with the nanofluid.

- The average temperature is almost constant up to the magnetic field inclination angle $\gamma = 30^{\circ}$, further increment in the magnetic field inclined angle results a decline in the average temperature for forced and mixed convective regimes whereas an opposite behavior is inspected for free convection flows.

- An amplification in the inclined magnetic field angle results a slight increase in the kinetic energy for forced and mixed convection cases whereas an opposite response is observed for free convective flow regime.

7.3 Future Work

We have considered the viscous, laminar, Newtonian and incompressible fluid in a square lid-driven cavity. A lot of work can be done in this direction by considering the non-Newtonian fluid. Turbulent flow regime can also be considered. A list of some possible problems out of many is given in the following.

- Entropy generation in the non-Newtonian fluids can be considered with different effects.
- Double diffusion phenomenon along with the entropy generation can be investigated with various physical effects.
- Effect of porosity can be examined considering the entropy generation.

Bibliography

[1] S. U. S. Choi. Enhancing thermal conductivity of fluids with nanoparticles. *ASME Fluids Engineering*, 231:99–105, 1995.

[2] J. A. Eastman, S. U. S. Choi, S. Li, W. Yu, and L. J. Thompson. Anomalously increased effective thermal conductivities of ethylene glycol-based nanofluids containing copper nanoparticles. *Applied Physics*, 78:718–720, 2001.

[3] J. A. Eastman, S. U. S Choi, S. Li, L. J. Thompson, and S. Lee. Enhanced thermal conductivity through the development of nanofluids. *Materials Research Society Symposia Proceedings*, 457:3–11, 1997.

[4] G. Roy, C. T. Nguyen, and P. R. Lajoie. Numerical investigation of laminar flow and heat transfer in a radial flow cooling system with the use of nanofluids. *Superlattices and Microstructures*, 35:497–511, 2004.

[5] X. Wang, X. Xu, and S. U. S. Choi. Thermal conductivity of nanoparticles--fluid mixture. *Journal of Thermophysics and Heat Transfer*, 13:474–480, 1999.

[6] J. A. Eastman, S. U. S. Choi, S. Li, G. Soyez, L. J. Thompson, and R. J. DiMelfi. Novel thermal properties of nanostructured materials. *Journal of Metastable and Nanocrystalline Materials*, 2:629–634, 1999.

[7] S. Lee, S. U. S. Choi, S. Li, and J. A. Eastman. Measuring thermal conductivity of fluids containing oxide nanoparticles. *Journal of Heat Transfer*, 121:280–289, 1999.

[8] Y. Xuan and W. Roetzel. Conceptions for heat transfer correlation of nanofluids. *International Journal of Heat and Mass Transfer*, 43:3701–3707, 2000.

[9] M. Jourabian, M. Farhadi, and A. A. R. Darzi. Outward melting of ice enhanced by Cu nanoparticles inside cylindrical horizontal annulus. *Applied Mathematical Model*, 37(20-21):8813–8825, 2013.

[10] S. S. Azimi and M. Kalbasi. Numerical study of dynamic thermal conductivity of nanofluid in the forced convective heat transfer. *Applied Mathematical Model*, 38(4):1373–1384, 2014.

[11] M. Kalteh. Investigating the effect of various nanoparticles and base liquid types on the nanofluids heat and fluid flow in a microchannel. *Applied Mathematics*, 37:18–19, 2013.

[12] R. Ellahi. The effects of MHD and temperature dependent viscosity on the flow of non-Newtonian nanofluid in a pipe: Analytical solutions. *Applied Mathematics*, 37(3):1451–1467, 2013.

[13] S. Hussain, K. Mehmood, and M. Sagheer. MHD mixed convection and entropy generation of water-alumina nanofluid flow in a double lid driven cavity with discrete heating. *Journal of Magnetism and Magnetic Materials*, 419:140–155, 2016.

[14] S. Hussain, S. Ahmed, K. Mehmood, and M. Sagheer. Effects of inclination angle on mixed convective nanofluid flow in a double lid-driven cavity with discrete heat sources. *International Journal of Heat and Mass Transfer*, 106: 847–860, 2017.

[15] K. Mehmood, S. Hussain, and M. Sagheer. Mixed convection in alumina-water nanofluid filled lid–driven square cavity with an isothermally heated square blockage inside with magnetic field effect: Introduction. *International Journal of Heat and Mass Transfer*, 109:397–409, 2017.

[16] K. Mehmood, S. Hussain, and M. Sagheer. MHD mixed convection in alumina–water nanofluid filled square porous cavity using KKL model: Effects of non-linear thermal radiation and inclined magnetic field. *Journal of Molecular Liquids*, 238:485–498, 2017.

[17] S. Hussain, K. Mehmood, A. Farooq, and M. Sagheer. Entropy generation analysis of mixed convective flow in an inclined channel with cavity with Al_2O_3-water nanofluid in porous medium. *International Communications in Heat and Mass Transfer*, 89:198–210, 2017.

[18] E. Sourtiji, M. G. Bandpy, D. D. Ganji, and S. F. Hosseinizadeh. Numerical analysis of mixed convection heat transfer of Al_2O_3-water nanofluid in a ventilated cavity considering different positions of the outlet port. *Powder Technology*, 262:71–81, 2014.

[19] M. A. Teamah, M. M. Sorour, W. M. El-Maghlany, and A. Afifi. Numerical simulation of double diffusive laminar mixed convection in shallow inclined cavities with moving lid. *Alexandria Engineering Journal*, 52:227–239, 2013.

[20] S. E. Ahmed, M. A. Mansour, A. K. Hussein, and S. Sivasankaran. Mixed convection from a discrete heat source in enclosures with two adjacent moving walls and filled with micropolar nanofluids. *Engineering Science and Technology, an International Journal*, 19:364–376, 2016.

[21] M. A. Sheremet and I. Pop. Mixed convection in a lid-driven square cavity filled by a nanofluid: Buongiorno mathematical model. *Applied Mathematics and Computation*, 266:792–808, 2015.

[22] M. Sheikholeslami, T. Hayat, and A. Alsaedi. MHD free convection of Al_2O_3-water nanofluid considering thermal radiation: A numerical study. *International Journal of Heat and Mass Transfer*, 96:513–524, 2016.

[23] M. Sheikholeslami. KKL correlation for simulation of nanofluid flow and heat transfer in a permeable channel. *Physics Letters A*, 378:3331–3339, 2014.

[24] M. Sheikholeslami and M. M. Rashidi. Effect of space dependent magnetic field on free convection of Fe_3O_4-water nanofluid. *Journal of the Taiwan Institute of Chemical Engineers*, 000:1–10, 2015.

[25] E. Abu-Nada and A. J. Chamkha. Mixed convection flow in a lid-driven inclined square enclosure filled with a nanofluid. *European Journal of Mechanics B/Fluids*, 29:472–482, 2010.

[26] M. Alinia, D. D. Ganji, and M. Gorji-Bandpy. Numerical study of mixed convection in an inclined two sided lid driven cavity filled with nanofluid using two-phase mixture model. *International Communications in Heat and Mass Transfer*, 38:1428–1435, 2011.

[27] S. Sivasankaran, V. Sivakumar, and A. K. Hussein. Numerical study on mixed convection in an inclined lid-driven cavity with discrete heating. *International Communications in Heat and Mass Transfer*, 46:112–125, 2013.

[28] A. Karimipour, M. H. Esfe, M. R. Safaei, D. T. Semiromi, and S. N. Kazi. Mixed convection of copper-water nanofluid in a shallow inclined lid driven cavity using the Lattice Boltzmann Method. *Physica A*, 2014.

[29] R. K. Tiwari and M. K. Das. Heat transfer augmentation in a two-sided lid-driven differentially heated square cavity utilizing nanofluids. *International Journal of Heat and Mass Transfer*, 50:2002–2018, 2007.

[30] S. M. Sebdani, M. Mahmoodi, and S. M. Hashemi. Effect of nanofluid variable properties on mixed convection in a square cavity. *International Journal of Thermal Science*, 52:112–126, 2012.

[31] M. Muthtamilselvan, P. Kandaswamy, and J. Lee. Heat transfer enhancement of copper-water nanofluids in a lid-driven enclosure. *Communication in Nonlinear Science and Numerical Simulation*, 15:1501–1510, 2010.

[32] C. J. Ho, M. W. Chen, and W. Liz. Numerical simulation of natural convection of nanofluid in a square enclosure: Effects due to uncertainties of

viscosity and thermal conductivity. *International Journal of Heat and Mass Transfer*, 51:4506–4516, 2008.

[33] K. Khanafer and K. Lighstone. Buoyancy-driven heat transfer enhancement in a two-dimensional enclosure utilizing nanofluids. *International Journal of Heat and Mass Transfer*, 46:3639–3653, 2003.

[34] A.H. Mahmoudi, M. Shahi, and F. Talebi. Effect of inlet and outlet location on the mixed convective cooling inside the ventilated cavity subjected to an external nanofluid. *International Communication in Heat and Mass Transfer*, 37:1158–1173, 2010.

[35] A. Malleswaran and S. Sivasankaran. A numerical simulation on MHD mixed convection in a lid-driven cavity with corner heaters. *Journal of Applied Fluid Mechanics*, 9:311–319, 2016.

[36] D. Chatterjee. MHD mixed convection in a lid-driven cavity including a heated source. *Numerical Heat Transfer, An International Journal of Computation and Methodology*, 64(3):235–254, 2013.

[37] A. Kumar, A. K. Singh, P. Chandran, and N. C. Sacheti. Effect of perpendicular magnetic field on free convection in a rectangular cavity. *Sultan Qaboos University Journal for Science*, 20(2):49–59, 2015.

[38] M. Sheikholeslami, M. G. Bandpy, and D. D. Ganji. Numerical investigation of MHD effects on Al_2O_3-water nanofluid flow and heat transfer in a semi-annulus enclosure using LBM. *Energy*, 60:501–510, 2013.

[39] A. K. Hussein, H. R. Ashorynejad, S. Sivasankaran, L. Kolsi, M. Shikholeslami, and I.K. Adegun. Modeling of MHD natural convection in a square enclosure having an adiabatic square shaped body using Lattice Boltzmann Method. *Alexandria Engineering Journal*, 2016.

[40] A. Malvandi, M. R. Safaei, M. H. Kaffash, and D. D.Ganji. MHD mixed convection in a vertical annulus filled with Al_2O_3-water nanofluid considering

nanoparticle migration. *Journal of Magnetism and Magnetic Materials*, 382: 296–306, 2015.

[41] S. Mondal and P. Sibanda. Unsteady double diffusive convection in an inclined rectangular lid-driven enclosure with different magnetic field angles and non-uniform boundary conditions. *International Journal of Heat and Mass Transfer*, 90:900–910, 2015.

[42] M. M. Billah, M. M. Rahman, R. Saidurc, and M. Hasanuzzaman. Simulation of MHD mixed convection heat transfer enhancement in a double lid-driven obstructed enclosure. *International Journal of Mechanical and Materials Engineering*, 6:18–30, 2011.

[43] N. A. Bakar, A. Karimipour, and R. Roslan. Effect of magnetic field on mixed convection heat transfer in a lid-driven square cavity. *Journal of Thermodynamics*, 2016.

[44] K. M. Shirvan, M. Mamourian, S. Mirzakhanlari, and M. Moghiman. Investigation on effect of magnetic field on mixed convection heat transfer in a ventilated square cavity. *Procedia Engineering*, 127:1181–1188, 2015.

[45] A. Malvandi and D. D. Ganji. Magnetic field and slip effects on free convection inside a vertical enclosure filled with alumina/water nanofluid. *Chemical Engineering Research and Design*, 2014.

[46] G. R. Kefayati. Magnetic field effect on heat and mass transfer of mixed convection of shear-thinning fluids in a lid-driven enclosure with non-uniform boundary conditions. *Journal of the Taiwan Institute of Chemical Engineers*, 51:20–33, 2015.

[47] C. G. Mohan and A. Satheesh. The numerical simulation of double-diffusive mixed convection flow in a lid-driven porous cavity with magnetohydrodynamic effect. *Arabian Journal of Science and Engineering*, 2015.

[48] H. M. Elshehabey and S. E. Ahmed. MHD mixed convection in a lid-driven cavity filled by a nanofluid with sinusoidal temperature distribution on the

both vertical walls using Buongiorno nanofluid model. *International Journal of Heat and Mass Transfer*, 88:181–202, 2015.

[49] F. Selimefendigil and A. J. Chamkha. MHD mixed convection in a lid-driven cavity having a corrugated bottom wall and filled with a non-Newtonian power-law fluid under the influence of an inclined magnetic field. *Journal of Thermal Science and Engineering Applications*, 2015.

[50] M. A. Sheremet, I. Pop, and N. C. Rosca. Magnetic field effect on the unsteady natural convection in a wavy-walled cavity filled with a nanofluid: Buongiorno mathematical model. *Journal of the Taiwan Institute of Chemical Engineers*, pages 1–12, 2016.

[51] M. H. Esfe, M. Akbari, and A. Karimipour. Mixed convection in a lid-driven cavity with an inside hot obstacle filled by an Al_2O_3-water nanofluid. *Journal of Applied Mechanics and Technical Physics*, 56:443–453, 2015.

[52] A. W. Islam, M. A. R. Sharif, and E. S. Carlson. Mixed convection in a lid driven square cavity with an isothermally heated square blockage inside. *International Journal of Heat and Mass Transfer*, 55:5244–5255, 2012.

[53] H. F. Öztop, Z. Zhao, and B. Yu. Fluid flow due to combined convection in lid-driven enclosure having a circular body. *International Journal of Heat and Fluid Flow*, 30:886–901, 2009.

[54] M. M. Billah, M. M. Rahman, M. S. Uddin, N. A. Rahim, R. Saidur, and M. Hasanuzzaman. Numerical analysis of fluid flow due to mixed convection in a lid-driven cavity having a heated circular hollow cylinder. *International Communications in Heat and Mass Transfer*, 38:1093–1103, 2011.

[55] A. A. Mehrizi, M. Farhadi, H. H. Afroozi, K. Sedighi, and A. A. R. Darz. Mixed convection heat transfer in a ventilated cavity with hot obstacle: Effect of nanofluid and outlet port location. *International Communications in Heat and Mass Transfer*, 39:1000–1008, 2012.

[56] M. M. Rahman, M. A. H. Mamun, , and R. Saidur. Analysis of magnetohydrodynamic mixed convection and joule heating in lid-driven cavity having a square block. *Journal of the Chinese Institute of Engineers*, 34(5):585–599, 2011.

[57] K. Khanafer and S. M. Aithal. Laminar mixed convection flow and heat transfer characteristics in a lid driven cavity with a circular cylinder. *International Journal of Heat and Mass Transfer*, 66:200–209, 2013.

[58] F. Selimefendigil and H. F. Öztop. Numerical study of MHD mixed convection in a nanofluid filled lid driven square enclosure with a rotating cylinder. *International Journal of Heat and Mass Transfer*, 78:741–754, 2014.

[59] G. F. Zheng, M. Y. Ha, H. S. Yoon, and Y. G. Park. A numerical study on mixed convection in a lid-driven cavity with a circular cylinder. *Journal of Mechanical Science and Technology*, 27(1):273–286, 2013.

[60] M. Musto, N. Bianco, G. Rotondo, F. Toscano, and G. Pezzella. A simplified methodology to simulate a heat exchanger in an aircraft's oil cooler by means of a porous media model. *Applied Thermal Engineering*, 94:836–845, 2016.

[61] Z. G. Xu and C. Y. Zhao. Enhanced boiling heat transfer by gradient porous metals in saturated pure water and surfactant solutions. *Applied Thermal Engineering*, 100:68–77, 2016.

[62] M. Siavashi, M. J. Blunt, M. Raisee, and P. Pourafshary. Three–dimensional streamline-based simulation of non–isothermal two-phase flow in heterogeneous porous media. *Computers and Fluids*, 103:116–131, 2014.

[63] J. Fu, Y. Tang, J. Li, Y. Ma, W. Chen, and H. Li. Four kinds of the two–equation turbulence model's research on flow field simulation performance of DPF's porous media and swirl-type regeneration burner. *Applied Thermal Engineering*, 93:397–404, 2016.

[64] R. Ghasemizadeh, X. Yu, C. Butscher, F. Hellweger, I. Padilla, and A. Alshawabkeh. Equivalent porous media EPM simulation of groundwater hydraulics and contaminant transport in karst aquifers. *PloS one*, 10, 2015.

[65] A. R. A. Khaled and K. Vafai. The role of porous media in modeling flow and heat transfer in biological tissues. *International Journal of Heat and Mass Transfer*, 46:4989–5003, 2003.

[66] S. S. Alrwashdeh, H. Marktter, J. Haumann, T. Arlt, M. Klages, J. Scholta, J. Banhart, and I. Manke. Investigation of water transport dynamics in polymer electrolyte membrane fuel cells based on high porous micro porous layers. *Energy*, 102:161–165, 2016.

[67] M. Cascetta, G. Cau, P. Puddu, and F. Serra. A comparison between CFD simulation and experimental investigation of a packed-bed thermal energy storage system. *Applied Thermal Engineering*, 98:1263–1272, 2016.

[68] T. Stamboul, M. A. Saada, and A. Campo. Maximum heat transfer reduction in a horizontal porous annular cavity induced by the attachment of symmetric radial baffles to the hot inner cylinder. *Applied Thermal Engineering*, 93: 1105–1113, 2016.

[69] G. H. Tang, C. Bi, Y. Zhao, and W.Q. Tao. Thermal transport in nano–porous insulation of aerogel:factors, models and outlook. *Energy*, 90:701–721, 2015.

[70] L. Qin, J. Han, W. Chen, X. Yao, S. Tadaaki, and H. Kim. Enhanced combustion efficiency and reduced pollutant emission in a fluidized bed combustor by using porous alumina bed materials. *Applied Thermal Engineering*, 94:813–818, 2016.

[71] K. Vafai. Handbook of porous media. *Taylor and Francis, New York*, 2005.

[72] D. A. Nield and A. Bejan. Convection in Porous Media, 4th Edition. *Springer*, pages 31–32, 2013.

[73] A. Shenoy, M. Sheermat, and I. Pop. Convective flow and heat transfer from wavy surfaces, viscous fluids, porous media and nanofluids. *Taylor and Francis, Boca Raton*, 2016.

[74] M. A. Sheremet and I. Pop. Natural convection in a square porous cavity with sinusoidal temperature distributions on both side walls filled with a nanofluid: Buongiornos mathematical model. *Transport in Porous Media*, 105:411–429, 2014.

[75] A. J. Chamkha and M. A. Ismael. Natural convection in differentially heated partially porous layered cavities filled with a nanofluid. *Numerical Heat Transfer, Part A: An International Journal of Computation and Methodology*, 65:1089–1113, 2014.

[76] S. E. Ahmed, H. F. Öztop, and K. Al-Salem. Effects of magnetic field and viscous dissipation on entropy generation of mixed convection in porous lid-driven cavity with corner heater. *International Journal of Numerical Methods for Heat & Fluid Flow*, 26, 2016.

[77] A. M. Rashad, M. M. Rashidi, G. Lorenzini, S. E. Ahmed, and A. M. Aly. Magnetic field and internal heat generation effects on the free convection in a rectangular cavity filled with a porous medium saturated with Cu-water nanofluid. *International Journal of Heat and Mass Transfer*, 104:878–889, 2017.

[78] G. C. Bourantas, E. D. Skouras, V. C. Loukopoulos, and V. N. Burganos. Heat transfer and natural convection of nanofluids in porous media. *European Journal of Mechanics B/Fluids*, 43:45–56, 2014.

[79] M. A. Sheremet, S. Dinarvand, and I. Pop. Effect of thermal stratification on free convection in a square porous cavity filled with a nanofluid using Tiwari and Das nanofluid model. *Physica E*, 69:332–341, 2015.

[80] M. A. Sheremet, I. Pop, and N. Bachok. Effect of thermal dispersion on transient natural convection in a wavy-walled porous cavity filled with a

nanofluid: Tiwari and Das nanofluid model. *International Journal of Heat and Mass Transfer*, 92:1053–1060, 2016.

[81] A. M. Rashad, A. J. Chamkha, C. R. Reddy, and P. V. S. N. Murthy. Influence of viscous dissipation on mixed convection in a non-Darcy porous medium saturated with a nanofluid. *Heat Transfer and Asian Research*, 43: 397–411, 2014.

[82] H. Zargartalebi, A. Noghrehabadi, M. Ghalambaz, and I. Pop. Natural convection boundary layer flow over a horizontal plate embedded in porous medium saturated with a nanofluid: Case of variable thermophysical properties. *Transport in Porous Media*, 107:153–170, 2015.

[83] R. Hossain, S. Mahmud, A. Dutta, and I. Pop. Energy storage system based on nanoparticle enhanced phase change material inside porous medium. *International Journal of Thermal Science*, 91:49–58, 2015.

[84] T. Grosan, C. Revnic, I. Pop, and D. B. Ingham. Free convection heat transfer in a square cavity filled with a porous medium saturated by a nanofluid. *International Journal of Heat and Mass Transfer*, 87:36–41, 2015.

[85] V. Kuznetsov and D. A. Nield. The Cheng-Minkowycz problem for natural convective boundary layer flow in a porous medium saturated by a nanofluid: A revised model. *International Journal of Heat and Mass Transfer*, 65:682–685, 2013.

[86] A. J. Chamkha and M. A. Ismael. Conjugate heat transfer in a porous cavity filled with nanofluids and heated by a triangular thick wall. *International Journal of Thermal Science*, 67:135–151, 2013.

[87] M. Ghalambaz, A. Behseresht, J. Behseresht, and A. J. Chamkha. Effects of nanoparticles diameter and concentration on natural convection of the aluminawater nanofluids considering variable thermal conductivity around a vertical cone in porous media. *Advanced Powder Technology*, 26:224–235, 2015.

[88] M. A. Ismael and A. J. Chamkha. Conjugate natural convection in a differentially heated composite enclosure filled with a nanofluid. *Journal of Porous Media*, 18:699–716, 2015.

[89] A. Bejan. Second law analysis in heat transfer. *Energy*, 5:720–732, 1980.

[90] T. Basak, R. Anandalakshmi, S. Roy, and I. Pop. Role of entropy generation on thermal management due to thermal convection in porous trapezoidal enclosures with isothermal and non-isothermal heating of wall. *International Journal of Heat and Mass Transfer*, 67:810–828, 2013.

[91] T. T. Naas, Y. Lasbet, and C. Kezrane. Entropy generation analyze due to the steady natural convection of Newtonian fluid in a square enclosure. *International Journal of Mechanical, Aerospace, Industrial, Mechatronic and Manufacturing Engineering*, 9, 2015.

[92] A. M. Bouchoucha and R. Bessaih. Natural convection and entropy generation of nanofluids in a square cavity. *International Journal of Heat and Technology*, 33:1–10, 2015.

[93] F. Selimefendigil, H. F. Öztop, and N. A. Hamdeh. Natural convection and entropy generation in nanofluid filled entrapped trapezoidal cavities under the influence of magnetic field. *Entropy*, 18(2), 2016.

[94] G. R. Kefayati. Simulation of heat transfer and entropy generation of MHD natural convection of non-Newtonian nanofluid in an enclosure. *International Journal of Heat and Mass Transfer*, 92:1066–1089, 2016.

[95] A. Mchirgui, N. Hidouri, M. Magherbi, and A. B. Brahim. Entropy generation in double-diffusive convection in a square porous cavity using Darcy Brinkman formulation. *Transport in Porous Media*, 93:223–240, 2012.

[96] R. K. Nayak, S. Bhattacharyya, and I. Pop. Numerical study on mixed convection and entropy generation of Cu-water nanofluid in a differentially heated skewed enclosure. *International Journal of Heat and Mass Transfer*, 85:620–634, 2015.

[97] F. Selimefendigil, H. F. Öztop, and A. J. Chamkha. MHD mixed convection and entropy generation of nanofluid filled lid driven cavity under the influence of inclined magnetic fields imposed to its upper and lower diagonal triangular domains. *Journal of Magnetism and Magnetic Materials*, 2016.

[98] M. Bouchmel, B. Nabil, A. M. Ammar, G. Kamel, and O. Ahmed. Entropy generation and heat transfer of Cu-water nanofluid mixed convection in a cavity. *International Journal of Mechanical, Aerospace, Industrial, Mechatronic and Manufacturing Engineering*, 8, 2014.

[99] A. Chamkha, M. Ismael, A. Kasaeipoor, and T. Armaghani. Entropy generation and natural convection of CuO-water nanofluid in C-shaped cavity under magnetic field. *Entropy*, 2016.

[100] M. Y. A. Jamalabadi, J. H. Park, and C. Y. Lee. Optimal design of magnetohydrodynamic mixed convection flow in a vertical channel with slip boundary conditions and thermal radiation effects by using an entropy generation minimization method. *Entropy*, 17:866–881, 2015.

[101] N. Hajialigal, A. Fattahi, M. H. Ahmadi, M. E. Qomi, and E. Kakoli. MHD mixed convection and entropy generation in a 3-D microchannel using Al_2O_3-water nanofluid. *Taiwan Institute of Chemical Engineering*, 46:30–42, 2015.

[102] Z. Mehrez, A. E. Cafsi, A. Belghith, and P. L. Quere. MHD effects on heat transfer and entropy generation of nanofluid flow in an open cavity. *Journal of Magnetism and Magnetic Materials*, 2014.

[103] G. R. Kefayati. Simulation of double diffusive natural convection and entropy generation of power-law fluids in an inclined porous cavity with Soret and Dufour effects. *International Journal of Heat and Mass Transfer*, 2015.

[104] A. Aghaei, H. Khorasanizadeh, G. Sheikhzadeh, and M. Abbaszadeh. Numerical study of magnetic field on mixed convection and entropy generation of nanofluid in a trapezoidal enclosure. *Journal of Magnetism and Magnetic Materials*, 2015.

[105] F. Selimefendigil and H. F. Öztop. Natural convection and entropy generation of nanofluid filled cavity having different shaped obstacles under the influence of magnetic field and internal heat generation. *Journal of the Taiwan Institute of Chemical Engineers*, 00:1–15, 2015.

[106] S. Das, A. S. Banu, R. N. Jana, and O. D. Makinde. Entropy analysis on MHD pseudo-plastic nanofluid flow through a vertical porous channel with convective heating. *Alexandria Engineering Journal*, 54:325–337, 2015.

[107] T. C. Papanastasiou, G. C. Georgiou, and A. N. Alexandrou. Viscous fluid flow. *CRC Press Boca Raton, USA*, 2000.

[108] J. Ligere. Analytical solutions of magnetohydrodynamical problems on a flow of conducting fluid in the entrance region of channels in a strong magnetic field, Ph.D. Thesis. *Riga Technical University, Latvia*, 2014.

[109] J. N. Reddy. An introduction to the finite element method, third edition. *McGraw-Hill*, 2006.

[110] F. Brezzi and M. Fortin. Mixed and hybrid finite element methods. *Springer-Verlag, New York*, 1991.

[111] F. Brezzi and K. J. Bathe. A discourse on the stability conditions for mixed finite element formulations. *Computer Methods in Applied Mechanics and Engineering*, 82:27–57, 1990.

[112] P. Ming and Z. Shi. Nonconforming rotated Q_1 element for reissner mindlin plate. *Mathematical Models and Methods in Applied Sciences*, 11(8):1311–1342, 2001.

[113] S. Hussain, F. Schieweck, and S. Turek. Efficient Newton multigrid solution techniques for higher order space time Galerkin discretizations of incompressible flow. *Applied Numerical Mathematics*, 83:51–71, 2014.

[114] M. Sheikholeslami, M. G. Bandpy, and D. D. Ganji. Numerical investigation of MHD effects on Al_2O_3-water nanofluid flow and heat transfer in a semi-annulus enclosure using LBM. *Energy*, 60:501–510, 2013.

[115] F. Selimefendigil and H. F. Öztop. Numerical study of MHD mixed convection in a nanofluid filled lid driven square enclosure with a rotating cylinder. *International Journal of Heat and Mass Transfer*, 78:741–754, 2014.

[116] A. H. Mahmoudi, I. Pop, and M. Shahi. Effect of magnetic field on natural convection in a triangular enclosure filled with nanofluid. *International Journal of Thermal Sciences*, 59:126–140, 2012.

[117] J. Koo and C. Kleinstreuer. Viscous dissipation effects in microtubes and microchannels. *International Journal of Heat and Mass Transfer*, 47:3159–3169, 2004.

[118] J. C. Maxwell. A treatise on electricity and magnetism. *Oxford University Press, Cambridge, UK*, II, 1873.

[119] J. Koo and C. Kleinstreuer. Laminar nanofluid flow in microheat-sinks. *International Journal of Heat and Mass Transfer*, 48:2652–2661, 2005.

[120] H. C. Brinkman. The viscosity of concentrated suspensions and solutions. *Journal of Chemical Physics*, 20:571–581, 1952.

[121] O. Ghaffarpasand. Numerical study of MHD natural convection inside a sinusoidally heated lid-driven cavity filled with Fe_3O_4-water nanofluid in the presence of Joule heating. *Applied Mathematical Modelling*, 2009.

[122] A. Malleswaran and S. Sivasankaran. A numerical simulation on MHD mixed convection in a lid-driven cavity with corner heaters. *Journal of Applied Fluid Mechanics*, 9:311–319, 2016.

[123] M. A. Sheremet and I. Pop. Mixed convection in a lid driven square cavity filled by a nanofluid: Buongiorno's mathematical model. *Applied Mathematics and Computation*, 266:792–808, 2015.

[124] L. K. Saha, M. C. Somadder, and M. S. Uddin. Mixed convection heat transfer in a lid driven cavity with wavy bottom surface. *American Journal of Applied Mathematics*, 1(5):92–101, 2014.

[125] E. Abu-Nada and A. J. Chamkha. Mixed convection flow in a lid-driven inclined square enclosure filled with a nanofluid. *European Journal of Mechanics B/Fluids*, 29:472–482, 2010.

[126] M. A. R. Sharif. Laminar mixed convection in shallow inclined driven cavities with hot moving lid on top and cooled from bottom. *Applied Thermal Engineering*, 27:1036–1042, 2007.

[127] R. Iwatsu, J. M. Hyun, and K. Kuwahara. Mixed convection in a driven cavity with a stable vertical temperature gradient. *International Journal of Heat and Mass transfer*, 36:1601–1608, 1993.

[128] H. Moumni, H. Welhezi, R. Djebali, and E. Sediki. Accurate finite volume investigation of nanofluid mixed convection in two-sided lid driven cavity including discrete heat sources. *Applied Mathematical Modelling*, 39:4164–4179, 2015.

[129] F. Kuznik, J. Vareilles, G. Rusaouen, and G. Krauss. A double-population Lattice Boltzmann Method with non-uniform mesh for the simulation of natural convection in a square cavity. *International Journal of Heat and Fluid Flow*, 28:862–870, 2007.

[130] H. N. Dixit and V. Babu. Simulation of high Rayleigh number natural convection in a square cavity using the Lattice Boltzmann Method. *International Journal of Heat and Mass Transfer*, 49:727–739, 2006.

[131] G. D. V. Davis. Natural convection of air in a square cavity: a benchmark numerical solutions. *International Journal for Numerical Methods in Fluids*, 3:249–264, 1983.

[132] R. Djebali, M. El Ganaoui, H. Sammouda, and R. Bennacer. Some benchmarks of a side wall heated cavity using Lattice Boltzmann approach. *Fluid Dynamics and Materials Processing*, 5(3):261–282, 2009.

[133] N. C. Markatos and K. A. Pericleous. Laminar and turbulent natural convection in an enclosed cavity. *International Journal of Heat and Mass Transfer*, 27:755–772, 1984.

[134] S. Das, R. N. Jana, and O. D. Makinde. Mixed convective magnetohydrodynamic flow in a vertical channel filled with nanofluids. *Engineering Science and Technology, an International Journal*, 18:244–255, 2015.

[135] H. F. Öztop, Z. Zhao, and B. Yu. Fluid flow due to combined convection in lid-driven enclosure having a circular body. *International Journal of Heat and Fluid Flow*, 30:886–901, 2009.

[136] P. Forghani-Tehrani, A. Karimipour, M. Afrand, and S. Mousavi. Different nanoparticles volume fraction and Hartmann number effects on flow and heat transfer of water–silver nanofluid under the variable heat flux. *Physica E: Low–dimensional Systems and Nanostructures*, 2016.

[137] A. Mahmoudi, I. Mejri, M. A. Abbassi, and A. Omri. Analysis of the entropy generation in a nanofluid-filled cavity in the presence of magnetic field and uniform heat generation/absorption. *Journal of Molecular Liquids*, 198:63–77, 2014.

[138] A. W. Islam, M. A. R. Sharif, and E. S. Carlson. Mixed convection in a lid driven square cavity with an isothermally heated square blockage inside. *International Journal of Heat and Mass Transfer*, 55:5244–5255, 2012.

[139] C. Sivaraj and M. A. Sheremet. Natural convection coupled with thermal radiation in a square porous cavity having a heated plate inside. *Transport in Porous Media*, 2016.

[140] M. M. Rahman, M. A. Al-Lawatia, I. A. Eltayeb, and N. Al-Salti. Hydromagnetic slip flow of water based nanofluids past a wedge with convective surface in the presence of heat generation (or) absorption. *International Journal of Thermal Sciences*, 57:172–182, 2012.

[141] J. Koo and C. Kleinstreuer. Viscous dissipation effects in microtubes and microchannels. *International Journal of Heat and Mass Transfer*, 47:3159–3169, 2004.

[142] M. Grott, J. Knollenberg, and C. Krause. Apollo lunar heat flow experiment revisited: A critical reassessment of the in situ thermal conductivity determination. *Journal of Geophysical Research*, 115, 2010.

[143] K. S. Reddy and D. Sreedhar. Thermal conductivity of natural fiber, glass fiber & CNTs reinforced epoxy composites. *International Journal of Current Engineering and Technology*, 6, 2016.

[144] H. Moumni, H. Welhezi, R. Djebali, and E. Sediki. Accurate finite volume investigation of nanofluid mixed convection in two–sided lid driven cavity including discrete heat sources. *Applied Mathematical Modelling*, 39:4164–4179, 2015.